CRYSTAL STRUCTURE OF *PLASMODIUM FALCIPARUM* DIHYDROFOLATE REDUCTASE – THYMIDYLATE SYNTHASE IN COMPLEX WITH TRIMETHOPRIM

DUANGRUDEE TANRAMLUK

A THESIS SUBMITTED IN PARTIAL FULFILLMENT
OF THE REQUIREMENTS FOR
THE DEGREE OF MASTER OF SCIENCE (BIOCHEMISTRY)
FACULTY OF GRADUATE STUDIES
MAHIDOL UNIVERSITY
2004

ISBN 974-04-5222-1
COPYRIGHT OF MAHIDOL UNIVERSITY

Copyright by Mahidol University

CRYSTAL STRUCTURE OF *PLASMODIUM FALCIPARUM* DIHYDROFOLATE REDUCTASE – THYMIDYLATE SYNTHASE IN COMPLEX WITH TRIMETHOPRIM

.....
Miss Duangrudee Tanramluk
Candidate

.....
Lect. Jirundon Yuvaniyama,
Ph.D. (Biological Chemistry)
Major-Advisor

.....
Miss Penchit Chitnumsub,
Ph.D. (Chemistry)
Co-Advisor

.....
Assoc. Prof. Waraporn Thitinanthapan
D.D.S, Grad. Dip. Clin. Sc.(Endodontics)
M.Sc.(Clinical Science),
Board in Endodontics
Acting Dean
Faculty of Graduate Studies

.....
Prof. Prapon Wilairat,
Ph.D. (Biochemistry)
Chair
Master of Science Programme
in Biochemistry
Faculty of Science

Copyright by Mahidol University

CRYSTAL STRUCTURE OF *PLASMODIUM FALCIPARUM* DIHYDROFOLATE REDUCTASE – THYMIDYLATE SYNTHASE IN COMPLEX WITH TRIMETHOPRIM

was submitted to the Faculty of Graduate Studies, Mahidol University
for the degree of Master of Science (Biochemistry)
on
September 9, 2004

.....
Miss Duangrudee Tanramluk
Candidate

.....
Lect. Jirundon Yuvaniyama,
Ph.D. (Biological Chemistry)
Chair

.....
Miss Penchit Chitnumsub,
Ph.D. (Chemistry)
Thesis Defense Committee

.....
Prof. Yongyuth Yuthavong,
D.Phil. (Organic Chemistry)
Thesis Defense Committee

.....
Assoc. Prof. Waraporn Thitinanthapan
D.D.S, Grad. Dip. Clin. Sc.(Endodontics)
M.Sc.(Clinical Science),
Board in Endodontics
Acting Dean
Faculty of Graduate Studies
Mahidol University

.....
Prof. Prasert Sobhon,
Ph.D.
Dean
Faculty of Science
Mahidol University

Copyright by Mahidol University

ACKNOWLEDGEMENTS

Firstly, I wish to express my deep and sincere gratitude to the extensive support and guidance of my adviser, Dr. Jirundon Yuvaniyama. His excellent knowledge, great patience, ingenuity, endless support, and understanding have contributed in large part for the success of this thesis.

I would like to express my sincere thanks to my co-adviser Dr. Penchit Chitnumsub for her kind assistance and great effort with protein preparation. Without her first *Pf*-DHFR-TS crystal, this research could not have been completed. Her expertise and her well-planned schedule made each day at the laboratory very productive and successful.

I am truly grateful to Prof. Dr. Yongyuth Yuthavong, who gave me all the best opportunities to do drug design research. Besides his initiation of the thesis topic, I deeply appreciate his valuable time and his kind suggestions to the very end of this thesis.

I also extend my gratitude to Asst. Prof. Dr. Supa Hannongbua for supporting and introducing me to the computational aspects of drug design. Many people at the Laboratory for Computational and Applied Chemistry are acknowledged for equipped me with various molecular modeling tools.

I deeply thank Dr. Chawanee Sirichaiwat for trimethoprim derivatives.

I would like to thank Miss Catleya Rojviriya, Mr. Worrapoj Oonanant, Miss Salila Pengthaisong, Miss Chamaiporn Butriang and Miss Yupaporn Osiriphun for their excellent advice on laboratory techniques, sympathetic help, and encouragement throughout. I also wish to thank Miss Rossukon Thongwichian, Mr. Yuthapong Pongboonchu, Mr. Sirisak Lolupiman, Miss Thunyaluck Pratumrat, and Mr. Theerawat Prasertanan for being a constant source of assistance and encouragement.

I acknowledge all the lecturers at Somrudee School, Samutsakhonburana School, Sriboonyanon School, Dalhousie Regional High School, Kasetsart University and Mahidol University for my knowledge and skills. The Development and Promotion of Science and Talents Project and the Junior Science Talent Project are acknowledged for my financial support and opportunities in scientific research.

Finally, I wish to express my deepest gratitude to the unconditional love, great care, and all the best support from my family. I would like to dedicate this thesis to my father, my honorary mother, and the memory of my mother.

Duangrudee Tanramluk

Copyright by Mahidol University

CRYSTAL STRUCTURE OF *PLASMODIUM FALCIPARUM* DIHYDROFOLATE REDUCTASE – THYMIDYLATE SYNTHASE IN COMPLEX WITH TRIMETHOPRIM

DUANGRUDEE TANRAMLUK 4536160 SCBC/M

M.Sc. (BIOCHEMISTRY)

THESIS ADVISORS : JIRUNDON YUVANIYAMA, Ph.D. (Biological Chemistry), PENCHIT CHITNUMSUB, Ph.D. (Chemistry)

ABSTRACT

Plasmodium falciparum dihydrofolate reductase–thymidylate synthase (*Pf*-DHFR–TS) is one of the well-defined antimalarial drug targets. Crystal structures of this enzyme complexed with its potent inhibitors could provide structural information at the molecular level which would assist in antimalarial drug design.

This research aims to co-crystallize this enzyme with trimethoprim, an effective inhibitor of bacterial DHFR, based on the evidence suggesting that trimethoprim–sulfamethoxazole prophylaxis could develop cross-resistance at the molecular level with a combined antimalarial drug, sulfadoxine–pyrimethamine.

The enzyme complex was successfully crystallized and the crystal diffracted X-rays to 2.6 Å resolution. Processing of the diffraction data resulted in R_{merge} of 8.3% for a completeness of 97%. The crystal was of orthorhombic space group $P2_12_12_1$ with unit-cell parameters $\alpha = 90^o$, $\beta = 90^o$, $\gamma = 90^o$, a = 56.3 Å, b = 153.7 Å, c = 164.1 Å with 2 molecules/asymmetric unit (V_M= 2.5 $Å^3$/Da). The structure was determined using Difference Fourier method and refined to R-factor of 22.52% and free R-factor of 27.51%.

Structural investigation reveals that trimethoprim forms van der Waals interaction and hydrogen bonds in the *Pf*-DHFR–TS active site; whereas pyrimethamine has a greater binding affinity via hydrogen bonds, polar-polar, and van der Waals interaction which provide a better fit within the active site pocket.

KEY WORDS : X-RAY CRYSTALLOGRAPHY / CRYSTAL STRUCTURE / *PLASMODIUM FALCIPARUM* / TRIMETHOPRIM / DIHYDROFOLATE REDUCTASE/ THYMIDYLATE SYNTHASE

107 pp. ISBN 974-04-5222-1

Copyright by Mahidol University

โครงสร้างผลึกเอกซเรย์ของเอนไซม์ไดไฮโดรโฟเลตรีดักเทส-ไธมิดิเลตซินเทสจากเชื้อมาลาเรีย *พลาสโมเดียม ฟาลซิพารัม* กับสารประกอบไตรเมโธพริม (CRYSTAL STRUCTURE OF *PLASMODIUM FALCIPARUM* DIHYDROFOLATE REDUCTASE – THYMIDYLATE SYNTHASE IN COMPLEX WITH TRIMETHOPRIM)

ดวงฤดี ธารรำลึก 4536160 SCBC/M

วท.ม. (ชีวเคมี)

คณะกรรมการควบคุมวิทยานิพนธ์ : จิรันดร ยูวะนิยม, Ph.D. (Biological Chemistry), เพ็ญจิตร จิตรนำทรัพย์, Ph.D. (Chemistry)

บทคัดย่อ

เอนไซม์ไดไฮโดรโฟเลตรีดักเทส–ไธมิดิเลตซินเทสของเชื้อมาลาเรีย *พลาสโมเดียม ฟาลซิพารัม* เป็นเอนไซม์เป้าหมายที่สำคัญของการวิจัยยาต้านมาลาเรียชนิดขึ้นสมอง โครงสร้างผลึกเอกซเรย์ของเอนไซม์ดังกล่าวจึงมีความสำคัญต่อการศึกษากลไกการยับยั้งเอนไซม์ในระดับโมเลกุลเพื่อการออกแบบยารักษามาลาเรียชนิดใหม่

งานวิจัยนี้มีวัตถุประสงค์ในการตกผลึกเอนไซม์ดังกล่าวร่วมกับยาไตรเมโธพริมซึ่งเป็นตัวยับยั้งเอนไซม์ไดไฮโดรโฟเลตรีดักเทสของเชื้อแบคทีเรีย เนื่องจากมีงานวิจัยพบว่าการใช้ยาไตรเมโธพริมร่วมกับยาซัลฟาเมธอกซาโซลเป็นเวลานาน อาจทำให้ผู้ป่วยเกิดภาวะดื้อยารักษามาลาเรียซัลฟาดอกซีน—ไพริเมธามีน การศึกษาปฏิสัมพันธ์ในระดับโมเลกุลระหว่างเอนไซม์กับตัวยาไตรเมโธพริมจากโครงสร้างสามมิติของเอนไซม์ดังกล่าวอาจนำไปสู่องค์ความรู้ใหม่เกี่ยวกับกลไกการยับยั้งเอนไซม์และการเหนี่ยวนำการดื้อยาระหว่างกันของยาทั้งสองในระดับโมเลกุล

การตกผลึกเอนไซม์ประสบผลสำเร็จและได้ภาพการหักเหรังสีเอกซเรย์ที่มีความละเอียด 2.6 Å ผลึกที่ได้มีหน่วยเซลล์ที่มีขนาดมุม α = 90º, β = 90º, γ =90º, และมีความยาวด้าน a = 56.3 Å, b = 153.7 Å, c = 164.1 Å โดยแต่ละหน่วยอสมมาตรบรรจุโปรตีน 2 โมเลกุล ผลการหักเหเอกซเรย์มี R_{merge} = 8.7%

จากการศึกษาพบว่าไตรเมโธพริมมีความสามารถในการยับยั้งเอนไซม์น้อยกว่าไพริเมธามีน เนื่องจากการสร้างพันธะเคมีแบบไฮโดรเจนและแบบวานเดอร์วาลกับแอคทีฟไซต์ของเอนไซม์ไพริเมธามีนมีความสามารถในการจับกับยาได้ดีกว่าเนื่องจากการสร้างพันธะไฮโดรเจน, พันธะวานเดอร์วาลส์และพันธะหมู่เคมีที่มีขั้วภายในเอนไซม์

107 หน้า ISBN 974-04-5222-1

Copyright by Mahidol University

CONTENTS

	Page
ACKNOWLEDGEMENTS	iii
ABSTRACT	iv
LIST OF TABLES	ix
LIST OF FIGURES	x
LIST OF ABBREVIATIONS	xiii
CHAPTER	
1 INTRODUCTION	1
1.1 Malaria	1
1.2 Potential Targets in Antimalarial Chemotherapy	3
1.3 Antimalarial Drugs and Resistant Problems	6
1.4 Cross-resistance between HIV/AIDS and Malaria	10
1.5 Structure of *Pf*-DHFR-TS in Complex with Trimethoprim	12
1.6 Trimethoprim as a Potential *Pf*-DHFR-TS Binding Agent	16
1.7 Protein Crystallization	18
1.8 Protein Structure Determination using X-ray Crystallography	20
2 OBJECTIVES	23
2.1 Experimental Strategy	23
2.2 Specific Aims	23
3 MATERIALS AND METHODS	24
PART I: MATERIALS	24
A. Instruments	24
B. Biochemical apparatuses	24
C. Chemicals and Reagents	25
D. Protein Source	26

Copyright by Mahidol University

CONTENTS (CONTINUED)

	Page
PART II: METHODS	27
Summary	27
3.1 Protein Preparation	28
3.1.1 Cell Culture	28
3.1.2 Protein Purification	28
A. Purification by Gel Filtration Chromatography	29
B. Purification by Ion Exchange Chromatography	30
3.1.3 Protein Concentration	31
3.1.4 Protein Characterization	32
A. Determination of DHFR activity	32
B. Sodium Dodecyl Sulfate–Polyacrylamide Gel Electrophoresis	33
C. Determination of Protein Concentration	35
3.2 Crystallization of *Pf*-DHFR-TS	37
3.2.1 Preparation of Crystallizing Agents	37
3.2.2 Preparation of Protein Mixture for Crystallization	38
3.2.3 Microbatch Crystallization	39
3.2.4 Optimizing the Crystal Growth	40
3.2.5 Crystal Selection	41
3.2.6 Crystal Handling and Storage	43
3.3 Data Collection and Processing	44
3.3.1 Crystal Mounting for Cryo-crystallography	44
3.3.2 Data Collection	45
3.3.3 Data Processing	45
3.4 Structure Determination and Refinement	47
3.4.1 Difference Fourier Techniques	47
3.4.2 Model Building Based on Difference Map	48
3.4.3 Structure Refinement	50
3.4.4 Addition of Water Molecules	53

Copyright by Mahidol University

CONTENTS (CONTINUED)

	Page
3.4.5 Composite Omit Map	54
3.5 Structural Analysis	55
4 RESULTS	56
4.1 Protein Purification	56
A. Purification by MTX-Affinity and Gel Filtration Chromatography	56
B. Purification by MTX-Affinity and Ion Exchange Chromatography	61
4.2. Protein Crystallization	64
4.3 Data Collection	70
4.4 Structure Determination and Refinement	73
5 DISCUSSION	78
5.1 Architecture of the Protein	78
5.2 Trimethoprim Conformation	81
5.3 Molecular Interactions in Trimethoprim–*Pf*-DHFR Complex	85
5.3.1 Structural Basis toward the Resistance of C59R+S108N *Pf*-DHFR	86
5.3.2 Trimethoprim in Complex with C59R+S108N *Pf*-DHFR and NADPH	96
6 CONCLUSION	98
REFERENCES	99
BIOGRAPHY	107

Copyright by Mahidol University

LIST OF TABLES

		Page
1.	Antimalarial drugs categorized based on their respective drug targets	6
2.	List of mutants generated by cassette mutagenesis of wild-type synthetic *Pf*-DHFR domain, and also their corresponding field-isolate parasite strains with susceptibility towards pyrimethamine and cycloguanil	15
3.	Inhibition constants of pyrimethamine and trimethoprim	18
4.	Final concentration of ingredients in discontinuous SDS-PAGE gel	34
5.	Summary of crystallizing agents stock solutions	37
6.	Summary of protein mixture solutions	39
7.	Amount of DHFR obtained per 12 litres of cell culture and the protein binding percentage in MTX-column from DHFR activity assay	56
8.	Amount of DHFR obtained per 12 litres of cell after DHF elution	57
9.	Mobility of protein standards for molecular weight estimation	59
10.	Molecular weight estimation of the protein in the fraction 16^{th} eluted from gel filtration column using 10% SDS-PAGE	60
11.	Amount of DHFR obtained per 24 litres of cell culture and the protein binding percentage in MTX-column from DHFR activity assay	61
12.	Amount of DHFR obtained per 24 litres of cell culture after DHF elution	62
13.	Cryoprotectant trial used in crystal freezing	71
14.	X-ray data collection statistics	72
15.	Structure refinement statistics obtained from the best refinement cycle	76
16.	Torsion angles of trimethoprim found in DHFR active site from various organisms	84
17.	Inhibition constants reflecting trimethoprim's species selectivity in *Pf*-DHFR	86

Copyright by Mahidol University

LIST OF FIGURES

Page

1. Life cycle of *Plasmodium falciparum* 2
2. Folate biosynthesis pathway of *P. falciparum* contains two important targets for antimalarial chemotherapy 5
3. Chemical structures of quinoline derivatives and some aryl-amino alcohols currently used in antimalarial chemotherapy 7
4. Chemical structures of artemisinin and its derivatives 8
5. Chemical structures of pABA and sulfa drugs 8
6. Chemical structures of proguanil and its active metabolite cycloguanil 9
7. Chemical structures of pyrimethamine and trimethoprim 7
8. Chemical structure of atovaquone 10
9. The areas with high emergence of malaria and HIV/AIDS 11
10. Chemical reaction catalyzed by dihydrofolate reductase 14
11. Stereo drawing of trimethoprim, a bacterial DHFR inhibitors, bound to chicken liver DHFR and *E. Coli* DHFR 17
12. Illustration of the first crystallization trial conditions 41
13. Birefringence of the crystals 42
14. Diagram of typical cycle of refinement used in this project 52
15. Elution profile of protein fractions obtained from gel-filtration column 57
16. SDS-PAGE (10%) shows purity and size of the purified protein fractions obtained from gel filtration chromatography technique 58
17. Standard curve for SDS-PAGE molecular weight estimation 59
18. Elution profile of protein fractions eluted from Q-Sepharose column 62
19. SDS-PAGE (12.5%) shows purity and size of the purified *Pf*-DHFR-TS fraction obtained from anion exchange chromatography technique 63
20. Microcrystals found from the first batch of crystallization trial 64

Copyright by Mahidol University

LIST OF FIGURES (CONTINUED)

Page

21. Results of crystal morphology obtained in the first batch of crystallization trial 66
22. Crystals obtained from the second batch of crystallization by varying concentration of ammonium acetate (0.55–0.8 M) and PEG 4000 (15–18%) 67
23. Crystals obtained from the third batch of crystallization by varying concentration of ammonium acetate (0.80–0.95 M) and PEG 4000 (15–18%) 68
24. Chemical structure of trimethoprim-39 69
25. Crystals obtained from cocrystallization of the double mutant (C59R+S108N) *Pf*-DHFR-TS and trimethoprim-39 69
26. Diffraction pattern 70
27. Progression of R-factor and R_{free} along the iterative cycles of model refinement 74
28. Ramachandran plots of all of the ϕ/ψ angle pairs for the refined *Pf*-DHFR-TS 77
29. Structure of *Pf*-DHFR-TS 78
30. Structure of *Pf*-DHFR domain in comparison with *E. coli* DHFR 80
31. Stereo representation show the binding of trimethoprim and NADPH in the active site of *Pf*-DHFR 82
32. Binding mode of trimethoprim in the active site of *P. falciparum* DHFR, *P. carinii* DHFR, and *M. tuberculosis* DHFR 83
33. Torsion angles of trimethoprim measured from the crystal structures of *Pf*-DHFR-TS complex, *P. carinii* DHFR complex and *M. tuberculosis* DHFR complex 83
34. Stereo image showing superposition of the trimethoprim and pyrimethamine complexes of C59R+S108N *Pf*-DHFR 87
35. Significant loop shift is found within trimethoprim and pyrimethamine complexes 88

Copyright by Mahidol University

LIST OF FIGURES (CONTINUED)

Page

36. Superposition of S111 loops of C59R+S108N *Pf*-DHFR/NADPH/ pyrimethamine complex and wild-type *Pf*-DHFR/NADPH/WR99210 89
37. Major interacting residues around the pyrimidine rings of trimethoprim and pyrimethamine within the *Pf*-DHFR active sites 90
38. Comparison of water network within the active site of pyrimethamine and trimethoprim complexes 91
39. Stereo image of arginine at the position 59 that affects the catalytic cleft opening 92
40. Comparison of the effects of trimethoprim and pyrimethamine on the conformation of Asn108 93
41. Stereo image showing the highly unfavorable steric interactions found at the position 108 94
42. The *Pf*-DHFR catalytic cleft entry 95
43. Chemical interaction of within 7 Å from trimethoprim in the active site of C59R+S108N *Pf*-DHFR 97

Copyright by Mahidol University

LIST OF ABBREVIATIONS

3D	three-dimension
A	alanine
ADP	adenosine 5′-diphosphate
AIDS	Acquired immunodeficiency syndrome
Ala	alanine
AMP	adenosine 5′-monophosphate
APS	ammonium persulphate
Arg	arginine
Asn	asparagine
Asp	aspartate
ATP	adenosine 5′-triphosphate
C	cysteine
conc.	concentration
Cys	cysteine
Cα	alpha carbon
D	aspartate
Da	dalton, equivalent to the *unified atomic mass unit*
DHODase	Dihydroorotate dehydrogenase
DHF	Dihydrofolate
DHFR	Dihydrofolate reductase
DHPS	Dihydropteroate synthase
DMSO	dimethyl sulfoxide
DTT	dithiothreitol
dTMP	deoxythymidine 5′-monophosphate
dUMP	deoxyuridine 5′-monophosphate

Copyright by Mahidol University

LIST OF ABBREVIATIONS (CONTINUED)

E	glutamic acid
E. coli	*Escherichia coli*
e.g.	for example
EC	Enzyme Commission
EDTA	ethylenediaminetetraacetate
etc.	and so forth
F	phenylalanine
g	gravity (multiples of, as in centrifugal field)
G	glycine
Glu	glutamate
Gln	glutamine
Gly	glycine
GTP	guanosine 5′-triphosphate
H	histidine
His	histidine
HIV	human immunodeficiency virus
hr, hrs	hour, hours
I	isoleucine
i.e.	that is
Ile	isoleucine
IPTG	isopropyl-β-D-thiogalactoside
K	lysine
kDa	kilodalton
K_i	inhibition constant
L	leucine
LB	Luria-Bertani (broth)
log	logarithm (common, base 10)
Leu	leucine
Lys	lysine
M	methionine

Copyright by Mahidol University

LIST OF ABBREVIATIONS (CONTINUED)

M.W.	molecular weight
Met	methionine
mol	mole
MTX	methotrexate
N	asparagine
$NADP^+$	nicotinamide adenine dinucleotide phosphate
NADPH	nicotinamide adenine dinucleotide phosphate (reduced form)
No.	number
OD	optical density
P	proline
P. falciparum	*Plasmodium falciparum*
pABA	para-aminobenzoic acid
PEG 4000	polyethylene glycol with mean molecular weight of 4000
Pf-DHFR-TS	*Plasmodium falciparum* dihydrofolate reductase–thymidylate synthase
Phe	phenylalanine
Pi	orthophosphate
PPi	pyrophosphate
PPPK	7,8-dihydro-6-hydroxymethylpterin pyrophosphokinase
Pro	proline
Q	glutamine
R	arginine
rpm	revolution per minute
S	serine
SDS-PAGE	sodium dodecyl sulfate–polyacrylamide gel electrophoresis
Ser	serine
spp.	species (plural)
T	threonine
TEMED	N,N,N′,N′-tetramethylethylenediamine
THF	Tetrahydrofolate

Copyright by Mahidol University

LIST OF ABBREVIATIONS (CONTINUED)

Thr	threonine
Trp	tryptophan
Tyr	tyrosine
V	valine
Val	valine
vol.	volume
v/v	volume/volume
W	tryptophan
w/v	weight/volume
Y	tyrosine

Copyright by Mahidol University

CHAPTER 1
INTRODUCTION

1.1 Malaria

Malaria is a widespread, tropical disease among developing countries. It is caused by a single cell protozoan *Plasmodium* spp., which are transmitted to humans by the female *Anopheles* spp. mosquitoes.

The *Plasmodium*'s life cycle is spent partly in human and partly in mosquito. Human infection is initiated when the parasite's cells called sporozoites are injected with the saliva of a feeding mosquito. These sporozoites circulate in the bloodstream and invade hepatocytes, where they undergo asexual replicative process known as exo-erythrocytic schizogony. After multiple rounds of parasite's nuclear division without cytokinesis, the infected hepatocytes burst and the merozoites are released into the blood stream.

Erythrocytic cycle starts when the merozoites invade erythrocytes and undergo a trophic period. Beginning from ring morphology, the trophozoites enlarge upon the ingestion of host cytoplasm and the proteolysis of hemoglobin into amino acids. After the trophozoite undergoes multiple rounds of nuclear division without cytokinesis, a schizont is formed. The merozoites, budding from the mature schizonts, cause the infected erythrocyte to rupture and then to invade new erythrocytes again. Some merozoites can differentiate into sexual erythrocytic stages known as macro- and microgametocytes.

When gametocytes are ingested into the midgut of another *Anopheles* mosquito, gametogenesis induction occurs. Microgametes, formed by exflagellation of microgametocyte, will fertilize the macrogamete leading to a zygote. The zygote

Copyright by Mahidol University

develops into a motile ookinete which penetrates the gut epithelial cells and develops into an oocyst. After multiple rounds of asexual replication, the sporozoites are released from the mature oocyst into the hemocoel and then invade the salivary glands of the mosquito. When this mosquito bites the next person, the whole cycle begins again (1, 2).

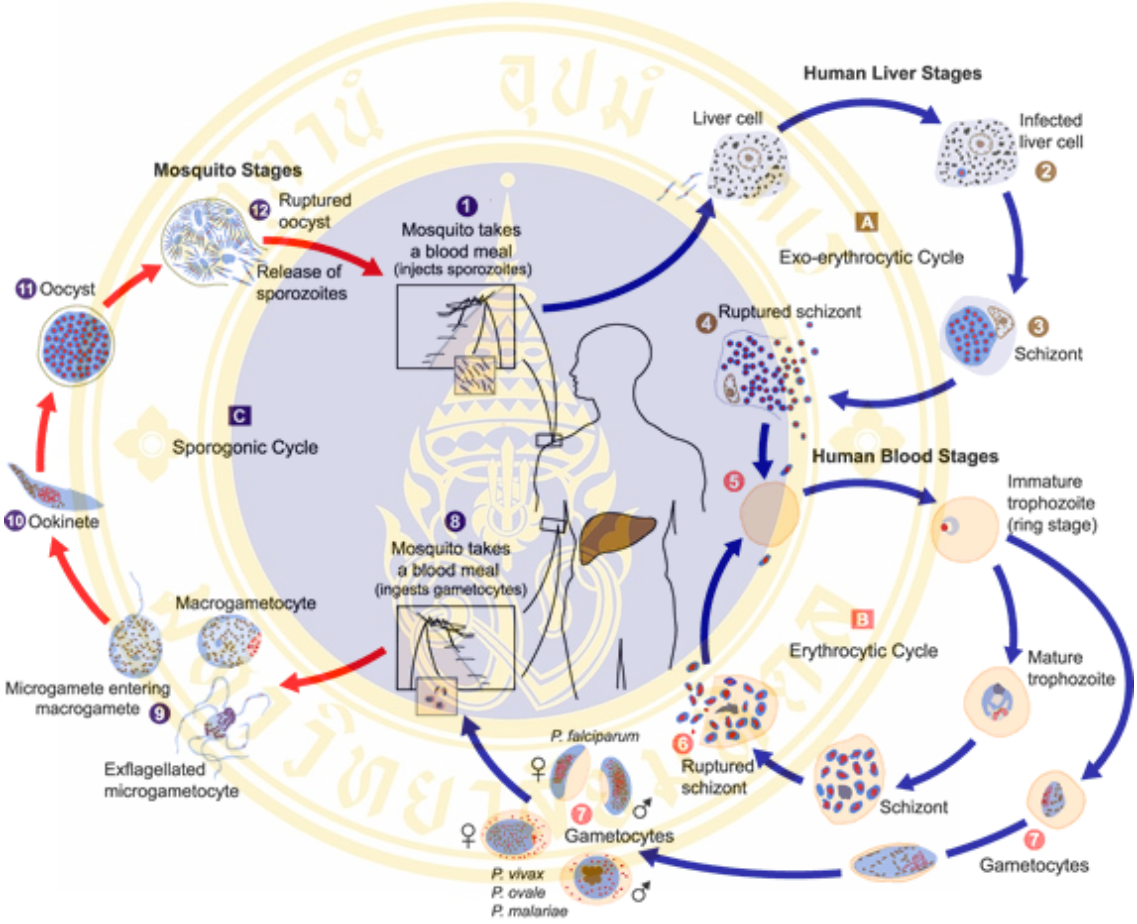

Figure 1 Life cycle of *Plasmodium falciparum*. The malaria parasite undergoes various stages of development in the liver (A) and in the red blood cells of the human host (B), and in the gut and in the salivary gland of the mosquito host (C). Exo-erythrocytic liver stages begin with the entry of sporozoites into hepatocytes. Once merozoites are released from hepatic schizont to invade erythrocytes, the asexual erythrocytic stages start. Some merozoites differentiate into gametocytes, hence they are said to be in the sexual erythrocytic stage. The parasites' multiplication in the mosquito is known as the sporogonic cycle. Figure is available at http://www.dpd.cdc.gov/dpdx/HTML/ImageLibrary/Malaria_il.htm.

Copyright by Mahidol University

Malaria symptoms occur within two weeks after the bite of an infectious mosquito. In general, malaria produces high fever, severe anaemia, headache, weakness, vomiting, and other flu-like symptoms. If treatment is not administered, the symptoms become more severe and the disease would become life-threatening.

World Health Organization has estimated that there are at least 300 million acute cases of malaria each year globally, resulting in more than one million deaths. Among four types of human malaria parasites (*i.e. Plasmodium vivax, Plasmodium malariae, Plasmodium ovale,* and *Plasmodium falciparum)*, *P. falciparum* is the most common, and the most lethal form of malaria, responsible for more than 90% of the deaths. Besides severe anaemia, this parasite causes the clogging of capillaries that carry blood to the brain and other vital organs, making it a deadly pathogen. Children who survive the *P. falciparum* malaria still risk suffering from learning impairments or brain damage (3). The fact that drug-resistant *P. falciparum* parasites have rapidly emerged has placed anti-malarial drug design research in a very critical situation.

1.2 Potential Targets in Antimalarial Chemotherapy

Potential chemotherapeutic targets in the malaria parasites can be classified into three main categories: those involved in processes taking place in the parasite's digestive vacuole, in macromolecular and metabolite syntheses, and in membrane processes and signal transduction (4). Many of the currently available antimalarial drugs are directed against the first two groups.

The digestive vacuole contains many potential drug targets, since the processes of hemoglobin degradation and haem detoxification are unique to the parasite. Haemoglobin is a source of most of the amino acids essential to parasite survival (5). Upon haemoglobin digestion, large quantity of haem is released. Since the free haem (ferriprotoporphyrin) can lyse membranes (6) and generate reactive oxygen species (7), they are detoxified in the digestive vacuole via biocrystallization into large insoluble crystals called hemozoin (8). Quinoline antimalarials are believed to act by interfering with the polymerization of the toxic haem to form hemozoin (9). Even

Copyright by Mahidol University

though various mechanisms of action have been proposed, they seem far from being resolved (10).

Due to the high rate of replication, the parasite has a high demand of nucleotides. Reduced folates serve as cofactors in many one-carbon transfer reactions in various amino acid and nucleotide biosyntheses. Unlike the vertebrate host which obtains preformed folate from food, the parasite cannot efficiently utilize exogenous folate and needs to synthesize the folates either via a *de novo* or salvage pathway. Therefore, enzymes participating in the folate metabolism are potentially good targets for antimalarial chemotherapy (4).

Folate is synthesized from three basic building blocks, *i.e.* GTP, para-aminobenzoic acid, and glutamate. Dihydropteroate synthase (DHPS) is the enzyme that catalyzes the condensation of para-aminobenzoic acid (pABA) and dihydropteridinepyrophosphate to form 7, 8-dihydropteroate which can be converted to folate upon addition of L-glutamic acid. This enzyme can be inhibited by sulfa-based drugs, which are structural analogs of pABA. Sulfonamides and sulfone compete with pABA to form a non-metabolizable sulfa-pterin adduct which leads to the depletion of folate-cofactor pool (11).

Acting down-stream of DHPS, the enzyme dihydrofolate reductase (DHFR) has received a considerable attention from medicinal chemists. This enzyme participates in the recycling of folate by reducing 7,8-dihydrofolate (DHF) back to 5,6,7,8-tetrahydrofolate (THF) using NADPH as a cofactor. Tetrahydrofolate supply is vital to pathways for the thymidylate biosynthesis from dUMP since such process is the only known source of dTMP for DNA synthesis. Blocking the formation of tetrahydrofolate can shut off the supply of dTMP necessary for DNA replication and lead to subsequent parasite death (12).

Copyright by Mahidol University

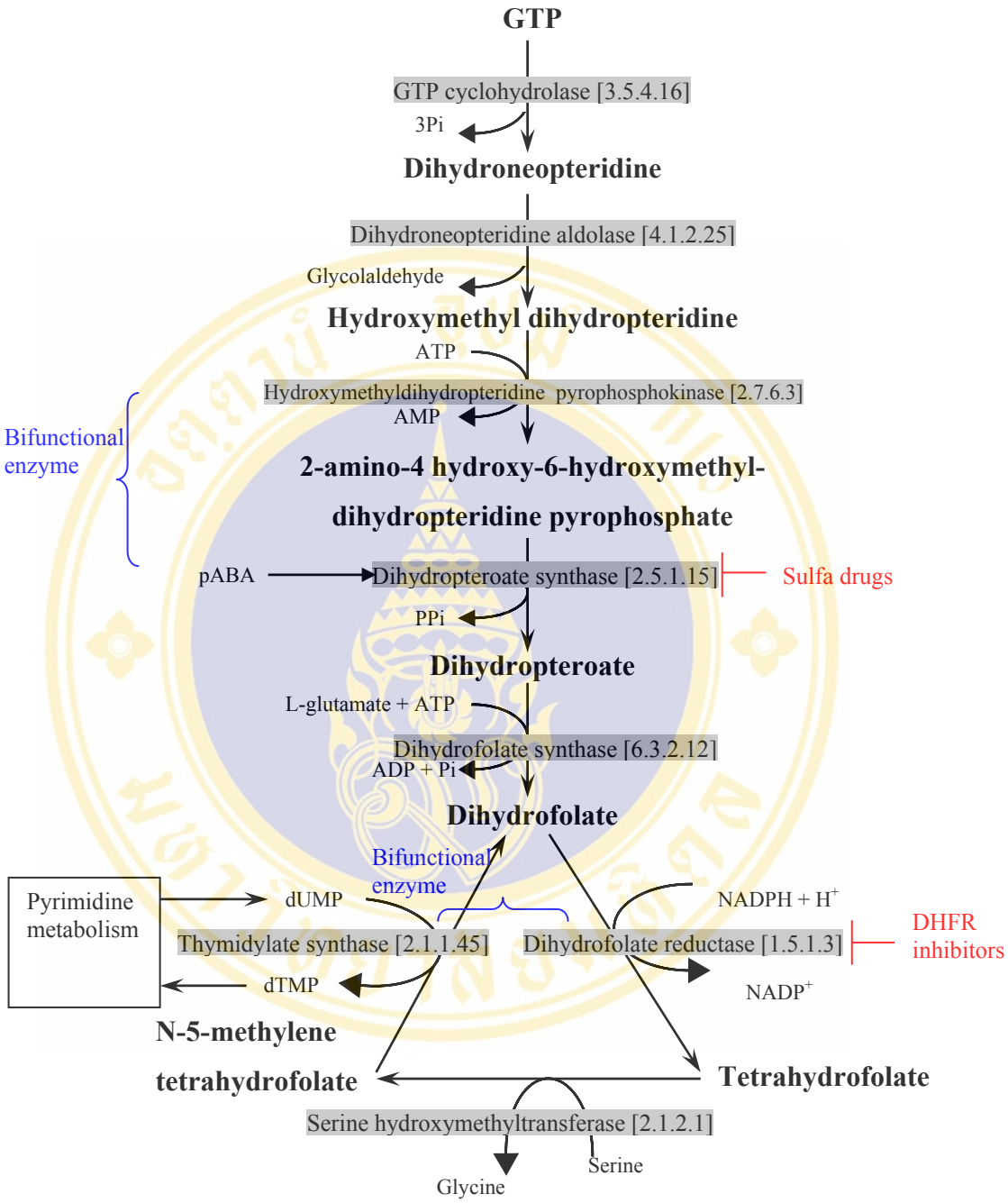

Figure 2 Folate biosynthesis pathway of *P. falciparum* contains two important targets for antimalarial chemotherapy. Both antimalarial targets, dihydropteroate synthase (DHPS) and dihydrofolate reductase (DHFR), are expressed as bifunctional enzymes, *i.e.* DHPS is coupled with 7,8-dihydro-6-hydroxymethylpterin pyrophosphokinase (PPPK) and DHFR is connected to thymidylate synthase (TS). All enzymes are shaded in gray, with respective EC number in square brackets (13).

Copyright by Mahidol University

1.3 Antimalarial Drugs and Resistant Problems

Antimalarial drugs have a selective action on different phases of the parasite's life cycle. The choice of the drug would depend on several factors, such as the presence of partial immunity in human host, the risks of toxic effects, as well as other simpler factors such as availability, preference, and cost. It also depends on the species, and even the strains of the malaria parasite concerned (14).

From years of combating with malaria, various antimalarial drugs have been discovered while many of which become obsolete. Antimalarials frequently used for treatment nowadays can be classified into 5 main classes, derived from the review written by Olliaro, 2001 (10).

Table 1 Antimalarial drugs categorized based on their respective drug targets

Pathway	Class	Mechanism of Action
Haem detoxification	Inhibition/termination of β-haematin formation	Aryl-amino alcohols (quinine, mefloquine, halofantrine)
		4-amino-quinolines (chloroquine, amodiaquine)
Oxidative stress	Free radical formation	Artemisinin derivatives (artesunate, artemeter, arteether)
Nucleic acid metabolism	DHPS inhibitors (mimic pABA)	Sulfonamides (sulfadoxine)
		Sulfones (dapsone)
	DHFR inhibitors (mimic DHF)	2,4-diamino-pyrimidines (pyrimethamine, trimethoprim)
		2,3-dihydrotriazines (cycloguanil, chlorproguanil)
	DHODase inhibitors (mimic ubiquinone)	Naphthoquinones (atovaquone)

Copyright by Mahidol University

Quinine is a quinoline-containing alkaloid originally extracted from *Cinchona* spp. tree bark (15). Structural elucidation of quinine has led to the development of fully synthetic 4-aminoquinolines with less toxic side-effects and better compliance, notably chloroquine and later amodiaquine.

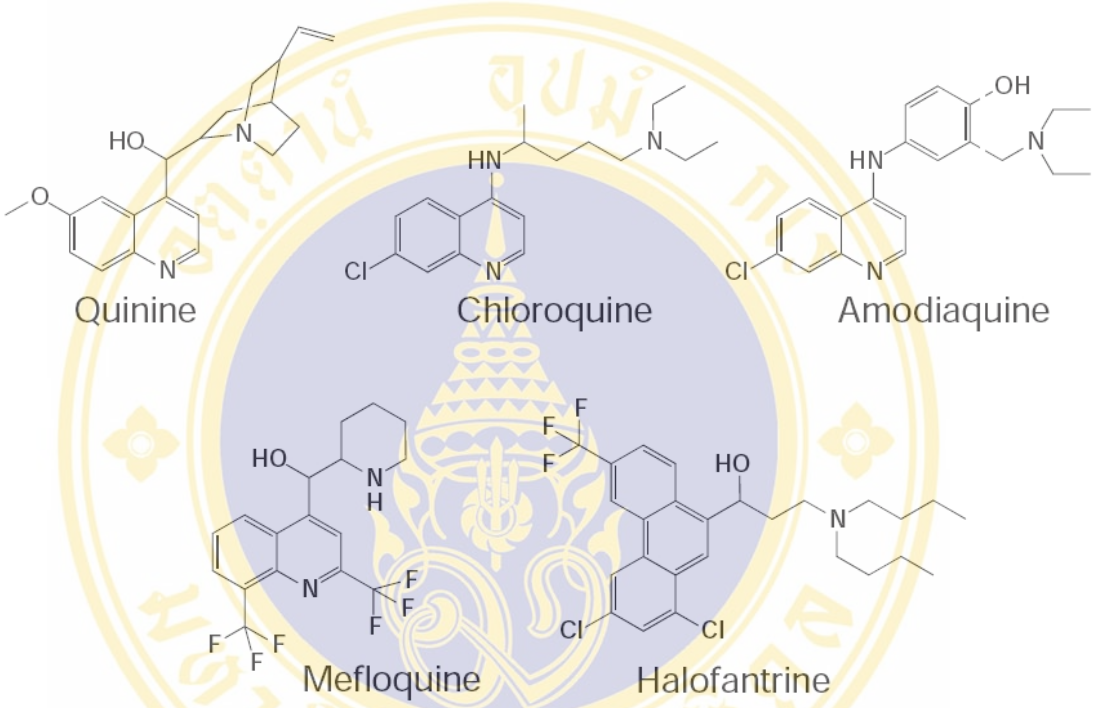

Figure 3 Chemical structures of quinoline derivatives and some aryl-amino alcohols currently used in antimalarial chemotherapy. These drugs are believed to involve haem detoxification of the parasite (16).

Since its introduction in 1940s, chloroquine developed from efforts of the German Forces had become the mainstay of antimalarial chemotherapy (14). Resistance to chloroquine in late 1950s has brought a disastrous consequence due to a difficulty to find available replacement with its safety, affordability, and effectiveness. Both severity and mortality of malaria was increased as the chloroquine resistance spread. Investigation showed that chloroquine resistant strains frequently associated with amodiaquine and quinine resistant (17). Mefloquine and halofantrine have limited usage due to the rapid developments of resistance and their toxic side-effects (16).

Copyright by Mahidol University

Artemisinin is an active ingredient of the Chinese herb 'qinghao', or *Artemisia annua*. It was first isolated in 1972 by Chinese scientists after qinghao was found to have potent antimalarial activity (18, 19). Artemisinin and its derivatives are metabolized to dihydroartemisinin, which has a fast action against the parasite's gametocytes. It is believed that dihydroartemisinin gives rise to toxic radicals involved in oxidative stress induction in infected erythrocytes (20). Nevertheless, the mechanism of action is still being debated (10). Since both the parent derivatives and the dihydroartemisinin metabolite have short half-lives, they are being used in combination with longer half-life drugs (21).

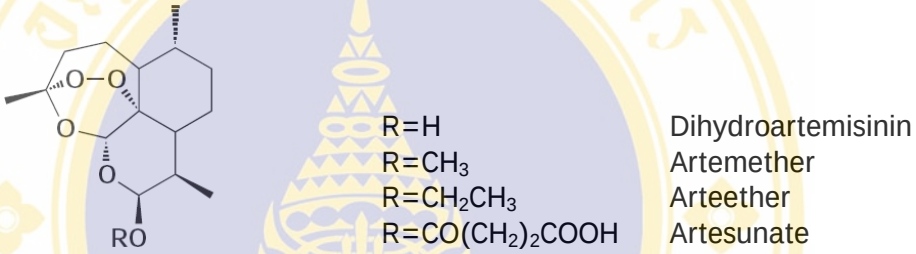

Figure 4 Chemical structures of artemisinin and its derivatives. The metabolized product, dihydroartemisinin, is believed to involve in free radical formation via iron-mediated decomposition

Diamino-diphenyl sulphone (dapsone) and a large numbers of sulphonamide derivatives (*e.g.* sulphadiazine, sulfamethoxazole, and sulphadoxine) are analogs of para-aminobenzoic acid (pABA). They compete with pABA for the enzyme dihydropteroate synthase (DHPS), a part of the parasite's bifunctional enzyme, the 7,8-dihydro-6-hydroxymethylpterin pyrophosphokinase–dihydropteroate synthase (PPPK–DHPS).

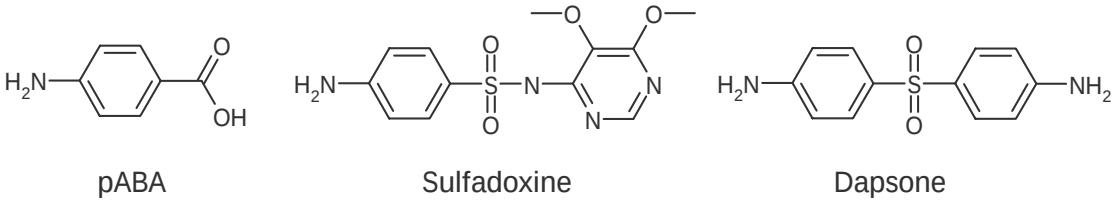

Figure 5 Chemical structures of pABA and sulfa drugs. Sulfadoxine (middle) and sulfamethoxazole, or Dapsone (right), are analogs of pABA (left).

Copyright by Mahidol University

A shortage of quinine during World War II greatly stimulated research in the UK and the USA, resulting in the discoveries of proguanil and pyrimethamine (14). Proguanil is metabolically converted to the cyclic metabolite 'cycloguanil', an analog of 2, 3-dihydrotriazines (22).

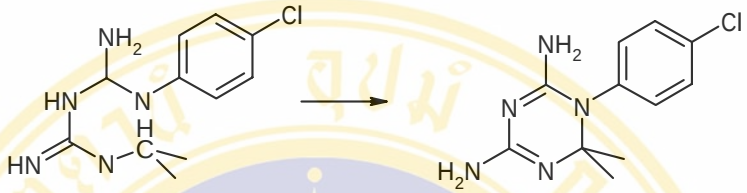

Proguanil Cycloguanil

Figure 6 Chemical structures of proguanil and its active metabolite cycloguanil. Cycloguanil (right) is a potent inhibitor of *P. falciparum* DHFR.

Among a number of 2,4-diaminopyrimidines that have been synthesized, pyrimethamine is the best potential antimalarial. Trimethoprim, though has far less activity against malaria, has been the most widely used antibacterial (12). Both compounds, synthesized by George Hitchings, act by inhibiting the DHFR domain of the bifunctional enzyme dihydrofolate reductase – thymidylate synthase of the parasite.

Trimethoprim Pyrimethamine

Figure 7 Chemical structures of pyrimethamine and trimethoprim. Pyrimethamine (left) inhibits *Pf*-DHFR, but trimethoprim (right) inhibits bacterial DHFR. The two compounds show structural similarity, especially at the 2,4-diaminopyrimidine ring moieties.

Copyright by Mahidol University

Atovaquone shares structural similarities with ubiquinone or coenzyme Q. Therefore, it can selectively inhibit the mitochondrial electron transport chain of protozoa through its action at the bc_1 complex of the respiratory chain (23).

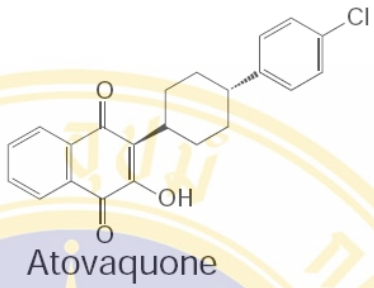

Figure 8 Chemical structure of atovaquone. It inhibits the parasite's electron transport chain

The resistance to chloroquine has necessitated the use of alternative drugs. Treatment of chloroquine-resistant malaria is often attempted with combined medication therapy because a synergistic effect on the parasite would result in tremendous increase in therapeutic action (15). The currently popular combined treatments include sulphadoxine-pyrimethamine, chloroquine-dapsone, atovaquone-proguanil, and artemisinin-based combination therapy (24).

1.4 Cross-resistance between HIV/AIDS and Malaria

While patients of human immunodeficiency virus/acquired immunodeficiency syndrome (HIV/AIDS) with advanced immunosuppression may augment the risk of malaria infection, the increase of malarila parasite density, and the failure of antimalarial treatments on one hand; acute malaria is found to temporarily increase HIV viral replication on the other hand. Recent conclusions of WHO on "Malaria and HIV/AIDS Interactions and Implications" resulted in attentions to obtain knowledge on interactions between HIV/AIDS and malaria as well as to reduce the consequences of dual infections (25). One of the agreements was to protect HIV-positive pregnant women with either sulfadoxine-pyrimethamine, or cotrimoxazole prophylaxis.

Copyright by Mahidol University

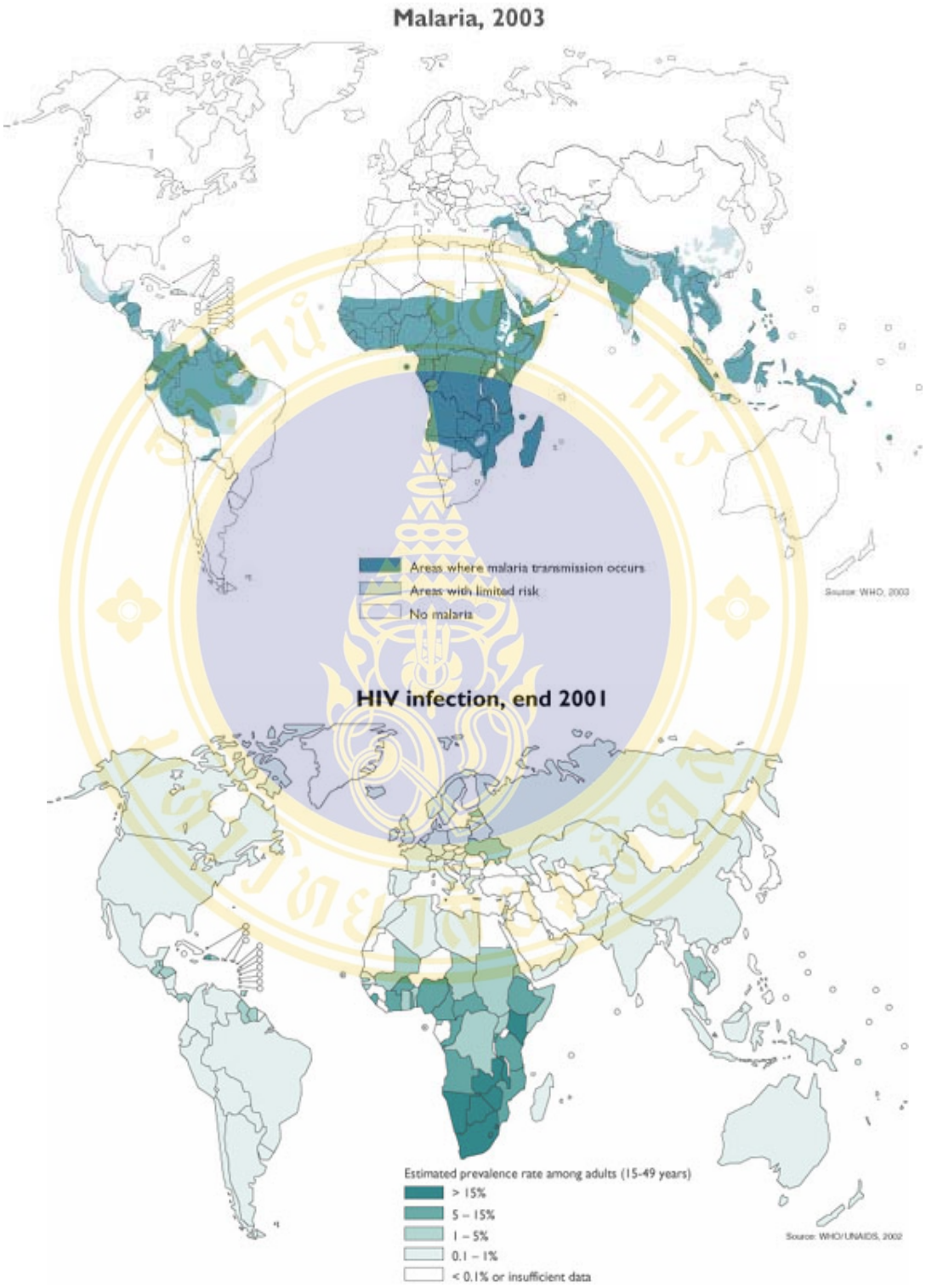

Figure 9 The areas with high emergence of malaria and HIV/AIDS. There is a wide geographical overlap, especially in sub-Saharan Africa and South/South-East Asia, where both diseases cause more than 4 million deaths per annum. Figures are available from http://www.who.int/ith/chapter05_01.html.

Copyright by Mahidol University

Sulfadoxine-pyrimethamine, known as Fansidar®, is one of the most widely available and affordable antimalarial combined treatments. Despite the potential drawback in the rapid emergence of resistant parasites when it is massively employed, sulfadoxine-pyrimethamine has been recommended as the first-line antimalarial drug throughout Africa (26), (27). Cotrimoxazole has been recommended by the World Health Organization to be used prophylactically against opportunistic infection in HIV patients (28), as well as children with respiratory symptoms (29).

These combined drugs share similarity by employing a combination of sulfa and antifolate to produce a synergistic blockade on folate pathway through DHPS and DHFR inhibition. Several evidences suggested that cotrimoxazole and sulfadoxine-pyrimethamine share extensive *in vitro* cross-resistance and cotrimoxazole prophylaxis might lead to the development of a cross-resistance between trimethoprim and pyrimethamine at the molecular level (30-33). Widespread use of cotrimoxazole could foster sulfadoxine-pyrimethamine resistance in *P. falciparum*, which might relate to similarity between these drug components (28).

It has been widely accepted that antifolate resistance in *P. falciparum* is due to mutations of the key amino acids of the enzyme DHFR, which results in either a decrease in the binding of inhibitors or the recovery of enzyme activity (34-37). Therefore, our attention has been made towards investigation of cross-resistance between pyrimethamine and trimethoprim by structural analysis of the enzyme *P. falciparum* dihydrofolate reductase's active site.

1.5 Structure of *Pf*-DHFR-TS in Complex with Trimethoprim

P. falciparum dihydrofolate reductase-thymidylate synthase (*Pf*-DHFR-TS) has been among a few well-defined target for antimalarial chemotherapy with good selectivity and high sensitivity. However, drug-resistant parasite has rapidly emerged. Thus, various structures of *Pf*-DHFR-TS in complex with different inhibitors are crucial for rational antimalarial drug design. Structural information obtained from *Pf*-

Copyright by Mahidol University

DHFR-TS in complex with trimethoprim not only leads us to a better understanding of drug resistant, but also provides us with other perspectives of trimethoprim selectivity.

Active site of plasmodial DHFR was significantly different from that of the human host. Hence, it allows for selective inhibition by antimalarial drugs. In addition, the malaria parasites found in infected erythrocyte contain very small amount of DHFR-TS, *i.e.* approximately 1,000 fold less than mammalian cells. Such low level of drug target would greatly enhance drug-sensitivity in the parasite because it could not suddenly replenish the drug-bound enzyme. Moreover, *Pf*-DHFR-TS is found to display an autologous translational control mechanisms to its cognate mRNA independently from the active site occupancy. Therefore, the enzyme that contains tight binding inhibitor could still block the translation of its cognate mRNA as well as an active enzyme (38).

The simple chemical reaction governed by DHFR, as shown in Figure 10, is believed to evolve the variability of DHFR structure among different species as well as in the rapid occurrence of drug-resistant parasite. Resistance to *P. falciparum* DHFR was most often found at amino acid residues 16, 51, 59, 108, and 164. Accumulation of mutations results in higher degree of resistance. The list of amino acid mutations with the corresponding drug resistant level is shown in Table 2.

Three X-ray structures of *Pf*-DHFR-TS have been elucidated. All amino acid mutations mentioned in Table 2 were found in the active site region of *Pf*-DHFR (39). Hence, the three-dimensional structures of *Pf*-DHFR-TS certainly provide some information about specificity and flexibility of *Pf*-DHFR active site which may lead to some information concerning drug resistance mechanisms.

Copyright by Mahidol University

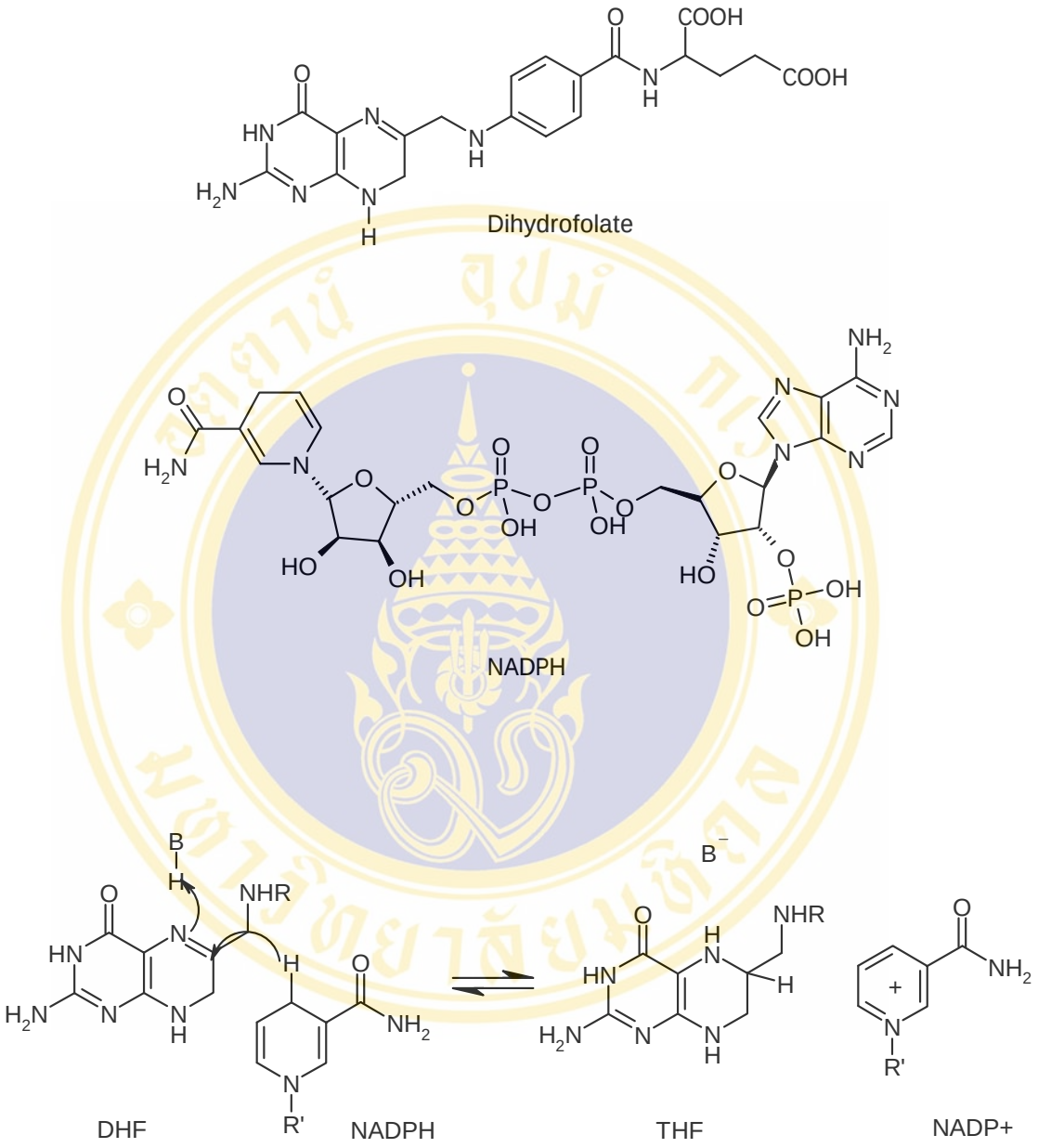

Figure 10 Chemical reaction catalyzed by dihydrofolate reductase. DHFR catalyzes the reduction of 7,8 dihydrofolate (DHF) to 5,6,7,8-tetrahydrofolate (THF) through a stereospecific hydride transfer from NADPH cofactor to C6 of the pterin ring with concurrent protonation at the N5 position. Chemical structure of DHF and NADPH are shown on the top and the middle panel, respectively. Figure reproduced from Benkovic, 2003 (40).

Copyright by Mahidol University

Table 2. List of mutants generated by cassette mutagenesis of wild-type synthetic *Pf*-DHFR domain, and also their corresponding field-isolate parasite strains with susceptibility towards pyrimethamine and cycloguanil. Table reproduced from Sirawaraporn, *et al.* 1997 (36); based on original evidences from Foote, *et al.* 1990 (41) and Peterson, *et al.* 1990 (35).

Construct	Field isolates with Equivalent mutation	Drug susceptibility	
		Pyrimathamine	Cycloguanil
Wild type	3D7, SL/D6	S	S
A16V*	-	-	-
N51I*	-	-	-
C59R*	-	-	-
S108N	HB3	MR	LR
S108T*	-	-	-
I164L*	-	-	-
A16V + S108T	FAC8, FAC3, UPA, FCB, It.G2.F6	S	HR
A16V+ S108N*	-	-	-
N51I + S108N	7G8, It.D12	MR	MR
C59R + S108N	K1, V1	MR	MR
N51I + C59R + S108N	W2	HR	MR
C59R + S108N + I164L	Cs1–2	HR	HR
N51I+C59R+S108N+ I164L	V1/S	HR	HR

* Constructs were not found in nature

S = sensitive; LR = low resistance; MR= moderate resistance; HR=High resistance.

Copyright by Mahidol University

1.6 Trimethoprim as a Potential *Pf*-DHFR-TS Binding Agent

Besides the urgency of cross-resistance induction to antimalarial drug, the structures of protozoal *Pf*-DHFR-TS with trimethoprim derivatives may lead to other perspectives of trimethoprim selectivity.

Trimethoprim is 100,000 times more inhibitory of *E. coli* DHFR than it is of human DHFR (12). Previous X-ray structural studies from the group of Matthews showed that trimethoprim binds differently at the active sites of chicken liver DHFR and *E. coli* DHFR (42). Matthews' generalization was that trimethoprim binds to "upper" binding sites of vertebrate DHFRs in the same binding mode as in chicken liver DHFR (Figure 11, top panel); while the "lower" sites make more favorable interactions in the bacterial DHFRs which resemble the *E. coli* DHFR binding mode (Figure 11, bottom panel) (43).

Such hypothesis was confirmed later by other crystal structures in complex with trimethoprim. The conformation of trimethoprims in mouse DHFR (44) and human DHFR (45) are similar to the upward conformation shown in the chicken liver active site. Trimethoprim conformation that occupies the lower binding site, as occurred in *E. coli* DHFR, was found in the bacterial *Mycobacterium tuberculosis* DHFR (46) and also the fungal *Pneumocystis carinii* DHFR (47). Hence, such geometrical differences give an answer to the question why trimethoprim could inhibit bacterial DHFRs but not vertebrate DHFRs.

The binding mode of trimethoprim in *P. falciparum* is an interesting issue. Trimethoprim does not bind to *P.falciparum* DHFR as tightly as bacterial DHFR, but it still exhibits a slight inhibitory effect on *P. falciparum*. The binding mode of trimethoprim in *P.falciparum* DHFR might provide a broader perspective on the available space that an inhibitor might occupy in the *P.falciparum* DHFR catalytic cleft. Such information can be a useful structural basis for rational drug design of novel *P. falciparum* DHFR's inhibitor.

Copyright by Mahidol University

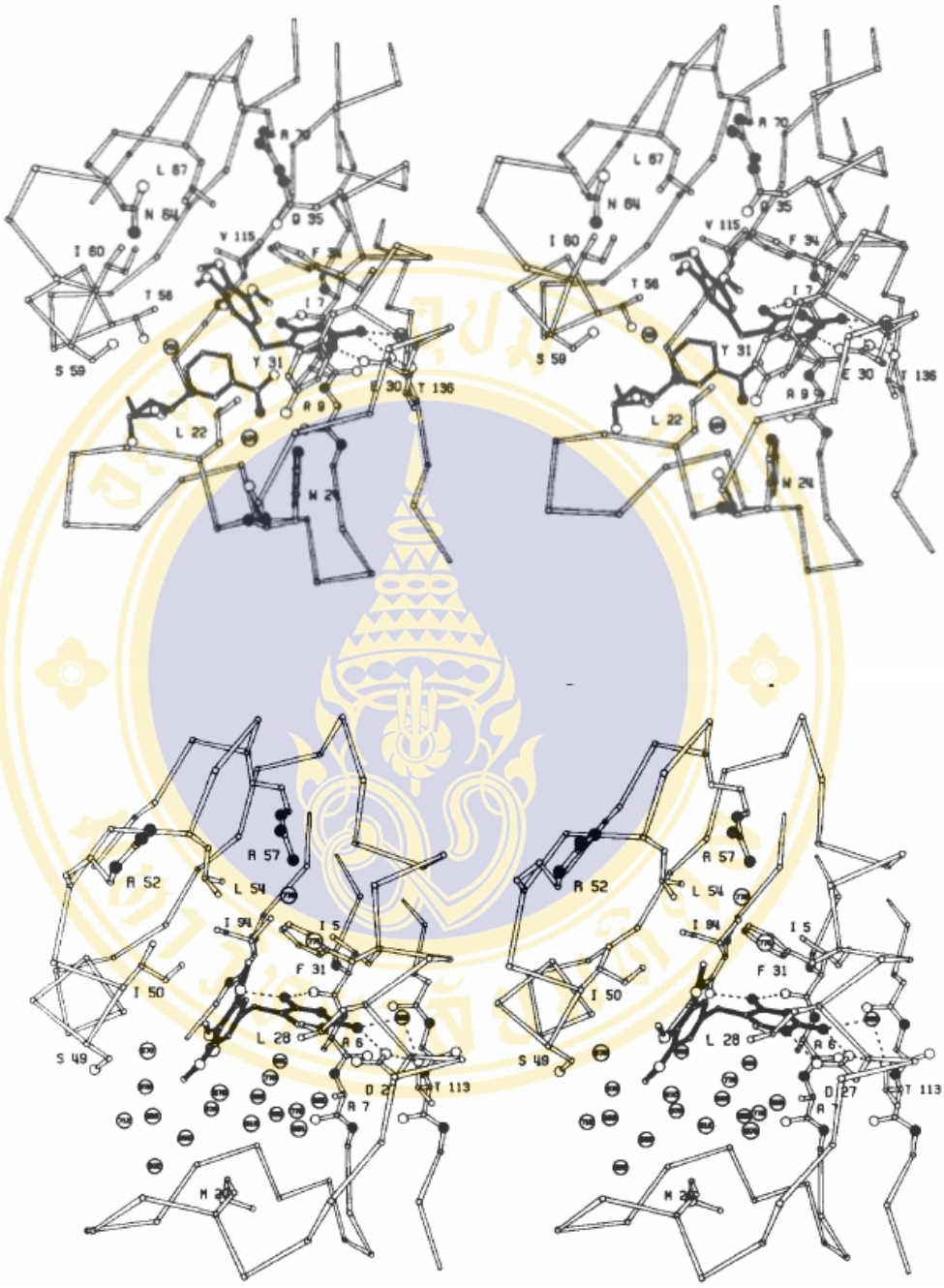

Figure 11 Stereo drawing of trimethoprim, a bacterial DHFR inhibitor, bound to chicken liver DHFR (top panel) and *E. Coli* DHFR (bottom panel). Trimethoprim is indicated by solid bonds, and protein by open bonds. Hydrogen bonds are shown by broken lines. The upward and downward conformation of trimethoprim was the main reason why trimethoprim inhibits bacterial DHFR much better than vertebrate DHFR (42).

Copyright by Mahidol University

Even though trimethoprim is not as effective as other antifolate drugs for malaria treatment, it shows an ability to bind to the enzyme *Pf*-DHFR-TS in sufficient affinity for crystallization experiment. Comparison between inhibition constants of pyrimethamine and trimethoprim is shown in Table 3.

Table 3 Inhibition constants of pyrimethamine and trimethoprim. K_i values of pyrimethamine and trimethoprim were referred from Tarnchompoo, *et al.* 2002 (48). The compound trimethoprim-39 and its K_i were obtained from Dr. Chawanee Sirichaiwat, see publication (49).

Compounds	K_i (nM)		$\frac{K_i \text{ C59R+S108N}}{K_i \text{ Wild-type}}$
	Wild-type (TM4/8.2)	C59R+S108N (K1CB1)	
Pyrimethamine	0.6 ± 0.2	53.9 ± 6.5	89.8
Trimethoprim	10.3 ± 0.5	242.1 ± 40.1	23.5
Trimethoprim-39	0.3 ± 0.0	2.2 ± 0.1	7.3

1.7 Protein Crystallization

To grow any protein crystals, the molecules of interest have to be brought to a supersaturated, thermodynamically unstable state, which they may return to equilibrium either by developing into a crystalline or amorphous phase. Besides having a protein with high concentration and free of contaminants, the protein has to be conformationally pure to allow crystallization. Since optimal stability of protein is restricted to narrow ionic strength, temperature and pH; protein crystallization requires a rather complex aqueous solution comparing to crystallization of small molecules.

Parameters affecting solubility and crystallization of proteins range from intrinsic physico-chemical parameters (*e.g.* concentration, purity, chemical reagents, temperature, time, pH, ionic strength, viscosity, pressure, interface effects to solid surface) to biochemical properties (*e.g.* conformational heterogeneity, denaturation,

Copyright by Mahidol University

substrates, cofactors, metal ions, reducing agents, detergents, and other impurities). In crystallization trials, the use of systematic controls of these factors is usually set up in combination with crystallization techniques that slowly increase protein saturation state. The use of salt and polyethylene glycol (PEG) for inducing crystallization are among the most popular protein crystallization approaches.

Salt plays a major role in protein solubility, which greatly affects crystallization. The effects of salts on protein solubility rely on a balance between protein-water, protein-salt, salt-water, and protein-protein interactions. Electrostatic interaction is predominant at low salt concentration, while hydrophobic interaction has more effect at high salt concentration.

At low ionic strength, the increase in salt concentration would increase protein solubility by shielding the protein from one another with an atmosphere of oppositely charged small ions. The increase in concentration of counterions which can help to dissolve a protein is referred to as 'salting-in'. At the extremely high ionic strength, however, solubility of the protein is governed mainly by hydrophobic effects. Since large amount of water is already taken up in the hydration shell of the counterions, increasing the salt concentration would exclude the protein out of solution. The term 'salting out' is used to describe the decrease in protein solubility as a result of high salt concentration. Solution additives employed for the purpose of salting out are called 'precipitants' (50).

Polyethylene glycol (PEG) is a classical crystallizing agent for soluble proteins. PEG has high viscosity which may prevent the protein from fast aggregation. Moreover, it is believed to act by competing with proteins for water molecules. At a given temperature, the solubility limit of the proteins depends on all constituents of the solution (*e.g.* PEG, detergent, protein, and salts). By increasing PEG concentration, the system will slowly approach this limit and the protein will eventually come out of the solution (51).

Copyright by Mahidol University

Crystallization experiment in this research was focused on crystallizing the protein *Pf*-DHFR-TS (K1CB1) complex using microbatch crystallization technique by finding optimum condition of ammonium acetate salt and polyethylene glycol with mean molecular weight of 4000 (PEG 4000) at pH 4.6, which was once a successful solution for this protein.

1.8 Protein Structure Determination using X-ray Crystallography

In order to have picture of a molecule with atomic resolution, the wavelength of light has to be smaller than the interatomic distance. The suitable wavelength is in range of 10^{-10} - 10^{-9} m, which falls in the wavelength range of X-ray. When a beam of X-rays is passed through a crystal and allowed to fall on a photographic plate, a central white spot is observed to be surrounded by a pattern of smaller spots that correspond to the scattering of X-rays from the crystal. This image is called a diffraction pattern, and each spot is called a reflection. Distance between reflections can be calculated to obtain dimensions of the unit cell, and the intensities of the reflections can be interpreted to generate the 3D-picture of electron clouds, hence the shape of individual molecules that constitute the unit cell.

In the crystal, atoms are arranged periodically into three dimensional array of unit cells alled lattice. Each unit cell of dimensions a, b, and c can be organized into families of planes with different orientations and spacing. The planes can be best described in relation to the unit cell by Miller indices *h*, *k*, and *l*, which define how many times each dimension was dissected by that family of planes. The family of planes may be thought of as sampling of the content of unit cell at regular intervals, just like serial cross-sections in microscopy. These imaginary planes produce reflections on the diffraction pattern at the positions reciprocal to where they dissect the crystal lattice, and with the intensities corresponding to the content of the unit cell.

From diffraction experiment, intensity and position of each reflection are measured, and its triple indices can be assigned based on the crystal space group. One reflection can be described in mathematical expression called a structure factor, $F_{(h,k,l)}$,

Copyright by Mahidol University

as a summation of scattering components from all atoms. Each term of structure factor, *f*, is the amplitude of the contribution of single atom *j* to reflection *hkl*.

$$F_{(h,k,l)} = \sum_{j=1}^{\text{atom}} f_j \, e^{[2\pi i \, (hx_j+ky_j+lz_j)]}$$

In other words, the structure factor that describes a reflection *hkl* is a Fourier series in which each term is the contribution of one atom, treated as a simple sphere of electron density. Assuming the amplitude f_j is scattered from electrons located at the position x_j, y_j, z_j in the unit cell, and occupies an infinitesimally small volume $\rho_{(x,y,z)}$. The structure factor would relate to a contour map of electron densities described by a Fourier series below:

$$\rho_{(x,y,z)} = \frac{1}{V} \sum_{h} \sum_{k} \sum_{l} F_{(h,k,l)} \, e^{[-2\pi i \, (hx+ky+lz)]}$$

where $\rho_{(x,y,z)}$ is the electron density at coordinate x, y, z of the unit cell

V is the unit cell volume

x, y, z are coordinates in the unit cell

h, k, l are indices of the reflection; its derivation (1/h,1/k,1/l) designating where corresponding lattice planes intersect the unit cell

$F_{(h,k,l)}$ is the structure factor

If the structure factors were known, the electron density in real structure can be calculated. However, structure factor $F_{(h,k,l)}$ is a wave created by the superposition of waves resulting from diffraction by all individual atoms; hence it posses amplitude, frequency, and phase. Measuring diffraction intensities can give the amplitude and the frequency can be derived from the Miller indices, but the phase $\alpha'_{(h,k,l)}$ of each reflection is not obtainable by the experiment.

Copyright by Mahidol University

The lack of experimental phase information is a major obstacle in electron density calculation, and is known as the phase problem. Formulation below is derived to simplify the phase $\alpha'_{(h,k,l)}$ in the electron density equation.

$$F_{(h,k,l)} = |F_{(h,k,l)}| \cdot e^{2\pi i \alpha'_{(h,k,l)}}$$

$$\rho_{(x,y,z)} = \frac{1}{V} \sum_h \sum_k \sum_l |F_{(h,k,l)}| \cdot e^{[-2\pi i (hx+ky+lz)]} \cdot e^{2\pi i \alpha'_{(h,k,l)}}$$

$$\rho_{(x,y,z)} = \frac{1}{V} \sum_h \sum_k \sum_l |F_{(h,k,l)}| \cdot e^{[-2\pi i (hx+ky+lz - \alpha'_{(h,k,l)})]}$$

where $\alpha'_{(h,k,l)}$ is the phase of the reflection h, k, l.

The phase problem can be tackled by various approaches depending on the available information about known structure of a similar protein family, and atoms in the crystal itself.

Copyright by Mahidol University

CHAPTER 2
OBJECTIVES

This research has an aim to find an X-ray structure of *Pf*-DHFR-TS in complex with trimethoprim in order to provide insights into interactions between the enzyme and trimethoprim inhibitor. Comparison between this complex structure and the previously published structures of pyrimethamine–complex (39) and also X-ray structure of trimethoprim which bind differently at the active sites of *E. coli* and chicken DHFR (42) may explain the molecular basis of cross-resistance between trimethoprim and pyrimethamine, and may also lead to new information in the development of a novel *Pf*-DHFR inhibitor.

2.1 Experimental Strategy

A protein has a very narrow range of condition to be crystallizable. The preparation and crystallization strategies, hence normally start from any available information on a similar protein. Since the available preparation protocol of *Pf*-DHFR-TS has been proven to allow the protein crystallization, the protein preparation protocol and also the crystallization reagents is based primarily on the *Pf*-DHFR-TS protocol published by Chitnumsub, *et al.* 2004 (52).

2.2 Specific Aims

1. To express and purify the protein *Pf*-DHFR-TS for crystallization.
2. To co-crystallize the enzyme *Pf*-DHFR-TS with dUMP, NADPH, and trimethoprim.
3. To obtain good X-ray diffraction data from the crystals that allows for 3D structure determination and refinement.
4. To analyze feature interaction of trimethoprim in the binding pocket of *Pf*-DHFR-TS.

Copyright by Mahidol University

CHAPTER 3
MATERIALS & METHODS

MATERIALS

A. Instruments

Centrifuge	SORVALL RC-5C
	SORVALL RC-5C Plus
Microcentrifuge	Biofuge pico, Heraeus
Fraction collector	Biotech AKTA *prime*, Amersham Pharmacia
French Press	SIM-AMICO
Electrophoresis chamber	Mini PROTEAN II Cell, Bio-Rad
Electrophoresis power supply	PowerPAC 300, Bio-Rad
Microscope	SZ-ST, Olympus
Shaker Incubator	Innova
Spectrophotometer	HEWLETT PACKARD 8453
X-ray machine	Rigaku/MSC rotating anode generator equipped with an R-Axis IV++ image-plate area detector

B. Biochemical Apparatuses

Cover glass

Centricon YM-10 (Amicon, USA)

Centriprep YM-10 (Amicon, USA)

Quartz cuvette 0.5 ml

Plastic cuvettes 1 ml

Copyright by Mahidol University

Vivaspin 0.5 ml, M.W. cut-off 10 kDa (Sartorious, Germany)

Vivaspin 20 ml, M.W. cut-off 30 kDa (Sartorius, Germany)

Millipore filter 0.22 μm GV(Durapore, Ireland)

Millipore filter 0.45 μm HV (Durapore, Ireland)

Flask for 1 litre–culture media (Pyrex)

Gel filtration column, size 1.4 cm × 33 cm

T.C. Terasaki plate, 60 well with lid (NUNC, Denmark)

Q-Sepharose column (Amersham Pharmacia)

Methotrexate (MTX) – Sepharose CL-6B; ~1 μmol/ml gel

Hanging drop crystallization tray

Sephacryl S-200 HR resin, M.W. 5,000-250,000

C. Chemicals and Reagents

All chemicals and reagents used in this study were of analytical grade or the highest purity commercially available. Water used for all experiments was of double distilled. For crystallization experiment, all prepared reagents were nano-pore filtered and stored at 4 ºC, degassed, and capped in glass bottle before use.

Name of Chemicals	Company/Source
Acrylamide PAGE	Pharmacia Biotech
Ammonium acetate (CH_3COONH_4)	Merck
Ammonium persulphate	Pharmacia Biotech
Ampicillin sodium (anhydrous)	T. P. drug laboratories
Acetic acid (glacial)	Merck
Bacteriological peptone	Scharlau
Bis-acrylamide (N, N'-methylenebisacrylamide)	Amersham Biosciences
Bromophenol blue	BioBasic
Coomassie Brilliant blue R-250	Sigma
Baby oil, with vitamin E	PZ Cussons, Thailand
Chloramphenicol	Sigma

Copyright by Mahidol University

Dithiothreitol (DTT)	BioBasic
Dimethylsulfoxide (DMSO) [$(CH_3)_2SO$]	Merck
EDTA	USB, Amersham Life Science
Ethanol, absolute	Merck
Glycerol [$C_3H_8O_3$]	Carlo Erba
Glycine	Scharlau
Hydrochloric acid [HCl]	Merck
Isopropyl-β-D-thiogalactoside (IPTG)	BioBasic
Standard Protein Marker	Amersham Biosciences
β-mercaptoethanol (BMCE)	Amersham Biosciences
Methanol, absolute [CH_3OH]	Merck
NADPH	Sigma
Polyethylene glycol (mean M.W. 4000)	Merck
Sodium acetate trihydrate [CH_3COONa]	Merck
Sodium chloride [NACl]	Merck
Sodium hydroxide [NaOH]	Merck
Sodium dodecyl sulfate (SDS)	Sigma
Trichloroacetic acid	Sigma
Tris-[hydroxymethyl]-aminomethane	Scharlau
N,N,N′,N′-tetramethylene-ethylenediamine (TEMED)	USB
Yeast extracts	Scharlau

D. Protein Source

The *E. coli* BL-21 (DE3) pLysS cells harbouring *Pf*-DHFR-TS (K1CB1) was kindly provided by the Protein-Ligand Engineering and Molecular Biology laboratory, BIOTEC. A single colony was selected for 4 hour-culturing in LB-broths containing 100 µg/ml ampicillin and 34 µg/ml chloramphenicol. The 1 ml-aliquot cells were stored in 15% glycerol at -80 ºC.

Copyright by Mahidol University

METHODS

Summary

In this experiment, the double mutation (C59R+S108N) K1CB1 *Pf*-DHFR-TS was selected as the protein candidate mainly because of the ease its purification.

E. coli BL-21 (DE3) pLysS cells harbouring *Pf*-DHFR-TS (K1CB1) gene was grown at 37ºC until OD_{600} reached 0.8, then the protein expression was induced by 0.4 mM IPTG induction at 20ºC for 20 hours. *E. coli* cell paste was harvested and then lyzed using French Press, and *Pf*-DHFR-TS can be extracted from supernatant. Purification was achieved by affinity chromatography using Methotrexate–Sepharose CL-6B column. Then the protein was purified further either by gel filtration or by anion exchange chromatography. The protein was concentrated using 30 kDa cut-off concentrators until OD_{280} was approximately 10. The concentrated protein was kept at -80 ºC for subsequent crystallization experiments.

Crystallization was done in microbatch under baby-oil containing vitamin E. Co-crystallization of *Pf*-DHFR-TS with dUMP, NADPH, and trimethoprim was first tried at 22 ºC in sodium acetate buffer (pH 4.6) using ammonium acetate and PEG 4000 as precipitants, since it is the condition that once was successful with *Pf*-DHFR-TS with dUMP, NADPH, and pyrimethamine. The crystal growth was optimized to obtain larger size crystals and stabilized in sitting drop tray before mounting. X-ray diffraction data were collected at -160ºC with the R-Axis IV++ image plate detector. Difference Fourier technique was employed for structure determination.

Copyright by Mahidol University

3.1 Protein Preparation

3.1.1 Cell Culture

The *Pf*-DHFR-TS protein was overexpressed from *E. coli* BL21(DE3) pLysS cells harboring the pET17b–*Pf*-DHFR-TS (K1CB1) gene. Pre-culture from a single colony was grown overnight at 37 ºC in 200 ml–Luria-Bertani (LB) broth containing 100 µg/ml ampicillin and 34 µg/ml chloramphenicol with 250 rpm shaking. Fifteen mililitre of the overnight pre-culture was added into each flask of 1 litre - LB broth containing 100 µg/ml of ampicillin.

Cell cultures were grown in shaker incubator at 37 ºC with 250 rpm shaking until OD_{600} reached about 0.8, using LB-broth as a blank. After that, protein expression in each flask was induced with 0.4 mM isopropyl-β-thiogalactoside (IPTG). The cells were continued to grow in 20 ºC shaker incubator for 20 hrs. After that, the cells were harvested using 10,500 × g centrifugation at 4 ºC for 10 minute, and resuspended in minimal amount of cold Buffer A [0.1 mM EDTA, 10 mM DTT, 20 mM potassium phosphate buffer pH 7.2, 20% (v/v) glycerol, 50 mM KCl], so that the final volume of cell suspension was less than 40 ml.

Cell suspension was disrupted twice using French Press at 1500 PSI. Cell lysate was clarified with 27,000 × g centrifugation at 4 ºC for 1 hr. The activity of DHFR could be determined from the supernatant and was assigned as 100% activity at this point (see detail in section 3.1.4A).

3.1.2 Protein Purification

Purification of *Pf*-DHFR-TS can be achieved by affinity chromatography using a DHFR's inhibitor, methotrexate, as a biospecific ligand. Methotrexate exhibits specific and reversible binding affinity to the protein DHFR, hence can be an efficient binding substance when attached to the chromatographic bed material. Desorption is

Copyright by Mahidol University

performed using the actual substrate of the enzyme, dihydrofolate, as an eluent to compete with methotrexate binding on the stationary phase.

All experiments dealing with *Pf*-DHFR-TS protein were carried out in 4 ºC cold box. Methotrexate–Sepharose CL-6B column (MTX-affinity column) was prepared by linking methotrexate to Sepharose CL-6B resin (~1 µmol/ml gel) according to the chemical method described by Meek *et al.*, 1985 (53)

The column was pre-equilibrated with Buffer A [0.1 mM EDTA, 10 mM DTT, 20 mM potassium phosphate buffer pH 7.2, 20% (v/v) glycerol, 50 mM KCl]. Crude protein extract was loaded to the pre-equilibrated column, and circulated at a flow rate of 1.0 ml/min for about 36 hours. Then the MTX-affinity column flow-through was assayed for the decreasing of DHFR activity, until the percentage of MTX bound-enzyme reached 80-90%. Non-specifically bound protein was removed by washing the column with ~ 3 litres of Buffer A containing a higher salt concentration, 0.5 M KCl. Once no more protein was detected in the effluent, *i.e.* OD_{280} < 0.01, KCl concentration in the column was readjusted to 50 mM with Buffer A.

The enzyme bound to MTX-affinity column was obtained by 36-hour-equilibrating, and then eluting the column with 200 ml of Buffer B [0.1 mM EDTA, 10 mM DTT, 50 mM TES pH 8.2, 20% (v/v) glycerol, and 50 mM KCl] containing 4 mM of dihydrofolate (DHF), which was prepared according to the method of Friedkin *et al.,* 1963 (54). Eluted fractions were assayed for DHFR activity (see detail in section 3.1.4A), and the active fractions were pooled and concentrated at 3,500 × g using Vivaspin-20 concentrator (M.W. cut-off 30 kDa). While concentrating, DHF in the eluted enzyme was partially removed by exchanging with Buffer B. The enzyme DHFR-TS was further purified by either gel filtration, or ion exchange chromatography.

Copyright by Mahidol University

A. Purification by Gel Filtration Chromatography

Gel filtration chromatography separates proteins with differences in molecular size. Separation depends on the different abilities of sample molecules to enter the porous matrix of stationary phase. Smaller molecules would take more sieving time than the larger ones because they spend a larger proportion of time in the stationary phase. The samples can be eluted using single buffer system without a gradient requirement. Because sample volume has a strong influence on the speed and resolution of separation, gel filtration chromatography is ideal for the final purification step when the sample volume has been reduced to less than 5% of the total column volume (55).

To further purify *Pf*-DHFR-TS by gel filtration chromatography, Sephacryl S-200 gel filtration column (diameter 1.4 cm × height 33 cm) was pre-equilibrated with Buffer A, with 150 mM KCl. The protein was concentrated to about 1 ml and filtered through 0.45 μm Millipore filter before loaded to the column. The column was eluted at a flow rate of 0.5 ml/min and 3 ml of effluent was collected in each small fraction tube. All fractions were determined for the presence of proteins spectrophotometrically by OD_{280} measurement. Fractions presenting the absorbance at 280 nm were analyzed by 10% gel SDS-PAGE (see detail in section 3.1.4B). The fractions containing *Pf*-DHFR-TS, judged by the presence of a large 72 kDa band, were collected as the main pool for subsequent steps as described in the section 3.1.3.

B. Purification by Ion Exchange Chromatography

Ion exchange chromatography can be used to separate proteins with differences in charge. It offers a high resolution of separation with high sample loading capacity (55). The separation is based on the reversible interaction between a charged protein and the oppositely charged chromatographic column medium.

Q-Sepharose column was used in this experiment. It is a strong anion exchanger which can be fully charged over a broad pH range, pH 2-12 (55). Above

Copyright by Mahidol University

their isoelectric points, proteins are negatively charged and bind to the anion exchanger as they are loaded onto the column. The salt concentration can then be altered so that the bound substances are eluted differently.

The column was equilibrated with Buffer B with no KCl [0.1 mM EDTA, 10 mM DTT, 50 mM TES pH 8.2, 20% (v/v) glycerol]. A linear gradient of Buffer B (with 0–0.4 M KCl) was applied at a flow rate of 1 ml/min; 6 ml of the effluent were collected in each fraction tube. The fractions containing proteins, determined by OD_{280} measurement, were assayed for DHFR activity as described in section 3.1.4A. Protein sample from every 2 fractions were selected for analysis using 12.5% SDS-PAGE. As the concentration of protein at this step was so low, 200 µl of the protein sample were precipitated with 40 µl of 50% trichloroacetic acid. The precipitates were washed 3 times and dissolved in a small volume of SDS-PAGE sample buffer before used, as described in section 3.1.4B. Fractions contianing *Pf*-DHFR-TS band of 72 kDa were pooled for subsequent concentration.

3.1.3 Protein Concentration

Various types of concentrators (*e.g.* Centriprep, Centricon, Vivaspin) were employed depending on the volume to be concentrated. Centrifugation was done at 4ºC with the maximum speed applicable for each concentrator. The pooled protein was concentrated until the final protein concentration reached about 10 mg/ml (see detail in section 3.1.4C). Concentrated protein was aliquoted into microfuge tubes and centrifuged at 10,500 ×g for 10 minutes to discard precipitates. The supernate were aliquoted into a new microfuge tube before storage at -80 ºC for subsequent crystallization experiments.

Copyright by Mahidol University

3.1.4 Protein Characterization

A. Determination of DHFR Activity

The activity of DHFR can be determined spectrophotometrically by monitoring the decrease in absorbance at 340 nm. Due to contributions by both the oxidation of NADPH and the reduction of dihydrofolate, the molar extinction coefficient change is mole-averaged combination of the two half reactions, which is 12,300 $M^{-1}cm^{-1}$ (56).

The chemical reaction is shown below;

$$DHFR + NADPH + DHF \rightleftharpoons NADP^{+} + THF$$

Using ε_{340} =12,300 $M^{-1}cm^{-1}$, DHFR activity assayed at 25 ºC in a 1 cm-path length cuvette can be calculated from the following equation:

$$\text{DHFR activity} = -\frac{\Delta OD}{12.3 \times \text{enzyme vol. in milliliter}} \quad \mu mol \cdot min^{-1} \cdot ml^{-1}$$

Standard assay in 1 ml-reaction contained 100 µM DHF, 100 µM NADPH, 1 mg/ml bovine serum albumin, 75 mM β-mercaptoethanol, 50 mM TES (pH 7.0), 0.1 mM EDTA, and about 0.01 unit of enzyme. The absorption at 340 nm of each plastic cuvette containing all the described components except for enzyme was set to zero before initiating the reaction by addition of DHFR sample.

Copyright by Mahidol University

The amount of enzyme can be calculated from the formulation below. One unit of enzyme activity is defined as the amount of enzyme required to catalyze the reduction of 1 μmol of substrate per minute at 25 ºC.

Unit of enzyme = DHFR activity × total vol.

B. Sodium Dodecyl Sulfate–Polyacrylamide Gel Electrophoresis

Electrophoresis is the process of moving charged molecules in solution by applying an electric field across a porous medium. Since charged molecules in electric field move through the pores to the electrode of opposite charge with mobility dependent on their charges, shapes, and sizes, electrophoresis has been extensively used for molecular separation. All sodium dodecylsulfate polyacrylamide gel electrophoresis (SDS-PAGE) analysis in this research work was based on the standard Laemmli SDS protocol, which is a discontinuous denaturing system (57).

In SDS-PAGE separations, migration is determined not by intrinsic charge but by molecular weight of polypeptides. Sodium dodecylsulphate (SDS) is an anionic detergent that denatures proteins by wrapping the hydrophobic tail around the polypeptide backbone and gives the polypeptide a uniform negative charge per unit length. SDS together with a reducing agent, such as dithiothreitol (DTT), can disrupt protein subunit that are attached by disulfide bonds, hydrogen bonds, hydrophobic interactions, and unfold the protein to flexible rods. Hence the proteins can be separated by molecular weight, which is a function of polypeptide chain length (58).

Polyacrylamide gel is formed by a free-radical catalyzed reaction, using ammonium persulphate (APS) as the initiator peroxide and the quaternary amine, N,N,N′,N′-tetramethylene-ethylenediamine (TEMED), as catalyst. Acrylamide and

Copyright by Mahidol University

cross linker, N,N´-methylenebisacrylamide, copolymerize into long chains that are covalently cross-linked, which serves as a porous matrix to sieve proteins. The average pore size is determined by the amount of cross-linker and total concentration of acrylamide. In discontinuous system, the treated proteins were concentrated into very thin zone on the stacking gel because of the higher percentage of gel and higher pH in the separating gel, providing a band sharpening effect.

The resolving gel and the stacking gel were prepared using the ingredients as shown in Table 4. To visualize 72 kDa major band as well as ~40 kDa minor bands of *Pf*-DHFR-TS, the polyacrylamide gel prepared using 12.5% acrylamide is more appropriate than the one containing 10% acrylamide since the separation size range of 12.5% SDS-PAGE is between 14–66 kDa. However, larger proteins would fail to move significantly into the resolving gel containing such high percentage of acrylamide (58).

Table 4. Final concentration of ingredients in discontinuous SDS-PAGE gel

Ingredients	Resolving gel		Stacking gel
Acrylamide [1:29] (w/v)	10.0 %(T)	12.5 %(T)	3.9 %
SDS (w/v)	0.1 %	0.1 %	0.1 %
Tris-HCl pH 8.8	0.375 M	0.375 M	-
Tris-HCl pH 6.8	-	-	0.126 M
APS (w/v)	0.05 %	0.05 %	0.05 %
TEMED (v/v)	0.1 %	0.1 %	0.1 %

Protein samples were solubilized with sample solubilizing buffer composed of 2% SDS, 10% glycerol, 0.1 M DTT and 20 µl saturated bromphenol blue in 0.08 M Tris-HCl pH 6.8. The dissolved sample was boiled in heat box for 5 minutes to ensure the complete denaturation and let cool before loading into the wells.

Copyright by Mahidol University

Electrophoresis was run at 200 Volt, constant voltage, using 300 ml of running buffer consisted of 25 mM Tris, 192 mM glycine and 0.1% (w/v) SDS, with the final pH ~8.3. The separation was terminated when the dye front of bromphenol blue started to disperse into the running solution. To visualize the proteins, the gel was then stained in Coomassie Brilliant Blue staining solution [0.1% Coomassie Brilliant Blue R-250, 40% methanol, and 10% acetic acid] for about 1 hr, before transferring to destaining solution [40% methanol, 10% acetic acid]. Gentle shaking was applied and destaining solution was changed until the background of the gel was clear. The gel was washed thoroughly with water and kept in cellophanes until dry.

The low molecular weight protein standard marker containing 80% marker and 20% dye was loaded in all gel. Standard protein marker used comprised phosphorylase B (94 kDa), bovine serum albumin (67 kDa), ovalbumin (43 kDa), carbonic anhydrase (30 kDa). soybean trypsin inhibitor (20.1 kDa) and lysozyme (14.4 kDa).

C. Determination of Protein Concentration

Concentration of the protein was estimated by direct measurement of ultraviolet absorption at 280 nm. At this wavelength, the absorbance would depend on the presence of aromatic amino acids in the protein sample (59). Theoretical molar absorption coefficients ε of polypeptides at 280 nm can be calculated from tryptophan and tyrosine content using:

$$\varepsilon_{280\ nm} = 5{,}690\ n_w + 1{,}280\ n_y$$

where 5,690 and 1,280 are molar absorption coefficients at 280 nm of tryptophan and tyrosine, n_w and n_y are the numbers of tryptophan and tyrosine residues, respectively (60).

Copyright by Mahidol University

According to amino acid sequence of the full length *Pf*-DHFR-TS, there are 38 tyrosine, and 6 tryptophan residues, hence:

$$\varepsilon_{280\ nm}\ (Pf\text{-DHFR-TS}) = (5{,}690 \times 6) + (1{,}280 \times 38)$$
$$= 82{,}780 \quad M^{-1}cm^{-1}.$$

From the theoretical $\varepsilon_{280\ nm}$ calculated above, the concentration of protein can be obtained from:

$$c\ (mg/ml) = OD_{280} \times (M.W. / \varepsilon_{280\ nm})$$
$$= OD_{280} \times (72{,}000 / 82{,}780)$$
$$= OD_{280} \times 0.87$$

Therefore, it can be assumed that 1 unit of OD_{280} is equivalent to 0.87 mg/ml.

A blank sample used in each round of protein concentration experiment was the concentrators' flow-through solution, which was expected to contain all components of the same concentration as in the sample, except for protein with molecular weight above 30 kDa-cut off. All measurements were done at room temperature in 0.5 ml quartz cuvette of 1 cm-path length. Since the concentration of protein was beyond the reliable limit of the instrument, *i.e.* $OD_{280} \geq 1.0$, the measurement was achieved by 500-time dilution.

Copyright by Mahidol University

3.2 Crystallization of *Pf*-DHFR-TS

3.2.1 Preparation of Crystallizing Agents

All the stock solutions for crystallization were prepared from the purest chemical grade available and double-distilled water. The prepared solution was filtered and degased under vacuum for 30 minutes and stored at 4ºC. Summary of the stock solution is shown in Table 5.

Table 5. Summary of crystallizing agents stock solutions

Stock Solution	Concentration	Remark
PEG 4000	50% (w/v)	Viscous precipitant, mean M.W. = 4000
Ammonium acetate	2 M	Salting precipitant
Sodium acetate	1 M	Buffer (pH 4.6)

Polyethylene glycol (PEG) is available in a variety of polymeric range; the one used in this experiment has mean molecular weight of 4000 Da. Viscosity of PEG often leads to pipetting errors; therefore, pipetting was done as slowly as possible and the tip was kept under solution long enough to ensure that the required volume had reached.

The pH of sodium acetate buffer was adjusted to 4.6 and its concentration was kept constant at 0.1 M for all crystallization trials. Concentrations of PEG 4000 and ammonium acetate were varied to obtain gradient of conditions. Promising condition was prepared based on results obtained from the previous crystallization trial.

Copyright by Mahidol University

3.2.2 Preparation of Protein Mixture for Crystallization

In order to have trimethoprim bind to all the DHFR active sites, the concentration of trimethoprim should be greater than final concentration of enzymes and should also be much higher than its K_i. Because solubility of trimethoprim in water is less than 1 mg/ml, its stock cannot be prepared in aqueous solution. A more appropriate solvent to dissolve trimethoprim is dimethyl sulfoxide (DMSO), which has been reported to dissolve more than 100 mg of trimethoprim per 1 ml (61). DMSO can also acts as precipitant by lowering the dielectric constant of the solution, hence the final DMSO concentration must be less than 5% in crystallization drop.

Nicotinamide adenine dinucleotide phosphate (NADPH) is a cofactor of the enzyme dihydrofolate reductase and deoxyuridine monophosphate (dUMP) is the substrate of the enzyme thymidylate synthase. Both ligands should be included to enhance the protein stability. Therefore, the concentration of each should be more than the concentration of protein – enough to ensure that all active sites of both enzymes were occupied.

DTT is a reducing agent used to prevent the oxidation of free sulfhydryl residues in the protein. Such oxidation can lead to non-specific aggregation of the sample, sample heterogeneity, and denaturation of the sample. DTT has two sulfhydryl groups and last about three to seven days in a typical crystallization experiment (62). Hence, DTT was freshly prepared every time before used. Concentration commonly used for protein crystallization was in the range of 1 to 10 mM per crystallization drop.

The protein sample was prepared with final concentration of *Pf*-DHFR-TS (K1CB1) ~ 0.1 mM in 1 mM trimethoprim, 0.875 mM NADPH, 0.875 mM dUMP, 12.5 mM DTT, and 2.5% DMSO for all crystallization experiments as shown in Table 6. All components, except for trimethoprim, were pipetted into the microfuge tube containing protein sample, spun down, and mixed thoroughly. Then trimethoprim were added, mixed well, and incubated for 10 minutes. After that, the solution was

Copyright by Mahidol University

centrifuged at room temperature for 10 minutes to remove invisible protein aggregates, and immediately used in microbatch crystallization.

Table 6. Summary of protein mixture solutions.

Stock Solution	Stock concentration	Final concentration
Trimethoprim*	40 mM	1 mM
NADPH	20 mM	0.875 mM
dUMP	20 mM	0.875 mM
DTT	1 M	12.5 mM
DMSO	100%	2.5%

*Trimethoprim-39, an analog of trimethoprim synthesized by Dr. Chawanee Sirichaiwat (49), was used instead of trimethoprim in one step of protein crystallization trial.

3.2.3 Microbatch Crystallization

Microbatch technique is employed for protein crystallization because of its advantages in easy set up, good reproducibility and small requirement of protein sample (63, 64). Unlike other crystallization techniques, the batch techniques are set up and incubated under oil. Using paraffin oil would prevent evaporation and uncontrolled concentration changes which results in the good reproducibility, while using oils that are slightly soluble in water result in gradual protein concentration as it permits water in the crystallization trial droplet to diffuse through the oil (65). Successful batch crystallization was accomplished when the drop contains a level of salt or other precipitant saturation very slightly less than that at which the protein precipitates.

For this experiment, the T.C. Terasaki Plate, 60 well with lid, was used for setting up the microbatch technique. The tray was filled with 6 ml of baby oil (Cussons' baby oil, PZ Cussons, Thailand), which allows water in the drop to diffuse

Copyright by Mahidol University

out. To avoid shock nucleation, protein sample (1 µl per drop) was first pipetted into each well under oil, and then 1 µl of precipitant was added to the same drop. The microbatch tray was kept in a 22ºC temperature incubator for three days before the first observation.

Crystal observation was performed every couple days until the crystal was harvested. Each well of crystallization tray was observed under a dissecting stereo-zoom microscope. The tray was handled gently and observed quickly, as the light source could warm up the microscope stage and affect temperature of the drops. Crystallization droplets were examined thoroughly from the surface in full depth. Record of each condition was kept by both text explanation and picture taken.

3.2.4 Optimizing the Crystal Growth

In general, protein crystals with a length of 0.2-0.5 mm are most suitable size for diffraction experiment. Diffraction from small crystal tends to be weaker, thus requiring longer exposure time and possibly resulting in poorer resolution. A large crystal may also generate problems associated with absorption of X-rays and non-uniform freezing which leads to crystalline ice formation during data collection (66). After crystals were observed, the crystallization condition has to be optimized to get a crystal big enough for X-ray diffraction.

Crystallization trial in the first batch was aimed to cover all the possible range of PEG and salt concentrations, so precipitants in the first tray were screened in large step size. Concentration of ammonium acetate (CH_3COONH_4) was varied from 0 to 0.4 M, while concentration of PEG 4000 was varied from 20% to 28% (w/v) as shown in Figure 12. A negative control experiment was set up using the same conditions as those drops in the third row [24%PEG 4000 and varying salt concentration], except for the protein which was replaced with 1 mM trimethoprim in the flow-through solution. These negative controls might provide an idea whether or not the crystal obtained was actually from undesired components, for instance trimethoprim, or ammonium salt.

Copyright by Mahidol University

Once a crystal was observed, concentrations of CH_3COONH_4 and PEG 4000 around the successful condition were refined further, with smaller concentration step. Crystallization conditions were optimized until crystals with sufficient size for diffraction experiment were obtained.

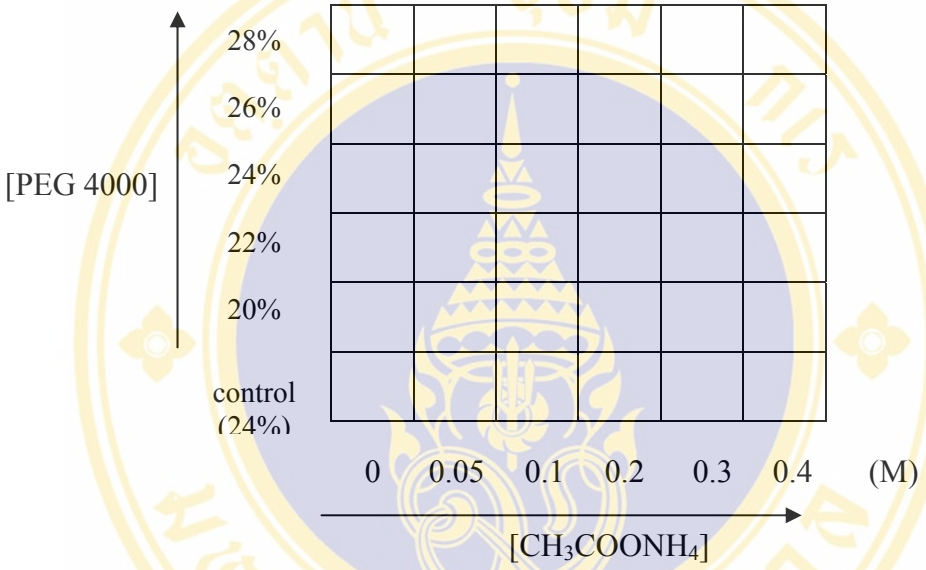

Figure 12 Illustration of the first crystallization trial conditions. The concentration of CH_3COONH_4 was increased in each subsequent column, while the concentration of PEG 4000 was reduced from the top down. The 6th row is a negative control experiment which comprised the same components as the 3rd row condition, but protein solution was replaced by trimethoprim dissolved in concentrator flow-through.

3.2.5 Crystal Selection

To select crystals for diffraction experiment, magnification of microscope in the range of 10x to 40x is most suitable as crystals with sizes that can not be seen with such magnification are probably not going to diffract X-rays well enough for data collection. Crystals with sharp edges probably diffract X-rays better than the other

Copyright by Mahidol University

ones. Beside the size and the morphology, quality comparison between crystals and also discrimination between microcrystals and precipitates can be made by observing its birefringence.

Birefringence, or double refraction, is the effect that occurs when each light ray splits into two components with different speeds and angles as it passes through a birefringent material. For crystal growers, the term birefringence is used to describe the colorful display produced by crystals when polarized light passed through the crystals. When the crystal is positioned between two polarizing filters, the color and the intensity of transmitted light can be changed as the polarizing filter is rotated (62). Greater birefringence phenomenon should imply better molecular organization within the protein crystal.

All the microbatch well containing crystals were examined under a stereo-zoom dissecting microscope, equipped with a crossed polarizing attachment. The big crystals with sharp edges and good birefringence were selected for storage prior to diffraction experiment.

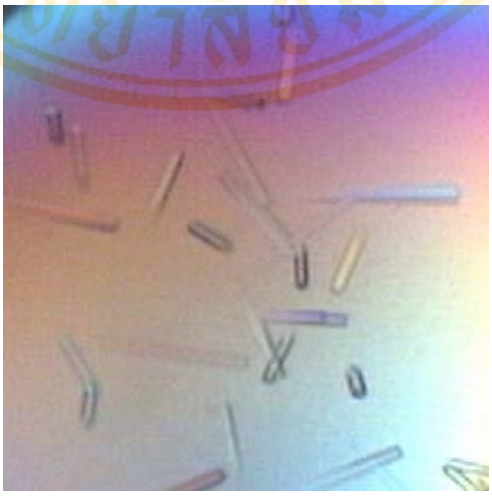

Figure 13 Birefringence of the crystals. Picture taken from the well using 15% ammonium acetate, and 0.8 M PEG 4000 precipitant from the third tray of crystallization trial

Copyright by Mahidol University

3.2.6 Crystal Handling and Storage

The crystals need to be harvested from the microbatch well since the water is continually dispersed out to the oil which results in shrinkage of the drop. When the volume is decreased, salts, PEG, and proteins would precipitate. Moreover, some denatured protein can form a thick film on the crystal, which would interfere with diffraction.

Once the crystals were harvested, they need to be stabilized in the preserving solution which contains higher concentration of ammonium acetate and PEG 4000 than ones that the crystals were crystallized in order to ensure that such solution would not solubilize them. A hanging-drop crystallization tray containing 24 wells with diameter 16 mm was used for crystal storage. Each well provides silicon grease around the rim, which allows the system to be sealed with a cover glass.

Selected crystals were picked up under a light microscope using a magnification of 10x. The volume of preserving solution [0.1 M CH_3COONa 30% (w/v) PEG 4000, 1.2 M CH_3COONH_4] in one chamber should be enough to completely cover the crystal surface. If a crystal was adhering to the wall of the microbatch, it was gently detached by withdrawing liquid from the drop and gently ejecting it onto a chosen crystal. When the crystal can hardly be dislodged, it was removed with a thin glass needle, made from broken dropper by slowly stretching the glass rod on direct flame. Crystals with branching were also carefully splitted with these glass needles.

Each crystal was positioned away from one another to avoid accidental destruction when pipetting a crystal nearby. Each reservoir chamber was sealed with a cover glass and the tray was stored in 22°C incubator. Reducing agent, 1 M DTT, was directly added to the well in 1:10 volume proportion and replenished once a week.

Copyright by Mahidol University

3.3 Data Collection and Processing

3.3.1 Crystal Mounting for Cryo-crystallography

A protein crystal contains large proportion of water, which could destroy the internal structure when dried out. When a crystal is put on X-ray beam, special mounting method is required to maintain the internal mother liquor as if the crystal is in the crystallization drop where it grew and also to prevent crystallization of components of the mother liquor.

Cryo-crystallography is a method to collect data under very low temperature. This technique could increase the life-time of the protein crystals by reducing radiation damage during data collection (67) and also increase the internal order of parts of the protein which are mobile at room temperature (68). Cryo-protective agent used in this experiment was glycerol which is the most popular cryo-protectant (69) in combination with chemical components in the preserving solution.

Various combination of preserving solution and glycerol was tested in order to preserve crystal integrity by obtaining a transition from water to vitreous ice (70). In order to optimize cryoprotectant, crystal was pipetted out from a preserving chamber by cryo-loop, and immersed in the trial cryoprotective solution dropped on a cover glass. Then the crystal was carefully scooped up with a cryo-loop. The loop with the crystal was flash-frozen by rapidly placing it onto the goniometer head while the cold nitrogen stream (-160ºC) was blocked with a plastic card. Crystal in the loop would be frozen immediately when the card was removed.

If the cryoprotective solution on the loop became opaque, the crystalline ice would give a powder diffraction pattern of water crystal, or ice-rings, reflecting an undesirable cryoprotectant condition. Various conditions were attempted until the cryoprotectant formed transparent ice which did not result in dark circular shading on the diffraction pattern.

Copyright by Mahidol University

3.3.2 Data Collection

Before data collection, position of the direct X-rays beam was determined in order to identify the center of the diffraction at the crystal-to-detector distance, where X-ray data collection would be collected. The crystal was flash-frozen mounted on the goniometer head. The height and the center of the crystal in cryo-loop were adjusted to ensure that the crystal would be centered in the X-ray beam in full degree of goniometer head rotation.

Then the crystal was exposed to X-rays (Cu K_α λ=1.5418 Å) on Rigaku rotating anode generator operating at 50 kV, 100 mA. Its diffraction was collected on an R-Axis IV++ image plate detector mounted on the generator in 0.5°oscillation for 209 frames. After obtaining the complete set of data, the crystal was restored in the preserving solution.

3.3.3 Data Processing

X-ray diffraction data were collected and processed with the program CrystalClear/d*TREK (Rigaku/MSC). Distance between the spots on a photograph was interpreted to give the separation of repeating units and dimensions of the unit cell. Crystal orientation and detector distance were refined to predict the reflection space group. Intensity of each reflection was integrated based on the predicted position and profiles of spot shapes. Redundant data were scaled and averaged to obtain unique data based on the symmetry and space group of the crystal. The unique scattering factors will be used in structure determination.

Number of protein molecules in unit cell (Z) can be estimated by a method proposed by Brian Matthews, 1968 (71). The method based on the ratio of the unit cell volume and the molecular weight of protein crystals, which have been found to be in the range of 1.9 to 4.2 $Å^3$/Da and around 2.4 $Å^3$/Da on average. This number is called Matthews coefficient, or V_M.

Copyright by Mahidol University

$$V_M = \frac{V_{cell}\ (Å^3)}{\frac{\text{No. mol}}{\text{1 asym.}} \times \frac{\text{No. asym.}}{\text{1 unit cell}} \times \text{M.W.}}$$

where: asym. = asymmetric unit, mol = molecules

With the knowledge of V_M, percentage of solvent content can be calculated from the volume fraction of the protein ($V_{protein}$) as follows.

$$V_{solvent} = V_{unit\ cell} - V_{protein}$$

$V_{protein}$ can be calculated from the specific volume (V_{sp}) of a protein molecule which is always approximately 0.74 cm^3/g, as shown below.

$$V_{protein} = \frac{\text{Specific volume of the protein } (cm^3/g)}{V_M\ (Å^3/Da) \times N\ (mol^{-1})}$$

where N = Avogadro's number, V_M= Matthews, coefficient.

Hence,

$$V_{protein} = (0.74/\ 0.602)\ V_M$$

and therefore,

$$V_{solvent} = 1 - (1.23 / V_M)$$

As protein crystals normally contain ~50% solvent, ranges from 20–80%, calculations of both V_M and solvent content are generally used to confirm the estimation of number of molecules per asymmetric unit.

Copyright by Mahidol University

The unique data were scaled to absolute scale based on the number of all atoms present in an asymmetric unit estimated from the V_M. This was done via a plot of $\log_e$(mean intensity/mean f^2) versus the resolution $(\sin\theta/\lambda)^2$, known as the Wilson plot. Calculation of electron density maps using these scaled data would result in distribution of electron in absolute scale, *i.e.* electron per cubic angstrom.

3.4 Structure Determination and Refinement

3.4.1 Difference Fourier Techniques

Difference Fourier techniques is a method of comparing similar structures when both can be obtained in essentially the same crystalline form. It is normally used for comparing the difference between an enzyme in its native state with its structure in complex with a ligand.

The phases can be obtained by back-calculation of the Fourier transform from the refined protein structure coordinates to its 'calculated' diffraction amplitudes, $|\mathbf{F}_{hkl}|_{\mathbf{calc}}$. Such phases can be used together with protein-ligand complex's diffraction amplitudes to calculate electron density maps of the protein-ligand complex. Substraction of the amplitudes of the diffraction pattern of the native crystal's from the amplitude of the complex crystal's would result in differences which can be used as the coefficients in Fourier synthesis to compute a Difference Fourier electron density map.

From the Difference Fourier map, any parts of the protein or individual amino acids that have altered position during binding process will ideally appear as pairs of closely associated negative and positive density areas. The negative density represents the position occupied in the native structure and the positive area represents the position occupied in the complex. Thus, not only how the ligand fits to the surface or active site of the protein, but how the protein alters its local conformation to accommodate and optimize its interaction with the ligand would be shown. The magnitude of difference electron density peaks would be proportional to the electron

Copyright by Mahidol University

density of the ligand, so the ligands can be located in relatively low resolution Difference Fourier maps (72, 73).

In order to obtain two crystals with comparable phases and amplitudes, the crystals have to be isomorphous, with identical unit cell dimensions and symmetry properties. The complex crystal data set must be placed on a common numerical scale with the native crystal data so that relative differences between individual reflections can be formed by subtraction of the two. Since the crystal of *Pf*-DHFR-TS complexed with trimethoprim obtained was found isomorphous to the crystal of *Pf*-DHFR-TS in complex with pyrimethamine which had already been solved (39), this method can be employed by using the latter, with ligands removed, as a template for Difference Fourier map calculation.

3.4.2 Model Building Based on Difference Map

In order to modify the model of protein structure from *Pf*-DHFR-TS – pyrimethamine complex to fit the diffraction data obtained from *Pf*-DHFR-TS – trimethoprim crystal, various electron density maps were used to guide the model building.

In order to obtain electron density map of the new complex, calculated phases, $\alpha'_{calc(h,k,l)}$, may be used in combination with experimental amplitudes $|F_{o(h,k,l)}|$ obtained from the reflections h,k,l to calculate an electron density map called an F_{obs}, or F_o, map. Each amplitude was assigned with a weighing factor to provide a different contribution to the Fourier series. This allows reduction of the bias from the observed reflections whose phases are questionable. The F_{obs}, or F_o, Fourier series is

$$\rho_{(x,y,z)} = \frac{1}{V} \sum_h \sum_k \sum_l w_{(h,k,l)} \left|F_{o(h,k,l)}\right| \cdot e^{[-2\pi i\,(hx+ky+lz-\alpha'_{calc(h,k,l)})]}$$

Copyright by Mahidol University

After rigid body minimization, which moves the molecules in an asymmetric unit to the most superimposable position, the new atomic coordinates were used to calculate a new set of amplitude called F_{calc}, or F_c, as follows.

$$F_{c\,(h,k,l)} = \sum_{i=1}^{atom} f_i \, e^{[2\pi i\,(hx_i+ky_i+lz_i)]} \cdot e^{[-B_i \sin^2\theta/\lambda^2]}$$

where F_c is the calculated structure factor or calculated amplitude for a reflection (h,k,l); f_c is a calculated atomic structure factor and B_i is the temperature factor of each atom. The temperature factor reflects the thermal motion of the atom which is the vibration of atom about its center position and also disorder in which equivalent atoms do not occupy the same position in every unit cell. Atoms with high temperature factor provide less contribution to the structure factor.

To allow improvement of the model without introducing excessive bias from the model phases, an electron density map called $F_o - F_c$ map was used as a difference map to visualize the positive and negative densities. This Fourier series is called an $F_o - F_c$ synthesis.

$$\rho_{(x,y,z)} = \frac{1}{V} \sum_h \sum_k \sum_l \left| |F_{o(h,k,l)}| - |F_{c(h,k,l)}| \right| \cdot e^{[-2\pi i\,(hx+ky+lz-\alpha'_{calc(h,k,l)})]}$$

The $F_o - F_c$ map aims to emphasizes errors and hard to interpret. A more easily interpretable map, which give solely a positive map with partial reduction of the influence by the model is called the $2F_o - F_c$ map. While using the calculated phases, this map strengthens the F_o map and leave out the unsupported features of the calculated map. A mathematical representation below illustrates why $2F_o - F_c$ map could satisfy such purposes.

Copyright by Mahidol University

$$\rho_{(x,y,z)} = \frac{1}{V}\sum_h\sum_k\sum_l \left|(2|F_o| - |F_c|)\right| \cdot e^{[-2\pi i\,(hx+ky+lz-\alpha'_{calc(h,k,l)})]}$$

$$= \frac{1}{V}\sum_h\sum_k\sum_l |F_o| \cdot e^{[-2\pi i(hx+ky+lz-\alpha'_{calc.})]} + \left||F_o| - |F_c|\right| \cdot e^{[-2\pi i(hx+ky+lz-\alpha'_{calc})]}$$

All electron density map calculations were done with the software CNS (74).

3.4.3 Structure Refinement

Various methods in crystallographic refinement seek to find the function **Φ** which give the least sum of the squares of differences between observed and calculated amplitudes.

$$\Phi = \sum_{hkl} w_{hkl}\,(|F_o| - |F_c|)^2_{hkl}$$

In the refinement, the calculated structure factor, F_c, can be expanded to illustrate all parameters used in the refinement as follows:

$$F_{c\,(h,k,l)} = G \cdot \sum_{j=1}^{atom} n_j f_j\, e^{[2\pi i\,(hx_j+ky_j+lz_j)]} \cdot e^{[-B_j\,(\sin\theta/\lambda)^2]}$$

G is an overall scale factor to pull an $|F_c|$ to a convenient numerical scale. The f_j term describes the diffractive contribution of atom j to this structure factor; n_j is the occupancy of atom j; B_j is its temperature factor; x_j, y_j, z_j are its atomic coordinates. The first exponential term is the Fourier description of a simple three-dimensional wave with the frequencies *h, k, l* in the direction *x, y,* and *z.* The second exponent shows that the effect of temperature factor on the structure factor depends on the angle of reflection [sinθ/λ], or resolution.

Copyright by Mahidol University

The overall agreement between the observed structure amplitudes and those calculated from the current model is normally indicated by a parameter called the residual index, or R-factor. As the model and the correct structure converge, the measured structure amplitude $|F_o|$ and the calculated structure amplitud $|F_c|$ should also converge. The R-factor is defined as

$$R = \frac{\sum \left| |F_o| - |F_c| \right|}{\sum |F_o|}$$

A desirable target for R-factor refined with data to 2.5 Å resolution is 0.2. In order to assess the refinement strategy and the quality of atomic model, another parameter called the free R-factor, or R_{free}, is used to together with the R-factor. The mathematical formulation is the same, but R_{free} is computed with a smaller set of data which have been set aside from the beginning, and have never been included in the overall data set used to calculate the phase in the refinement. R_{free} is believed to give a better and less biased measure of the overall model. In general R_{free} values are higher than R-factor, but they will become more similar in final stages of refinement (75).

Iterative rounds of refinement is illustrated in Figure 14. Each refinement cycle was aimed to find a structure with lower R-factor, and $R_{free.}$ Manual model building and refinement was done on a Linux-based graphics station using the program O (76). The amino acid side chains were adjusted to fit positive density, and avoid negative density. If a flexible loop was shifted from the position occurred in the structure of pyrimethamine complex, the backbone of that loop was rebuilt with polyalanine. Side chains were extended from the Cα atoms in the next round of refinement if their densities became clear.

Copyright by Mahidol University

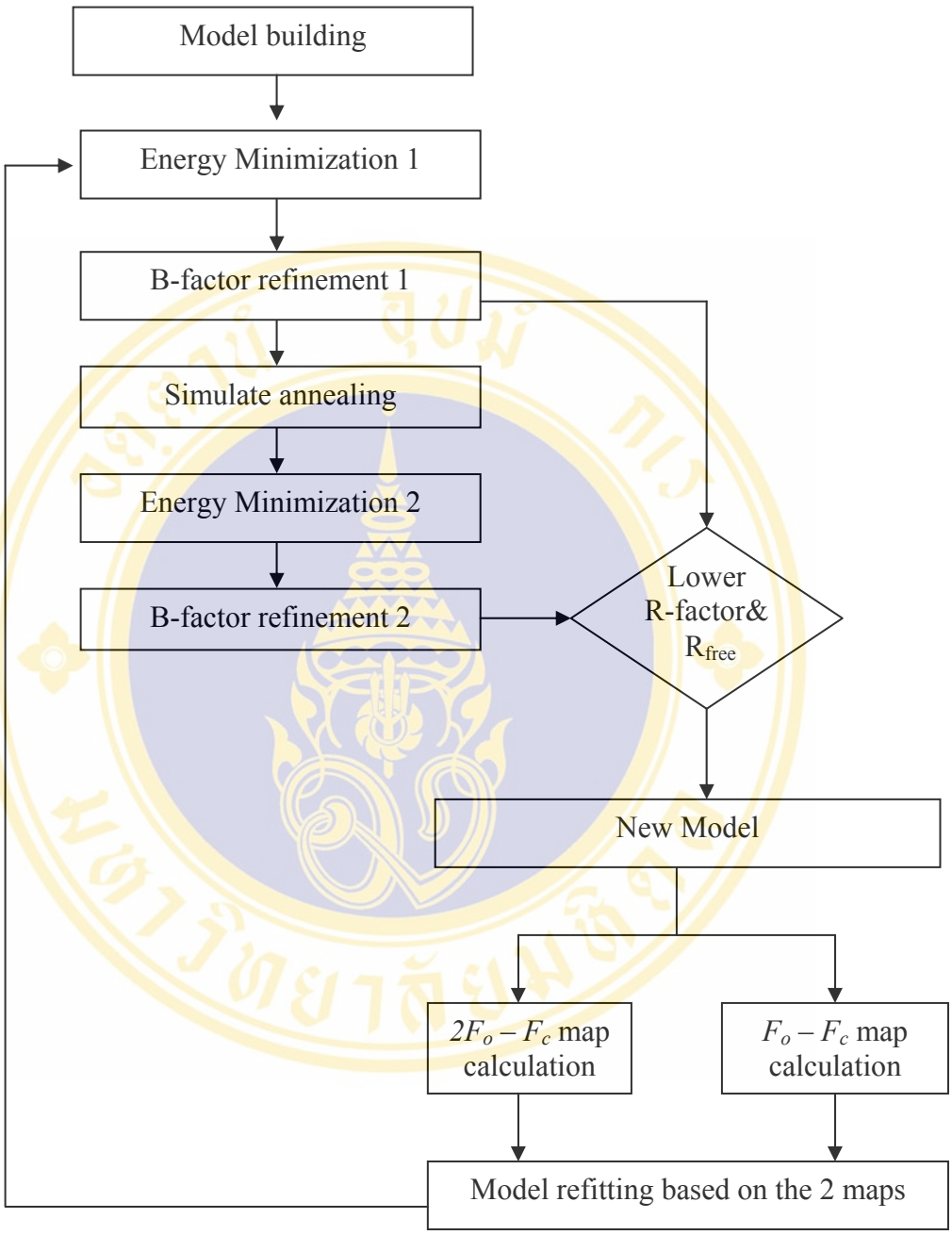

Figure 14 Diagram of typical cycle of refinement used in this project. Each refinement cycle was aimed to find a structure with lower R-factor, and $R_{free.}$ After the model was rebuilt by manually fit atoms into the electron density maps, geometries and B-factors of the model were optimized from both a regular energy minimization and from an energy minimization after simulated annealing. R-factors and R_{free} from the two models were compared and the chosen model was used to calculate two new maps, *i.e.* $F_o - F_c$ and $2F_o - F_c$, for the next round of model building and refinement.

Copyright by Mahidol University

After each round of manual model building, the geometry optimization was performed. The basic idea is that, all atomic connectivities have natural bond length, bond angles, and other geometries. Each deviation from these standard values would result in an increasing of the total energy of the system in relation with a hypothetical ideal geometry. Therefore, the structure with the lower total energy should be a consequence from lower intramolecular strain and the better overall geometry. Nevertheless, minimization algorithms applied to optimized geometry usually find only the local minimum on the potential energy surface closest to the initial coordinates (77).

An additional method called simulated annealing was used to prevent the system in getting stuck in a particular region of the conformational space. This method enhances conformational sampling by applying an elevated temperature to the simulation to allow the molecule to overcome large energy barriers that may exist between some conformations. Then the simulation temperature is gradually decreased to relax some distorted geometry that cannot be relaxed by regular optimization procedure (78).

The software CNS (Brunger *et al.*, 1998) was the main tool for energy minimization, simulate annealing, B-factor refinement, as well as structure factors and map calculations. Moleman and Mapman (79) was the programs used to facilitate in file conversion and data processing between these softwares.

3.4.4 Addition of water molecules

Oxygen atoms which represent water molecules were manually added to the positive density upon manual inspection. The electron density that was filled with water should have at least one hydrogen bond partner with an approximate intermolecular distance of 2.7-3.0 Å. Protein loops with high B-factor were deleted from the model. Effects of molecule insertion and deletion were observed closely by following the progression of R-factor and R_{free}.

Copyright by Mahidol University

3.4.5 Composite omit map

Late in the refinement, a composite omit map is also calculated for a more thorough elimination of model bias. Recalling the basic principle of X-ray diffraction, every part of electron density was contributed from all reflections from the diffraction pattern. Excluding a partial volume from the model during map calculation, could still give rise to the electron density map of the whole volume, but with less resolution.

A composite omit map was built from several boxes of electron density maps calculated separately. For the calculation of each box, all atoms present in that particular box (must be ≤ 5% of all atoms in the model) were deleted and the remaining model was used in electron density calculation. Since the electron density was of those atoms omitted in the map calculation, the map is essentially an 'omit map'. To remove the model bais in the map, the remaining model was subjected to a simulated annealing run before the calculation of electron density. Therefore, the density of each box was calculated independently of contribution of the scattering atoms in that box, and thus the composite omit map was considered free from model bias. Electron density in the map was a true representation of the content in the crystal.

For this research, the total map volume was divided into 440 boxes. While calculating an omit map, each 0.26% of volume of the whole map was defined to be excluded out of the protein model and only the rest 99.74% was used to calculate the map. Electron densities appeared in such 0.26% were used in combination with the other 439 portion of 0.26% maps to build the overall volume of the whole map. This map composition is called a composite omit map.

Though seem less accurate because of the smaller data set, the phase angles obtained from the remaining 99.74% of the models, were believed to have the smallest bias from the protein model in the 5% region. If the atoms actually present in such volume, the phases obtained from other parts of the model should contribute to make electron density in such region become visible without having any model built therein.

Copyright by Mahidol University

3.5 Structural Analysis

Interactions within and around *Pf*-DHFR-TS active sites was closely determined with the molecular graphics program O (76). Comparison with the pyrimethamine complex structure was made through superposition of the DHFR domain in terms of enzyme-ligand interactions in order to investigate the likeness and the difference between the two complexes.

Copyright by Mahidol University

CHAPTER 4
RESULTS

4.1 Protein Purification

A. Purification by MTX-Affinity and Gel Filtration Chromatography

In order to achieve the higher binding efficiency, the crude protein extract was divided into two portions for purification in two MTX-affinity columns (A and B). DHFR activity in the flow-through after sample circulation was subtracted from those measured before loading to the column to indicate percentage of protein bounded to the column as shown in the table below.

Table 7 Amount of DHFR obtained per 12 litres of cell culture and the protein binding percentage in MTX-column from DHFR activity assay

DHFR assay		$\Delta OD_{340}/\Delta t$ (min^{-1})	Assayed vol. (ml)	DHFR activity (µmol/min/ml)	Total vol. (ml)	Total DHFR activity (U)	% bound enzyme
Crude	A	-0.079	0.005	1.28	~200	257	-
	B	-0.073	0.005	1.19	~200	237	-
	A+B	-	-	-	400	494	-
Flow through	A	-0.020	0.005	0.33	~200	65	75
	B	-0.008	0.005	0.13	~200	26	89
	A+B	-	-	-	400	91	82

$$\text{MTX-Bound} = \frac{\text{Crude (A+B)} - \text{Flow through (A+B)}}{\text{Crude (A+B)}} \times 100\%$$

$$= \frac{403\ \text{U}}{494\ \text{U}} \times 100\% = 81\%$$

Copyright by Mahidol University

Table 8 Amount of DHFR obtained per 12 litres of cell culture after DHF elution

DHFR assay	$\Delta OD_{340}/\Delta t$ (min^{-1})	Assayed vol. (ml)	DHFR activity (µmol/min/ml)	Total vol. (ml)	Total DHFR activity (U)	Pooled DHFR (U)
F1	-0.485	0.005	7.89	9.0	71	
F2	-0.296	0.005	4.82	9.2	44	**125**
F3	-0.244	0.005	3.97	2.5	10	
F4	-0.228	0.005	3.71	2.5	9	
F5	-0.252	0.005	4.10	4.5	18	48
F6	-0.162	0.005	2.64	5.0	13	
F7	-0.157	0.005	2.55	3.2	8	
DHFR obtained after DHF elution					173	

The first three fractions (F1-F3) were pooled for further purification using gel filtration chromatography. The elution profiles was obtained as shown in Figure 15.

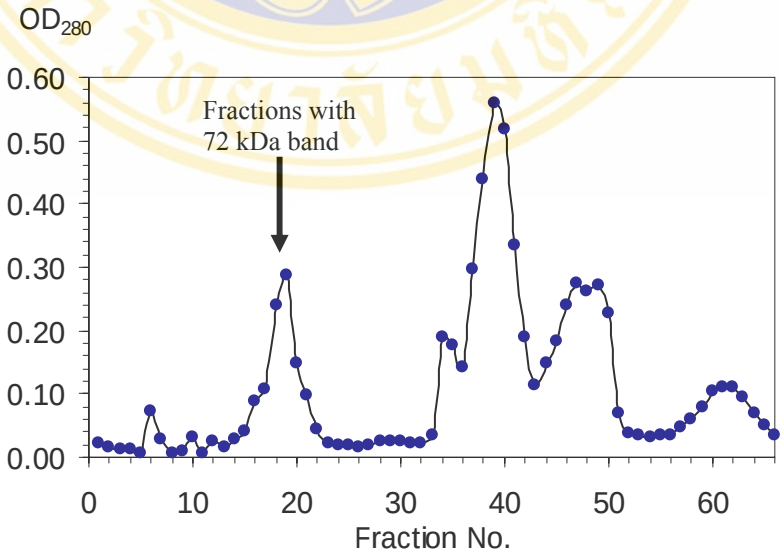

Figure 15 Elution profile of protein fractions obtained from gel-filtration column. *Pf*-DHFR-TS was eluted between fractions 16-22, as confirmed by 10% SDS-PAGE analysis.

Copyright by Mahidol University

All fractions with absorbance at 280 nm were determined for size and purity of proteins with 10% SDS-PAGE. SDS-PAGE gel of the most probable fractions to contain *Pf*-DHFR-TS is shown in Figure 16.

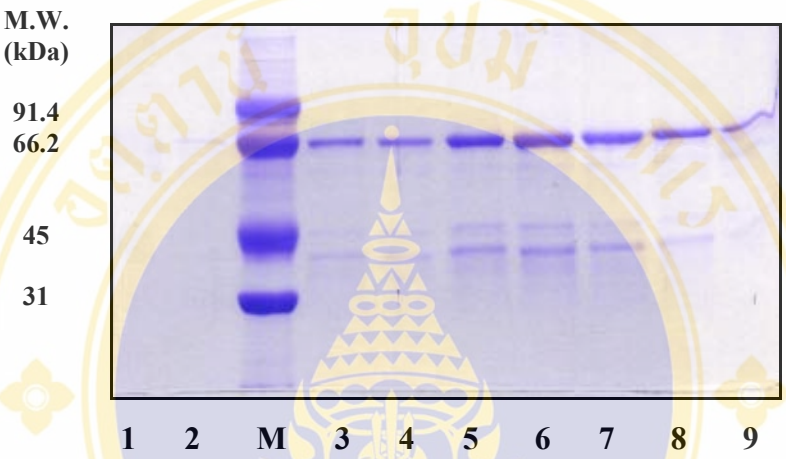

Figure 16 SDS-PAGE (10%) shows purity and size of the purified protein fractions obtained from gel filtration chromatography technique. These fractions were the only ones with protein bands comparable to *Pf*-DHFR-TS with the size of 72 kDa. The minor bands was previously reported to be the truncated *Pf*-DHFR-TS fragments (52).

Lane 1, 2 *Pf*-DHFR-TS eluted from gel filtration column, lane 1 was the 13th fraction and lane 2 was the 15th fraction
Lane M. Standard protein markers
Lane 3, 4, 5, 6, 7, 8, 9 *Pf*-DHFR-TS eluted from gel filtration at the fractions number 16, 17, 18, 19, 20, 21, 22 respectively.

To estimate the size of the protein, a standard curve for a particular gel can be obtained by plotting the distances that protein markers travel versus the logarithm of their molecular weights.

Copyright by Mahidol University

Table 9 Mobility of protein standards for molecular weight estimation

M.W. of the protein marker	Mobility (cm)	log M.W.
94	1.25	1.97
67	1.80	1.83
43	3.00	1.63
30	3.80	1.48

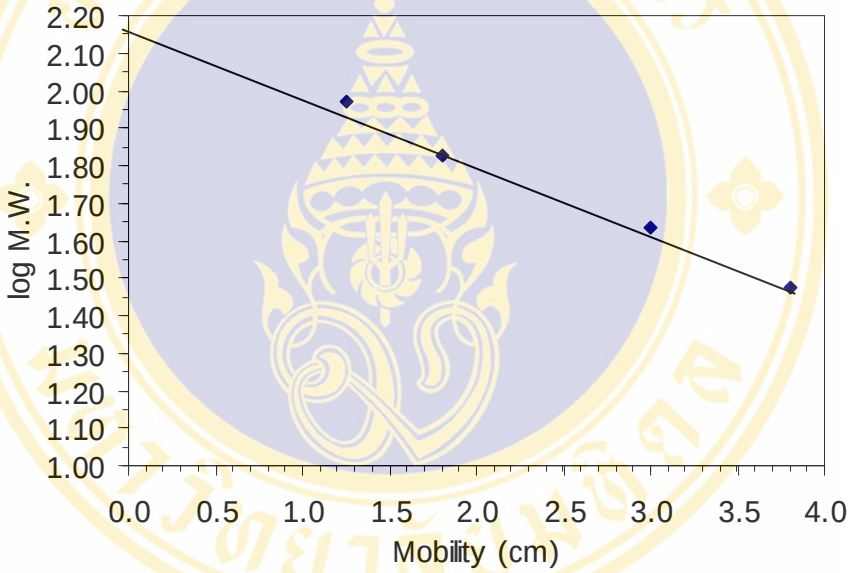

Figure 17 Standard curve for SDS-PAGE molecular weight estimation

By extrapolating the distance that the protein travels to meet the linear curve and converting the value on y-axis back to molecular weight, the size of the protein can be obtained. This can be done by a mathematical formulation described below

From the standard curve

slope = (y-y') / (x-x')

= (1.48-1.83) / (3.80-1.80)

= -0.17,

and

y-intercept = 2.15.

Copyright by Mahidol University

Therefore,

$$y = (-0.17)\,x + 2.15$$

From the formulation above, the size of the protein obtained can be calculated as shown in Table 10.

Table 10. Molecular weight estimation of the protein in the fraction 16th eluted from gel filtration column using 10% SDS-PAGE

Protein band	Mobility (cm)	log M.W.	Estimated M.W. (kDa)	Referent *Pf*-DHFR-TS M.W. (kDa)
Major band	1.65	1.86	~73	72
Minor band 1	2.85	1.65	~45	42
Minor band 2	3.15	1.60	~40	35 (12.5% gel)

Fractions 16-22 should contain the protein *Pf*-DHFR-TS because they contain a major band of 72 kDa corresponding to the estimated size of *Pf*-DHFR-TS, and also exhibit DHFR activity. The other two bands were likely to be truncated *Pf*-DHFR-TS as described by Chitnumsub, *et al.* 2004 (52). Even though, the estimated sizes of minor bands are not accurate due to the difference in percentage of the gel used; they were only ones that contain protein bands with similar sizes and number of bands. Thus, these fractions were pooled for further protein concentration.

In general, a protein crystallization experiment needs to have a starting concentration of approximately 10 mg/ml, or higher. Therefore, the purified *Pf*-DHFR-TS was concentrated several times to satisfy such generalization. *Pf*-DHFR-TS obtained from this batch tended to produce high amount of protein aggregation and such protein precipitate seemed to induce more precipitation very quickly. Therefore, the protein was centrifuged to remove protein precipitate several times, which resulted

Copyright by Mahidol University

in tremendous lost of protein yield. Finally, the purified *Pf*-DHFR-TS protein was concentrated until the volume was decreased to 100 μl. The protein sample was aliquoted into three batches and stored separately. According to Materials and Method described in section 3.1.4C, final concentration of the protein was found to be approximately 13.5 mg/ml, estimated for the measured $OD_{280\ nm}$ of 0.0155.

B. Purification by MTX-Affinity and Ion Exchange Chromatography

This batch of protein was prepared in a larger scale, 24 litres, to obtain larger amount of protein for crystallization. The aim was not successful as expected because of bad draining after cell disruption. The cell debris in the protein was clotted in the MTX-column and the protein came out from the lid of the column during affinity column circulation over the weekend. Therefore, the final yield after DHFR elution was less than a half of the amount obtained from MTX-column.

Table 11 Amount of DHFR obtained per 24 litres of cell culture and the protein binding percentage in MTX-column from DHFR activity assay

DHFR assay		$\Delta OD_{340}/\Delta t$ (min^{-1})	Assayed vol. (ml)	DHFR activity (μmol/min/ml)	Total vol. (ml)	Total DHFR activity (U)	% bound DHFR
Crude	A	-0.212	0.010	1.72	~225	387	-
	B	-0.285	0.010	2.32	~225	521	-
	A+B	-	-	-	**450**	**908**	-
Flow through	A	-0.051	0.010	0.42	~225	83	78
	B	-0.008	0.010	0.06	~225	13	98
	A+B	-	-	-	**400**	**96**	**89**

$$\textbf{MTX-Bound} = \frac{\text{Crude (A+B)} - \text{Flow through (A+B)}}{\text{Crude (A+B)}} \times 100\%$$

$$= \frac{812\ U}{908\ U} \times 100\% = 89\ \%$$

Copyright by Mahidol University

Table 12 Amount of DHFR per 24 litres of cell culture after DHF elution

DHFR assay	$\Delta OD_{340}/\Delta t$ (min^{-1})	Assayed vol. (ml)	DHFR activity (µmol/min/ml)	Total vol. (ml)	Total DHFR Activity (U)	Pooled DHFR (U)
F1+2	-0.568	0.005	9.24	26.0	240	**296**
F3	-0.504	0.005	8.20	6.8	56	
F4	-0.293	0.005	4.76	7.0	33	94
F5	-0.256	0.005	4.16	6.7	28	
F6	-0.171	0.005	2.78	10.5	29	
F7	-0.039	0.005	0.63	6.5	4	
DHFR obtained after DHF elution					390	

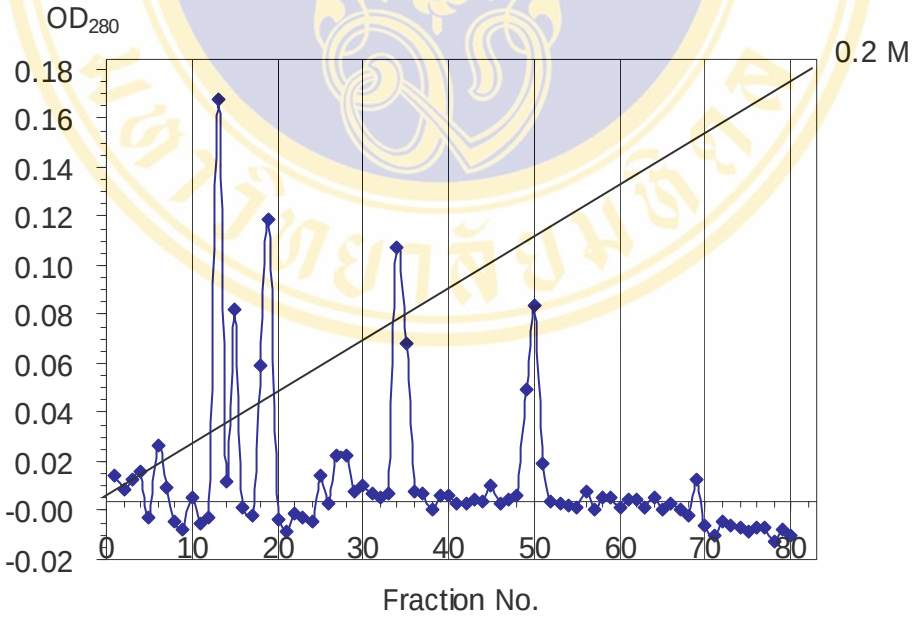

Figure 18. Elution profile of protein fractions eluted from Q-Sepharose column. *Pf*-DHFR-TS was eluted between fractions 24-33, as confirmed by 12.5%SDS-PAGE analysis.

Copyright by Mahidol University

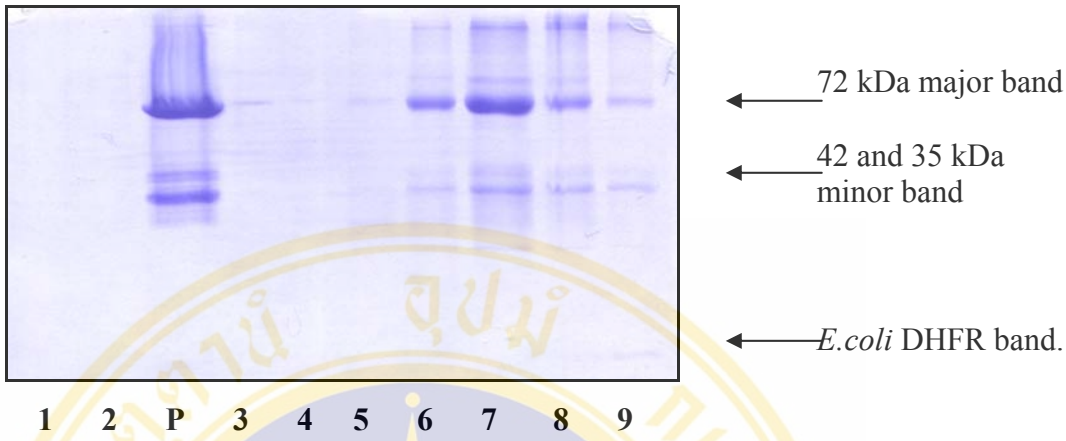

Figure 19 SDS-PAGE (12.5%) shows purity and size of the purified *Pf*-DHFR-TS fraction obtained from anion exchange chromatography technique.

Lane 1, 2 fractions number 19 and 21 eluted from Q-Sepharose column
Lane P. *Pf*-DHFR-TS positive protein marker obtained from Dr. Chitnumsub.
Lane 3, 4, 5, 6, 7, 8, 9 *Pf*-DHFR-TS elusion at fractions number 23, 25, 27, 29, 31, 33, 35, respectively. According to the SDS-PAGE gel, fractions 24-33 were pooled for subsequent crystallization experiment. *E. coli* DHFR band was present in fraction 35, hence it was excluded from the purified pool.

Final concentration of protein, estimated by measuring absorbance at 280 nm of 0.0178 as previously described in section 3.1.4C, was about 15.5 mg/ml. The concentration of protein from this batch was found to be higher than the one obtained from gel filtration technique.

The protein fractions 24 to 33 were pooled for subsequent crystallization experiment. Side fractions were discarded either because it was too diluted or because of contamination from other proteins which affected *Pf*-DHFR-TS purity.

Copyright by Mahidol University

4.2 Protein Crystallization

From the first batch of crystallization trial, 0–0.4 M CH_3COONH_4 and 20–28% (w/v) PEG 4000 in sodium acetate buffer (pH 4.6) at 20ºC, needle-shaped microcrystals were obtained from various conditions around the well with highest ammonium acetate concentration and lowest percentage of PEG 4000 (*i.e.* 0.4 M ammonium acetate, 20% PEG 4000) within three days after crystallization setup. Nothing was found in the row containing negative control experiment which did not contain protein.

Figure 20 Microcrystals found from the first batch of crystallization trial. The largest microcrystals in the tray were obtained from the condition that contained the lowest concentration of PEG 4000 (20%) and the highest ammonium salt concentration (0.4 M).

The sizes of crystals followed the same trend; the higher the amount of ammonium salt, the bigger the crystal size. From the first batch of crystallization, the amount of crystals seemed to be much less when the salt concentration was slightly increased. Therefore, increasing salt concentration might have an effect on crystal size preventing crystal nucleation. Much nucleation was not good because crystals would compete with one another to grow and the protein concentration would not be enough for them to obtain a sufficiently large size.

Copyright by Mahidol University

In every well that contained the same salt concentration, the least amount of PEG 4000 (*i.e.* 20%) produced the smallest amount of precipitation. Hence, the trend for crystallization setup in the second batch was towards the higher concentration of salt, and the smaller percentage of PEG 4000.

However, a prediction of how far to step further might help to reduce the crystallization trial. From the observation of the first batch, trend of crystal size and precipitation seems to occur in a diagonal fashion as illustrated in Figure 21. Since there was a minute amount of protein left from the first tray experiment, it might give some clue to the next crystallization trial.

To trace the direction that might give rise to better crystals in a new tray of crystallization trial, about 3 µl of protein left from the first tray was setup for two new conditions shown as double-line boxes in Figure 21. Precipitant Z [0.6 M CH_3COONH_4 and 18% PEG 4000], and precipitant Y [0.8 M CH_3COONH_4 and 16% PEG 4000], were used for crystallization trial. A positive control precipitant, the one that gave rise to the best crystals from the first tray [0.4M CH_3COONH_4 and 20% PEG 4000], was also set up to observe the reproducibility of the 3 day-leftover protein-trimethoprim mixture.

The well with precipitant Z gave bigger crystals but it was not conclusive whether or not it was better than precipitant Y, which showed a clear solution, as the amount of protein used to crystallize in precipitant Y was run out, hence the concentration of protein would be slightly less than the other 2 wells. Results from the first batch of crystal trial and the search diagram for a new condition were also shown in Figure 21.

Copyright by Mahidol University

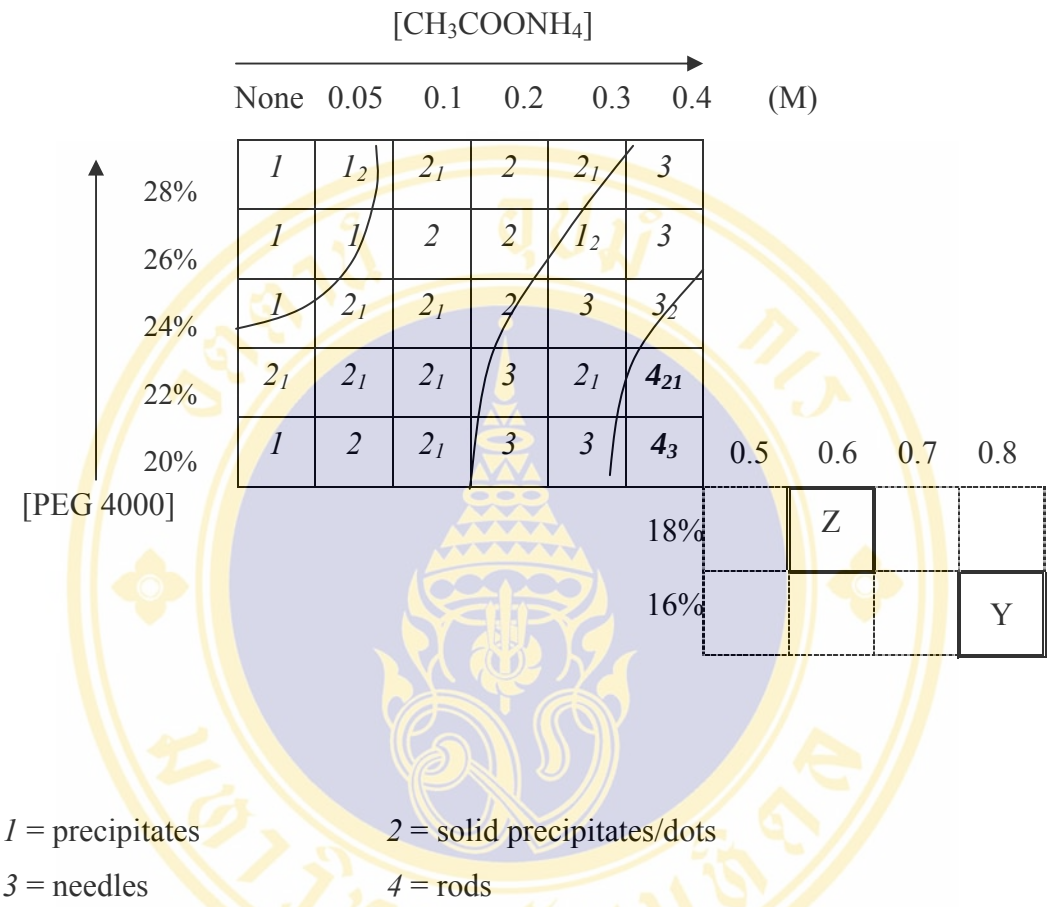

Figure 21 Results of crystal morphology obtained from the first batch of crystallization trial. Numbers in upper left table represent results from the first crystal screening. The results show trends to obtain better crystal towards lower right-hand side with combination towards the decreasing PEG and the increasing salt concentration. From this information, two additional drops were set with an aim to extend the results to the lower right hand side. Numbers with normal fonts represent the major component found in the well, and subscripted numbers represent minor components**.** Double-line boxes were the precipitant conditions used for tracing the promising direction.

Copyright by Mahidol University

The second tray of crystallization was set up to optimize the condition of precipitant Z. Crystals from many conditions formed orthorhombic rods within three days. The photographs of crystals from each condition are shown in Figure 22.

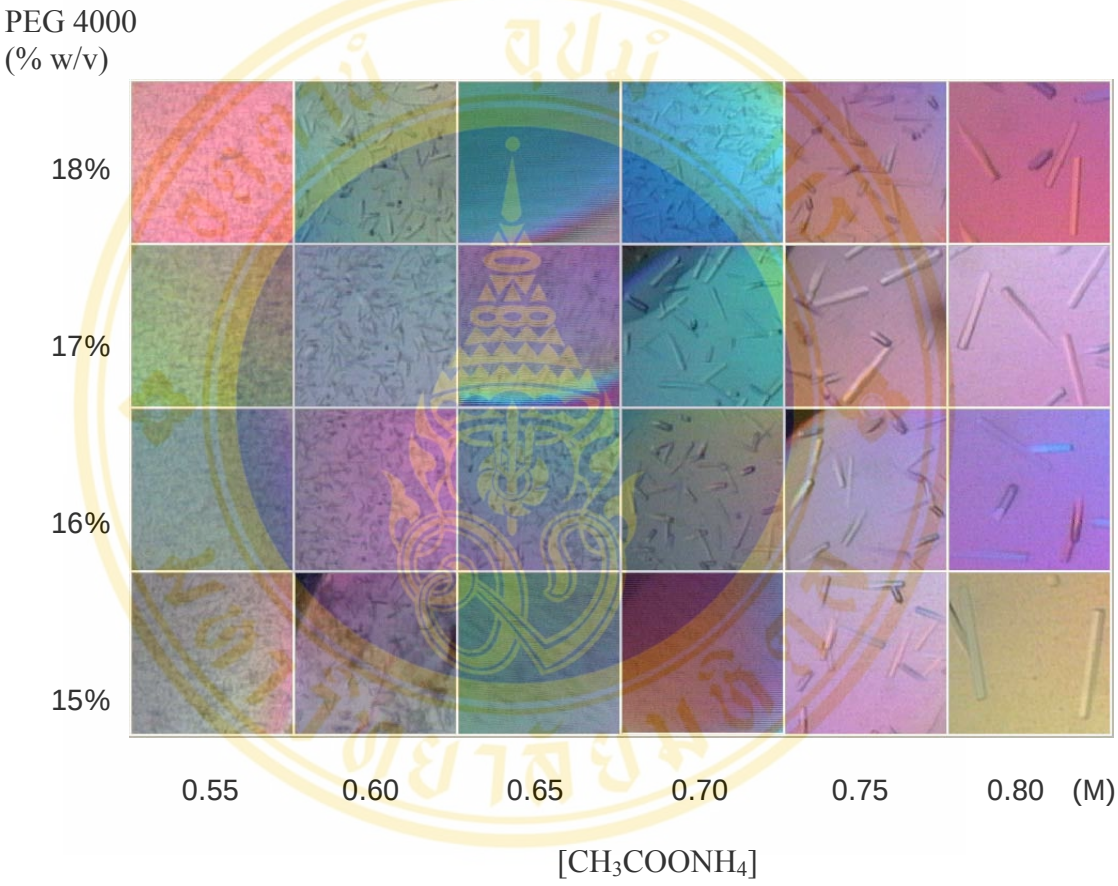

Figure 22 Crystals obtained from the second batch of crystallization by varying concentration of ammonium acetate (0.55–0.8 M) and PEG 4000 (15–18%)

Copyright by Mahidol University

In the third tray, crystallization condition was optimized further towards higher salt concentration. The result was as shown in Figure 23.

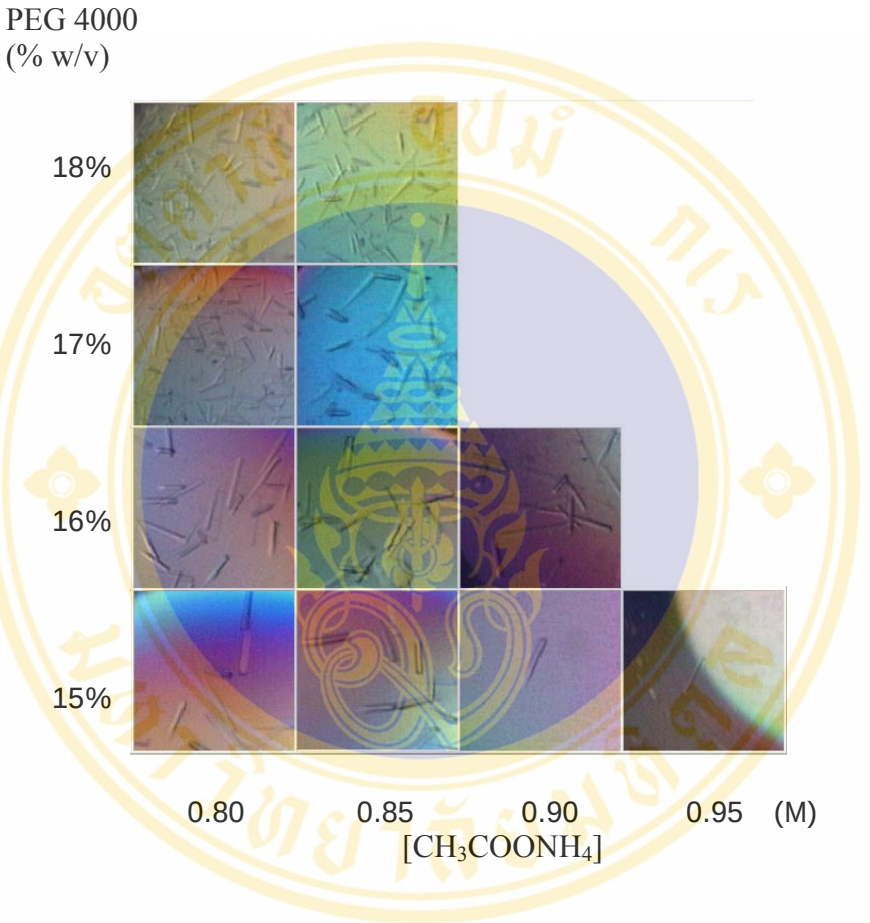

Figure 23 Crystals obtained from the third batch of crystallization by varying concentrations of ammonium acetate (0.80–0.95 M) and PEG 4000 (15–18%)

The rod-shape crystals with a typical size of 120 x 30 x 30 μm^3 were harvested at the 9^{th} day after crystallization setup. The harvested crystals were stored in preserving solution [1.2 M CH_3COONH_4 and 30% PEG 4000 in 0.1 M sodium acetate buffer pH 4.6] at 22°C for at least 30 hours before X-ray diffraction experiment.

Copyright by Mahidol University

In addition, cocrystallization of the double mutant (C59R+S108N) *Pf*-DHFR-TS and an analog of trimethoprim with chemical structure shown in Figure 24, trimethoprim-39 (49), was also accomplished within 6 well–diagonal screening. Crystals with similar morphology to ones with trimethoprim complex were obtained from the precipitant containing 0.9 M CH_3COONH_4 and 16% PEG 4000 in 0.1 M sodium acetate buffer at pH 4.6, as shown in Figure 25. However, the crystals were too small for data collection.

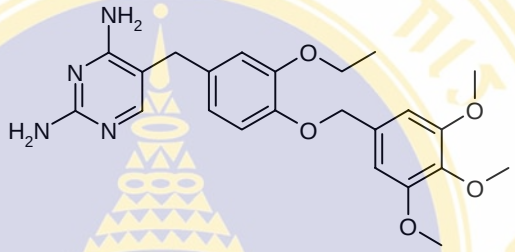

Figure 24 Chemical structure of trimethoprim-39 (49)

PEG4000:	24%	20%	18%	17%	16%	15%
CH_3COONH_4:	0.2 M	0.4 M	0.6 M	0.8 M	0.9 M	1 M

Figure 25 Crystals obtained from cocrystallization of the double mutant (C59R+S108N) *Pf*-DHFR-TS and an analog of trimethoprim, trimethoprim-39.

Copyright by Mahidol University

4.3 Data Collection

Suitable cryoprotectant solution was obtained by trial and error with many crystals. Successful cryoprotectant solution contained 15% glycerol, 28.5% PEG 4000, 0.8 M CH_3COONH_4, and 0.1 M sodium acetate buffer at pH 4.6. After a short soaking in cryoprotectant and flash-frozen, the crystal showed good diffraction up to 2.6 Å resolution with low mosaicity and no ice ring formation. X-ray diffraction data was collected on Rigaku/MSC rotating anode generator equipped with an R-Axis IV^{++} image-plate area detector operating at 50 kV and 100 mA. The crystal-to-detector distance was 260 cm. The results of cryoprotectant trials were summarized in Table 13.

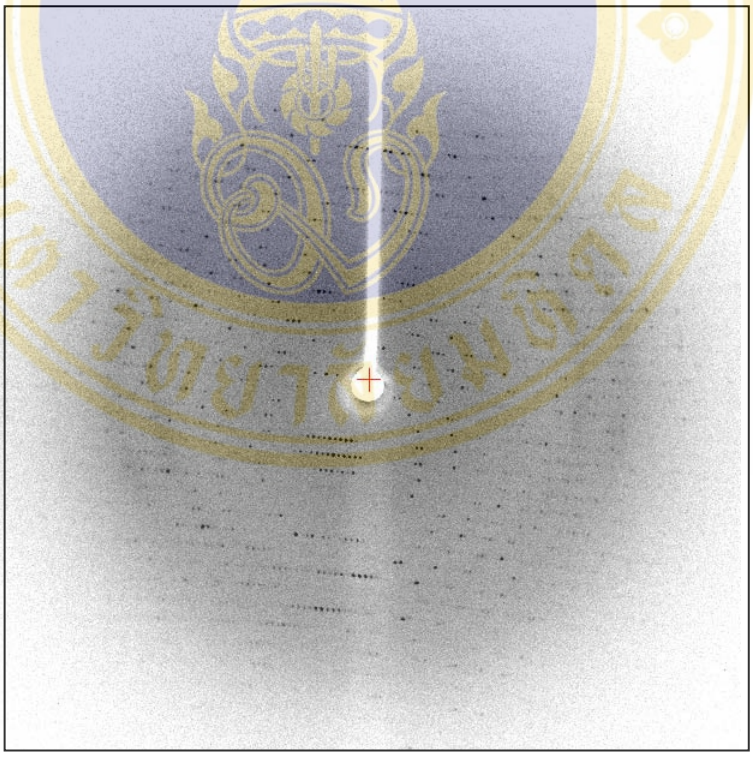

Figure 26 Diffraction pattern. This pattern can be interpreted to the space group and the unit cell dimensions.

Copyright by Mahidol University

Table 13 Cryoprotectant trial used in the crystal freezing

Cryoprotectant	Crystal code; shape (size, mm^3)	Incubation time	Results
30% PEG 4000 **1.2 M CH_3COONH_4** **0.1 M CH_3COONa**	2-2E, rod (0.1 × 0.03 × 0.03)	-	Ice ring formation
30% PEG 4000 **1.2 M CH_3COONH_4** **0.1 M CH_3COONa**	2-2F, rod (0.1 × 0.03 × 0.03)	-	Not diffract
30% PEG 4000 **1.2 M CH_3COONH_4** **0.1 M CH_3COONa** **100 mM DTT**	3-4A, rod (0.10 × 0.03 × 0.03)	-	10 Å
30% PEG 4000 **1.2 M CH_3COONH_4** **0.1 M CH_3COONa** **100 mM DTT**	3-4A, rod (0.10 × 0.03 × 0.03)	8 hrs	4.3 Å *; recollected at 4.0 Å
5% glycerol **30% PEG 4000** **1 M CH_3COONH_4** **0.1 M CH_3COONa** **A few drops of 1 M DTT**	1C_1, rod (0.32 × 0.05 × 0.04)	2 hrs	dissolved
5% glycerol **30% PEG 4000** **1 M CH_3COONH_4** **0.1 M CH_3COONa**	1C_2, rod (0.32 × 0.05 × 0.04)	7 hrs	3 Å
15% glycerol **28.5% PEG** **0.8 M CH_3COONH_4** **0.08 M CH_3COONa**	B3, rod (0.33 × 0.05 × 0.05)	No incubation	2.6 Å

* crystal slipped out of the loop center

Copyright by Mahidol University

Table 14 X-ray data collection statistics. Values in parentheses are statistics for the last resolution shell.

Compound	*Pf*-DHFR-TS, dUMP, NADPH, trimethoprim
Resolution range	51.54–2.60 Å (2.69–2.6 Å)
Space group	$P2_12_12_1$ (Orthorhombic)
Unit-cell parameters	$\alpha = 90^o$, $\beta = 90^o$, $\gamma = 90^o$ a = 56.3 Å, b = 153.7 Å, c = 164.1 Å
Mosaicity	0.49
No. of molecules per asymmetric unit	2
V_M	2.5 $Å^3$/Da
Solvent content	49.8%
No. of reflections	observed = 182,523 unique = 43,724
Completeness	97.0 % (79.5%)
I / sigma I	6.2 (1.6)
Average redundancy	4.17
R_{merge}	8.3 % (31.4%)

Copyright by Mahidol University

Unit cell dimensions derived from collected diffraction pattern were a = 56.3 Å, b = 153.7 Å, c = 164.1 Å, α = 90º, β = 90º, and γ = 90º. The crystal belonged to the orthorhombic space group $P2_12_12_1$.

The Matthew's coefficient, or V_m, was calculated as previously described in the section 3.3.3, by using a unit cell volume of 1.42×10^6 Å^3. The molecular weight of the protein *Pf*-DHFR-TS is known to be 72 kDa, and the space group $P2_12_12_1$ contains four asymmetric units per unit cell. Therefore, V_m could be 4.9, 2.5, or 1.6 Å^3/Da for Z of 1, 2, or 3, respectively. Based on the average value of V_M determined by Matthews, the *Pf*-DHFR-TS crystal most likely contained 2 molecules per an asymmetric unit, resulting in the V_M and the solvent content of 2.5 Å^3/Da and 49.8%, respectively.

Among 182,523 diffraction measurements, 43,724 reflections were unique and resulted in a 97.0 % complete data set. The last shell of resolution range (2.69–2.60 Å) contains 79.5% with R_{merge} of 31.4%, which give rise to the cumulated R-merge of 8.3%. Data in this range of resolution was the optimum range retain the data completeness at high resolution, without producing too high fluctuation among data from all diffraction patterns.

4.4 Structure Determination and Refinement

The structure solved based on difference Fourier technique as the crystal obtained from this experiment, *Pf*-DHFR-TS (K1CB1) in complex with trimethoprim, was found to be isomorphous to the well-refined *Pf*-DHFR-TS (K1CB1) in complex with pyrimethamine. The diffraction intensities from trimethoprim *Pf*-DHFR-TS complex were scaled to the absolute data using the CCP4 programs (80).

Difference Fourier maps were calculated using phases derived from the *Pf*-DHFR-TS (K1CB1) – pyrimethamine, without pyrimethamine excluded. Positive electron density was found in the active site region occupied by pyrimethamine in the pyrimethamine complex structure. Hence, it implies the presence of trimethoprim in the active site. Positions of trimethoprim and cofactors, as well as the conformation of

Copyright by Mahidol University

proteins after manual model fitting was decreased to an acceptable value, as indicated by R_{free} and R-factor. The detailed explanation about R-factor was described in Material and Methods 3.4.3, and the refinement progress was shown in Figure 27.

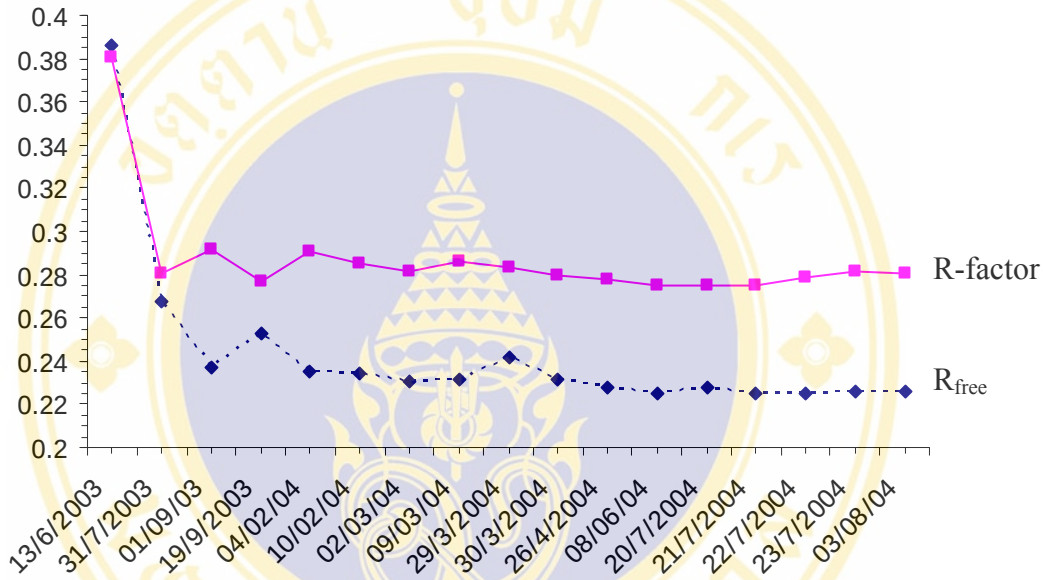

Figure 27 Progression of R-factor and R_{free} along the iterative cycles of model refinement. The decrease in both R-factor and R_{free} reflects the refinement improvement.

Except for the refinement done on September 19th,2003 and March 29th, 2004, R-factor and R_{free} were decreased gradually after each round of model refinement which showed that model building was done ion the proper direction.

Refinement on September 19th,2003 gave rise to a significant decrease of R_{free} and an increase in R-factor because the two large loops found coincided with negative density in the F_o-F_c map were removed. The increase in R-factor was the effect of loops truncation. The absence of several atoms in the model within the loop regions resulted in lesser amount of scattering electrons than those of the real molecules.

Copyright by Mahidol University

R-factor was calculated from almost the whole data set, while R_{free} was only calculated from a small number of reflections in the test set, hence the R-factor elevation was not unusual when large parts of the model were excluded. R_{free} reduction was a good sign as the model seemed to be closer to that of reality because, randomly, it did not contain too many parts in the wrong regions.

A lot of water molecules put into the refinement of March 9th, 2004 resulted in higher R-facter and R_{free}, which suggested the model building in this refinement was not correct. Therefore, most of the water molecules added in that refinement were removed for subsequent March 29th, 2004 refinement which resulted in the increase in R-factor and a slight decrease in R_{free}. Further minimization without model refinement on March 30th, 2004 give a comparable R-factor to March 9th, 2004 and a better value of R_{free}, which could be inferred that some of the water molecules kept from March 29th, 2004 resulted in better R_{free}.

Further model refinements were continued until July 21st, 2004, which resulted in only minor R-factor improvement. The final three rounds of model building for refinement were done mostly by adding atoms to the poorly defined map regions resulting in refined atoms with high B-factors which did not give rise to a better model. However, R-factor and R_{free} did not reach the optimal level yet, partly because the geometry optimization constrained the backbone too much that some parts of the refined model could not fit into the electron density. This will have to be improved further with the changes in the geometry restraining parameters.

The best refinement statistics were those obtained from the refinement done on July 20th, 2004. The results were shown in Table 15.

Copyright by Mahidol University

Table 15 Structure refinement statistics obtained from the best refinement cycle.

Resolution range (Å)	30–2.60 Å
Reflections used in refinement	
Total	43,381 (96.9 %)
Working set	41,192 (92.0 %)
Test set	2,189 (4.9%)
No. of non-hydrogen atoms	
Total	9,058
Protein	8,684
Ligand	178
Water	196
R-factor (%)	0.225
Free R-factor (%)	0.275
R.m.s. deviations from ideal values	
Bond lengths (Å)	0.009
Bond angles (°)	1.429
Dihedral angles (°)	22.677
Improper angles (°)	1.308
B-factors (Å^2)	
Range	29.078–95.408
Mean	56.934

According to the Ramachandran plots in Figure 28, the overall structure is within the expected range for a well refined structure as reported from the program WHAT IF (81).

Copyright by Mahidol University

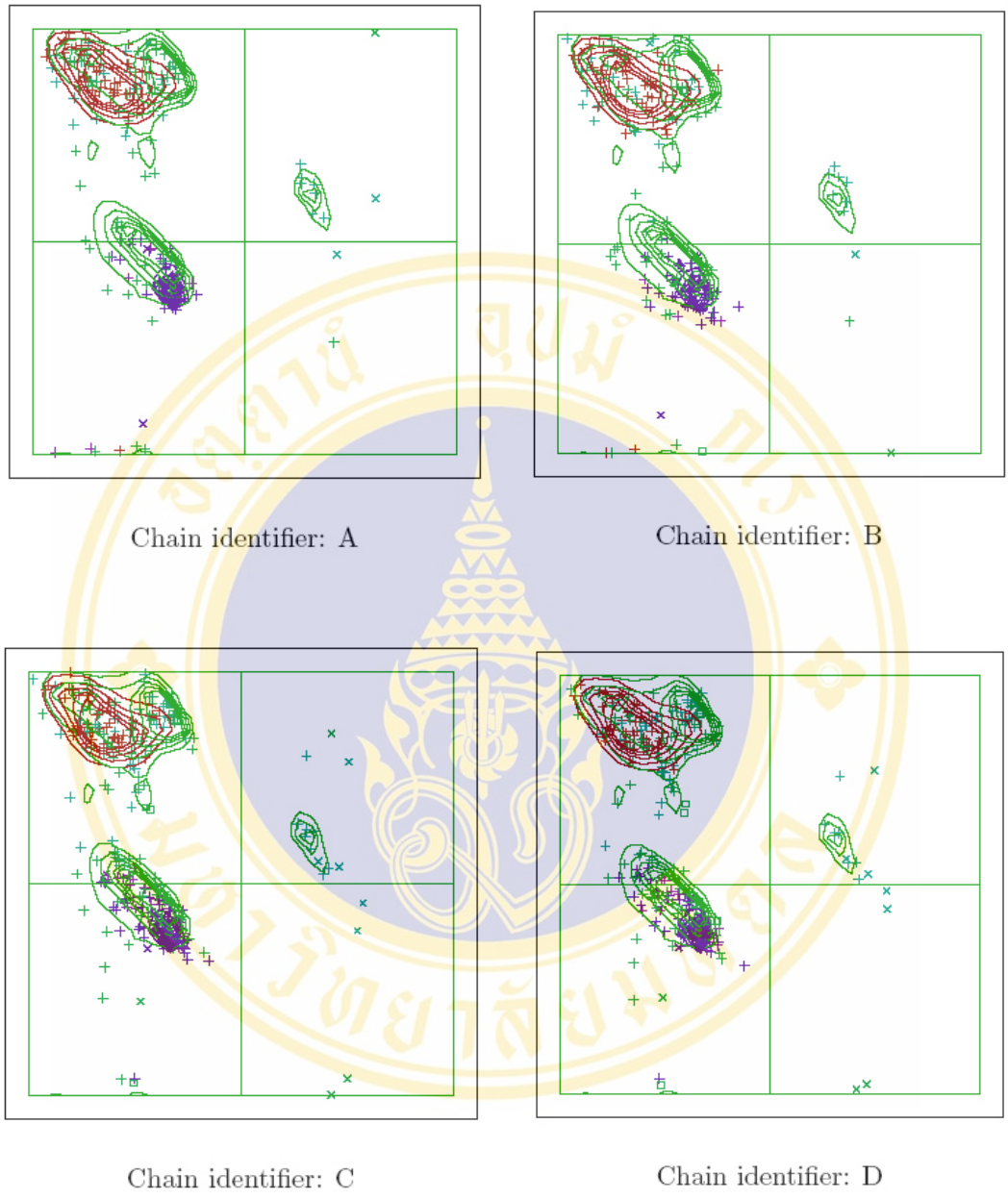

Figure 28 Ramachandran Plots of all of the ϕ/ψ angle pairs for the refined *Pf*-DHFR-TS. Panels with chain identifier A and B designate the two DHFR chains, and chain identifier C and D designate the two TS chains. Within each panel, x-signs represent glycines, squares-signs represent proline, the plus-signs represent all other residues. The contour areas in each panel are allowed regions for strand residues (far left), helix residues (bottom left), and for all other residues. There are only a few unacceptable plus-sign falls outside the contour regions, which can be improved without difficulty in further round of refinement.

Copyright by Mahidol University

CHAPTER 5
DISCUSSION

5.1 Architecture of the Protein

The overall structure of *Pf*-DHFR-TS is the same as reported in Yuvaniyama, 2003 (39). The protein comprises 4 domains as shown in Figure 29. This research focuses on structural information of the *Pf*-DHFR domains which harbor trimethoprim.

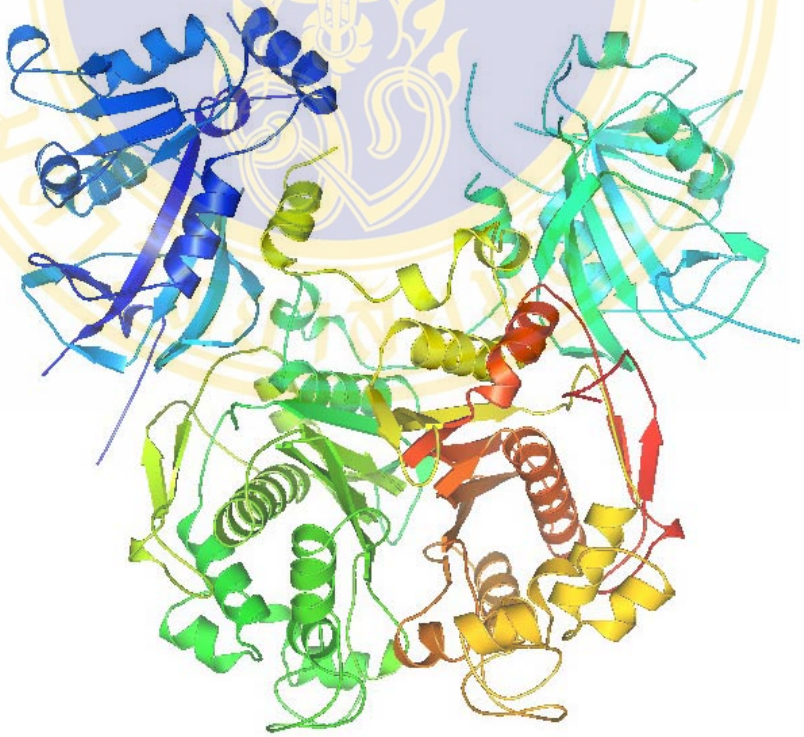

Figure 29 Structure of *Pf*-DHFR-TS. The protein consists of 4 domains. The two upper domains are dihydrofolate reductase and the two lower domains are thymidylate synthase.

Copyright by Mahidol University

Pf-DHFR consists of 8 central β-strands, and 4 flanking helices including 3 short helices. To compare with *E. coli* DHFR subdomains (82), *Pf*-DHFR can be divided with respect to the active site into 2 structural subdomains.

1. Adenosine binding subdomain (residues 38-88 in *E. coli*) comprises residues 101 to 158 which provide the binding site for adenosine moiety of the NADPH cofactor.

2. Major subdomain, or the loop domain, can be classified according to the *E. coli* structure as shown in Figure 30.

2.1 Met20 loop (equivalent to residues 9-24 in *E. coli* DHFR) lies between residues Cys18 to Asn51, which contains an extra insertion between residues 21 to 36. This loop lies over the active site to protect the cofactor and the substrate from the solvent. It also acts as a flexible gate to stabilize the nicotinamide ring in a proper geometry for the hydride transfer (82).

2.2 F-G loop is from Asn188 to Glu204 (equivalent to residues 116-132 in *E. coli* DHFR).

2.3 G-H loop is from Thr215 to Thr220 (equivalent to residues 142-150 in *E. coli* DHFR).

The latter two loops play stabilizing role via hydrogen bonding interaction with the Met20 loop. Architecture and dynamics of these loops, as studied in *E. coli* DHFR, were discussed extensively by Schnell, 2004 (82).

Copyright by Mahidol University

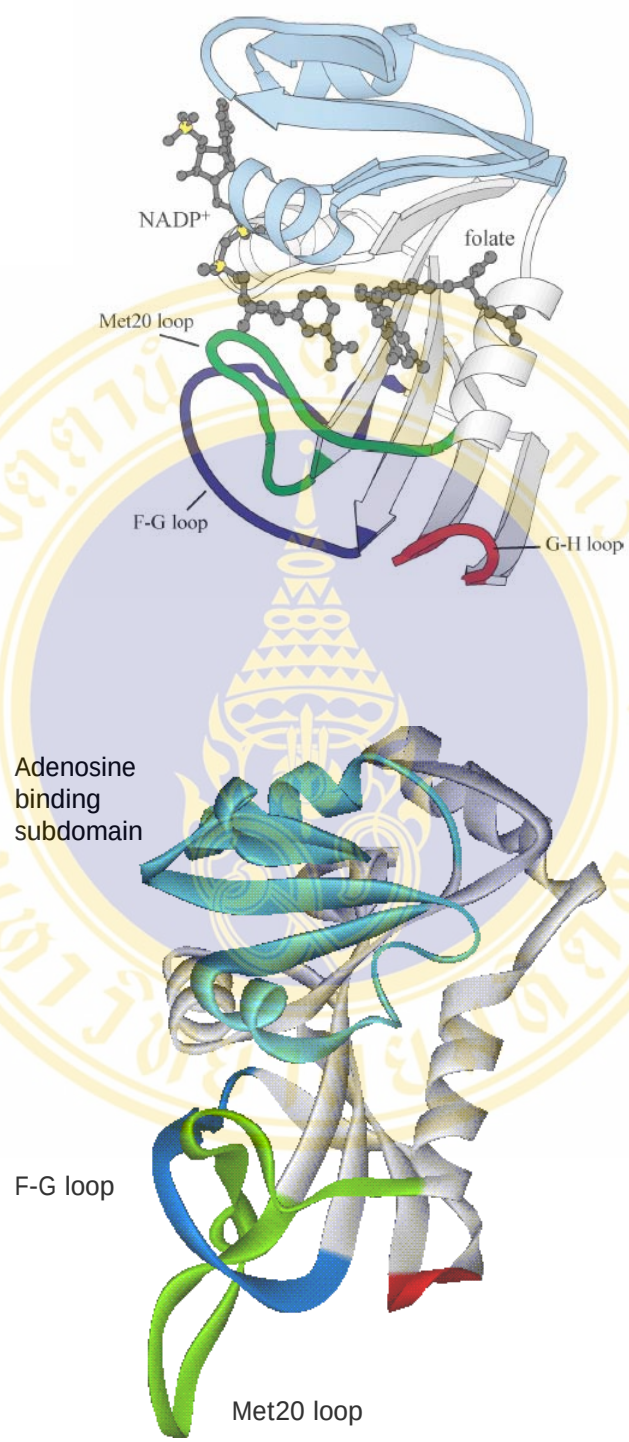

Figure 30 Structure of *Pf*-DHFR domain in comparison with *E. coli* DHFR. The major subdomain loops of *E. coli* DHFR (top panel) and *Pf*-DHFR (bottom panel) are labeled and highlighted in green (Met20), dark blue (F-G) and red (G-H). The adenosine binding subdomain is colored in cyan.

Copyright by Mahidol University

5.2 Trimethoprim Conformation

Trimethoprim binds to bacterial DHFR as high as 10,000 times tighter than it does to vertebrate DHFR (83). For years that trimethoprim has been used as one of the most effective antibacterials, the secret of trimethoprim selectivity is still a mystery.

Matthews, *et al.* proposed that the different binding modes of trimethoprim might be a major structural basis that governs the high species selectivity of this inhibitor (42, 43). In this generalization, trimethoprim in the "down" conformation, as found in bacterial DHFR, is the higher affinity conformation comparing with the "up" conformation found in vertebrate DHFR (Figure 11). He speculated that the binding pocket of chicken DHFR was too large to accommodate good, hydrophobic contact as appears in the downward conformation of trimethoprim. Thus, in vertebrate DHFRs, trimethoprim adopts the "up" conformation instead. However, the upward binding results in a loss of one hydrogen bond between the carbonyl oxygen of Val115 and 4-amino group of the pyrimidine part, and hence the lower binding affinity.

Nevertheless, the generalization was challenged by Oefner's crystal structure of human DHFR (45), whose active site was found to have a very similar size to that of *E. coli* DHFR. Therefore, such generalization regarding the difference in size of the catalytic cleft that governs the different binding modes may not be true. Other factors that may contribute to the different binding modes might be the chemical interaction and the shape complementary of trimethoprim and the amino acids within the active site of DHFR.

Since coordinates of the chicken liver and *E. coli* DHFR structures crystallized by Matthews have never been deposited on the Protein Data Bank, comparison was made in the active site of *Pf*-DHFR through manual modeling based on the information extracted from the stereo drawings published in the literature (42), also shown in Figure 11 of this thesis. From Figure 31, trimethoprim was found to adopt the downward conformation in the active site of *Pf*-DHFR, which resembles the higher affinity conformation of trimethoprim in the binding pocket of *E. coli* DHFR.

Copyright by Mahidol University

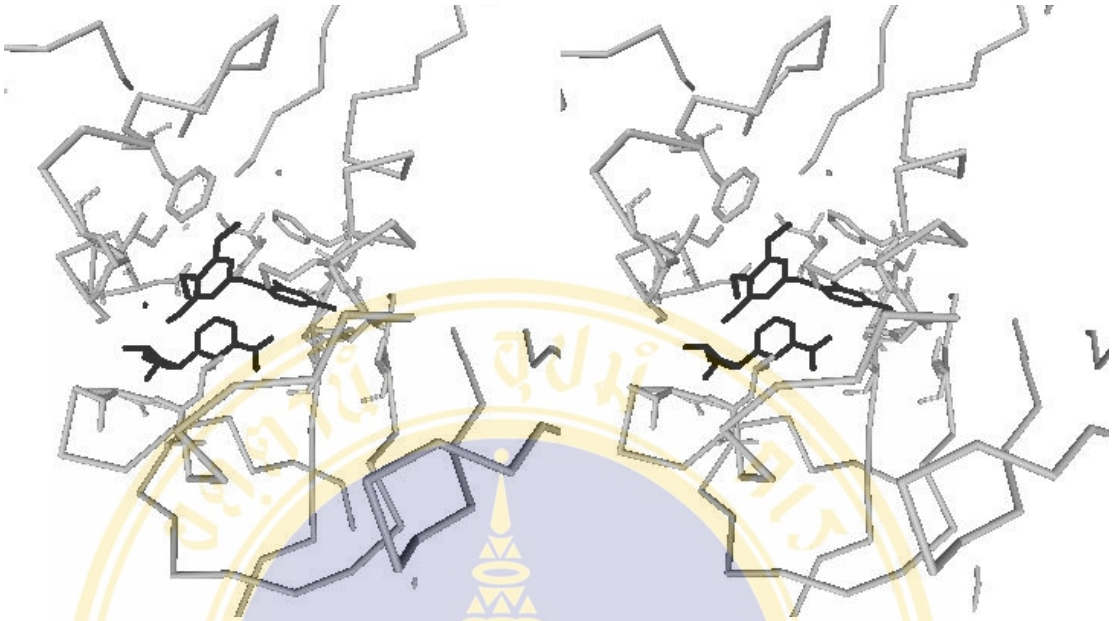

Figure 31 Stereo representation show the binding of trimethoprim and NADPH in the active site of *Pf*-DHFR. Trimethoprim binds in the downward-conformation binding mode similar to the one found in *E. coli* DHFR. The picture is obtained by orientating the equivalent amino acid residues of *Pf*-DHFR-TS structure to those specified in literatures (42, 44, 45), which are in the same view as in Figure 11 of this thesis. The protein parts are shown in gray, while trimethoprim and the nicotinamide ring of NADPH are shown in black.

Further comparison was made by superimposing *Pf*-DHFR domain of the refined structure to other two available DHFR structures complexed with trimethoprim, *i.e. Pneumocystis carinii* DHFR [PDB ID: 1DYR] (47) and *Mycobacterium tuberculosis* DHFR [PDB ID: 1DG5] (46). As illustrated in Figure 32, trimethoprim binding mode in the *P. falciparum* DHFR appears to be the same as the fungal DHFR, *P. carinii*, and the bacterial DHFR, *M. tuberculosis*. The conformation of trimethoprim found in these three complexes is the same as the downward conformation found in *E.coli* DHFR. Hence, the assumption that downward conformation of trimethoprim contributed greater inhibitory effect is true for *P. falciparum* DHFR. For the detail of trimethoprim torsion angles within various DHFR species, see Table 16.

Copyright by Mahidol University

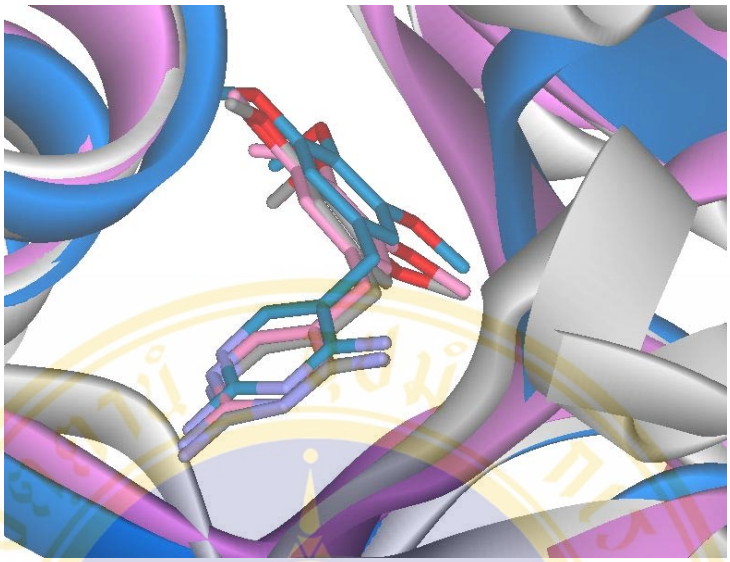

Figure 32 Binding mode of trimethoprim in the active site of *P. falciparum* DHFR, *P. carinii* DHFR, and *M. tuberculosis* DHFR. Superposition of the three complex structures shows the same binding conformation of trimethoprim in *Pf*-DHFR (gray), *P. carinii* DHFR (pink), and *M. tuberculosis* DHFR (blue).

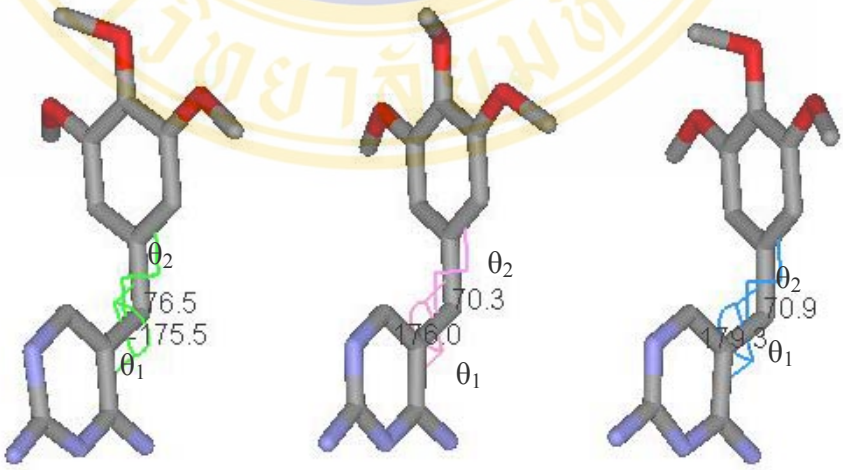

Figure 33 Torsion angles of trimethoprim measured from the crystal structures of *Pf*-DHFR-TS complex (left), *P. carinii* DHFR complex (middle) and *M. tuberculosis* DHFR complex (right)

Copyright by Mahidol University

Table 16 Torsion angles of trimethoprim found in DHFR active site from various organisms.

Enzyme Complex	Torsion θ_1	Torsion θ_2
trimethoprim/NADPH/*P. falciparum* DHFR↓	184.5º (-175.5º)	76.5º
trimethoprim/NADPH/chicken liver DHFR↑ (42)	275º (-85º)	102º
trimethoprim/*E. coli* DHFR↓ (42)	177º	76º
trimethoprim/NADPH/*E. coli* DHFR↓ (84)	192º	56º
trimethoprim/NADPH/*P. carinii* DHFR↓ (47)	176º	70.3º
trimethoprim/NADPH/*M. tuberculosis* DHFR↓ (46)	179.3º	70.9º

↓ "Down" conformation (trimethoprim binds upward to the upper binding site)

↑ "Up" conformation (trimethoprim binds downward to the lower binding site)

In addition to the binding mode observation, torsion angles of trimethoprim in *P. falciparum* DHFR, *P. carinii* DHFR (47) and *M. tuberculosis* DHFR (46) are measured and compared to other reported values as shown in Table 16 (42, 84). The torsion angles (θ_1), as determined in Figure 33, measured from the obtained structure of ternary *Pf*-DHFR/NADPH/trimethoprim complex is somewhat between the corresponding torsion angles found in the binary *E. coli* DHFR (*E. coli* DHFR/trimethoprim) and the ternary *E. coli* DHFR (*E. coli* DHFR/trimethoprim/ NADPH) complexes (84). Hence, it implies that the two torsion angles of trimethoprim may be affected by the surrounded electrostatic or steric environment within the active site.

Based on evidence from crystal structures of mouse DHFRs, trimethoprim showed the ability to bind in both the upward conformation for the strain L1210 (44) and the downward conformation for the strain S180 (85). However, the upward conformation seems impossible for both the wild-type and the C59R+S108N

Copyright by Mahidol University

P. falciparum DHFR due to the steric clash of m-methoxy group of trimethoprim with Ile164. This position is equivalent to Val115 for all the reported "up" conformation–trimethoprim complexes, *i.e.* chicken liver DHFR (42), human DHFR (45) and mouse L1210 DHFR (44) as well as in bovine liver and porcine liver DHFR. From structure-based sequence alignment of DHFRs from various species, *e.g. Candida albicans, Escherichia coli, Haloferax volcanii, Mycobacterium tuberculosis, Pneumocystis carinii, Thermotoga maritima, Staphylococcus aureus,* amino acids at the position equivalent to Ile164 in *P. falciparum* DHFR (or Val115 in chicken liver DHFR) were isoleucines. The larger side chain of isoleucine fills up the "upper" cavity of the active site, and makes the space unavailable for adopting trimethoprim in the "up" conformation. Therefore, it is very likely that Val115, which is found to be Ile164 in *Pf*-DHFR, is the major factor that allows the "up" conformation to occur.

Such steric interaction at Val115, which might determine the binding conformation of trimethoprim, might be the answer to the high species selectivity that trimethoprim used to discriminate vertebrate DHFR. However, an explanation of what makes the downward conformation bind tighter to DHFR active site than the upward conformation is still unclear because of the lack of available DHFR coordinates with trimethoprim in its up conformation.

5.3 Molecular Interactions in Trimethoprim–*Pf*-DHFR Complex

As introduced previously, the main objective of this research was to find structural explanation for the slight difference between the K_i values of trimethoprim and pyrimethamine towards the *P. f*alciparum DHFR active site.

From Table 17, it can be seen that the K_i of trimethoprim in *Pf*-DHFR complexes were in the range comparable to the active and inactive form representing by *E.coli* and human DHFR, respectively. Thus, the structure of *Pf*-DHFR offer various ranges of binding affinities to trimethoprim, and it can be used for an implication to understanding of trimethoprim's selectivity in the C59R+S108N *Pf*-DHFR. The obtained crystal structures of C59+S108N *Pf*-DHFR in complex with

Copyright by Mahidol University

trimethoprim exhibit 5 times –less binding affinities comparing to the same protein structure in complex with pyrimethamine. These two complexes can be compared directly to derive the cause of difference in binding. Available structure of the wild-type *Pf*-DHFR complexed with WR99210 was used to guide in making a comparison.

Table 17 Inhibition constants reflecting trimethoprim's species selectivity in *Pf*-DHFR. Numbers in parentheses are calculated by dividing the K_i of trimethoprim in C59R+S108N *Pf*-DHFR by the K_i reported therein, and thus represent the relative binding affinities with respect to the trimethoprim/C59R+S108N *Pf*-DHFR complex in fold.

DHFR	K_i (nM)	
	Pyrimethamine	**Trimethoprim**
E. coli* DHFR (RT 500)	-	0.08 (3,026)
Wild-type *Pf*-DHFR (TM4/8.2)**	0.6 ± 0.2 (403.5)	10.3 ± 0.5 (23.5)
C59R+S108N *Pf*-DHFR (K1CB1)**	53.9 ± 6.5 (4.5)	242.1 ± 40.1 (1)
Human DHFR*	-	196 (1.2)

* K_i obtained from Margosiak, 1993 (86)

** K_i obtained from Sirichaiwat, 2004 (49)

5.3.1 Structural Basis toward the Resistance of C59R+S108N *Pf*-DHFR

The refined structure obtained in this research, C59R+S108N *Pf*-DHFR/NADPH/trimethoprim complex, was superimposed to the available structure of C59R+S108N *Pf*-DHFR/NADPH/pyrimethamine [PDB ID: 1J3J] (39). The two proteins are very similar in overall structural motifs, as shown in Figure 34. The only

Copyright by Mahidol University

obvious difference is found in the range of S111 to Asn121, which will be called the S111 loop in this thesis, as shown in Figure 35.

Figure 34 Stereo image showing superposition of the trimethoprim and pyrimethamine complexes of C59R+S108N *Pf*-DHFR. The trimethoprim complex drawn in gray and the pyrimethamine complex shown in cyan are very similar.

Copyright by Mahidol University

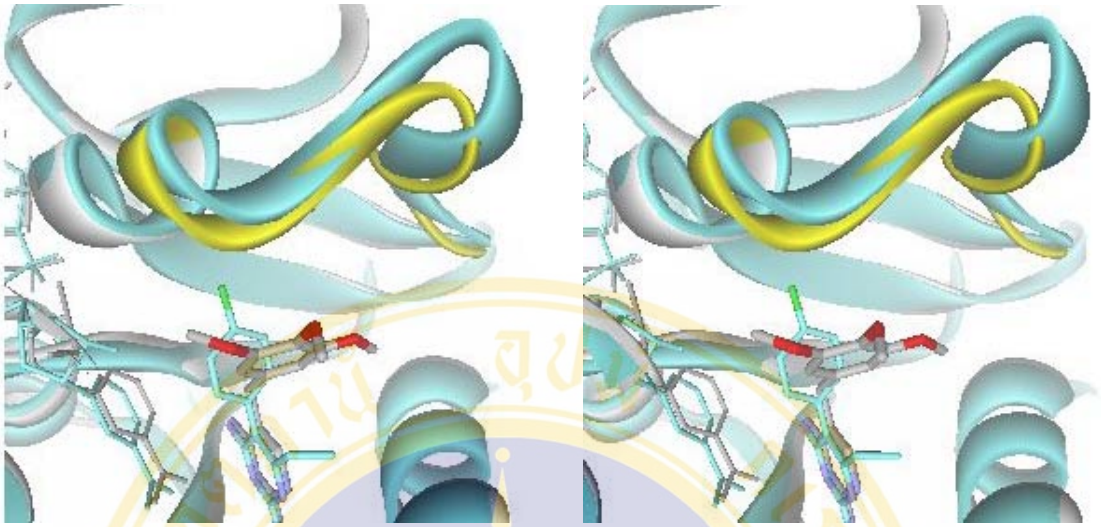

Figure 35 Significant loop shift is found within trimethoprim and pyrimethamine complexes. The S111 loop (yellow) of the C59R+S108N *Pf*-DHFR/NADPH/ trimethoprim complex (gray) lies closer toward the inhibitor's side than the one found in C59R+S108N *Pf*-DHFR/NADPH/pyrimethamine complex (cyan).

It seems straightforward that the S111 loop was pushed upward to accommodate the longer rigid length of pyrimethamine (Figure 35). To assure such hypothesis, the structure of wild-type *Pf*-DHFR in complex with WR99210, which has a shorter rigid length, was superimposed to the two structures. However, the result was astonishing because the S111 loop of wild-type *Pf*-DHFR complexed with WR99210 was found superimposable with the one in pyrimethamine complex instead (Figure 36). Thus, a better explanation is needed to explain why the S111 loop movement is positioned so closed to the trimethoprim. Similarities and differences were determined to gain more information about such major structural changes.

Copyright by Mahidol University

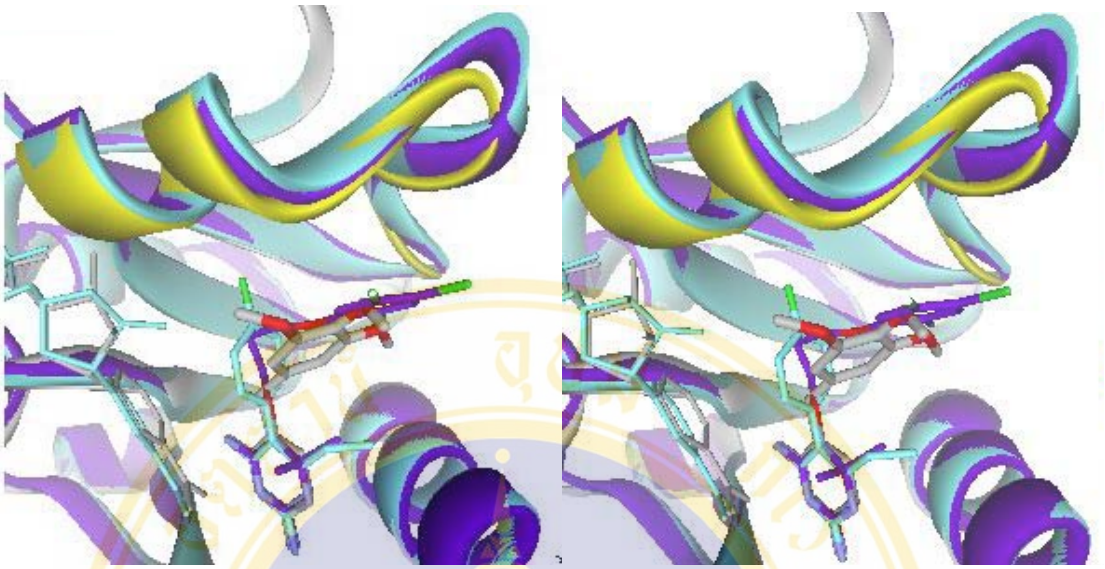

Figure 36 Superposition of S111 loops of C59R+S108N *Pf*-DHFR/NADPH/pyrimethamine complex (cyan) and wild-type *Pf*-DHFR/NADPH/WR99210 (dark blue). This illustration poses the question why the catalytic loop of C59R+S108N*Pf*-DHFR/NADPH/trimethoprim (yellow) was shifted towards trimethoprim.

From the similarity point of view, the diaminopyrimidine rings of both compounds were found at almost the same position as they form hydrogen bonds with Asp54. This amino acid residue is equivalent to Asp27 in *E. coli*, which has been reported to be the only ionizable group that has potential to donate a proton to the N5 atom of the pterin ring within the active site of *E. coli* DHFR (87). The 4-amino groups from both compounds point to a cleft of negative potential comprising carbonyl groups from residues Ile14 and Ile164, and also a phenol group of Tyr170 of *Pf*-DHFR (Figure 37). Phenylalanine 58 is also likely to create a Pi-Pi stacking with the pyrimidine rings of both compounds, as can be seen in Figure 38.

Copyright by Mahidol University

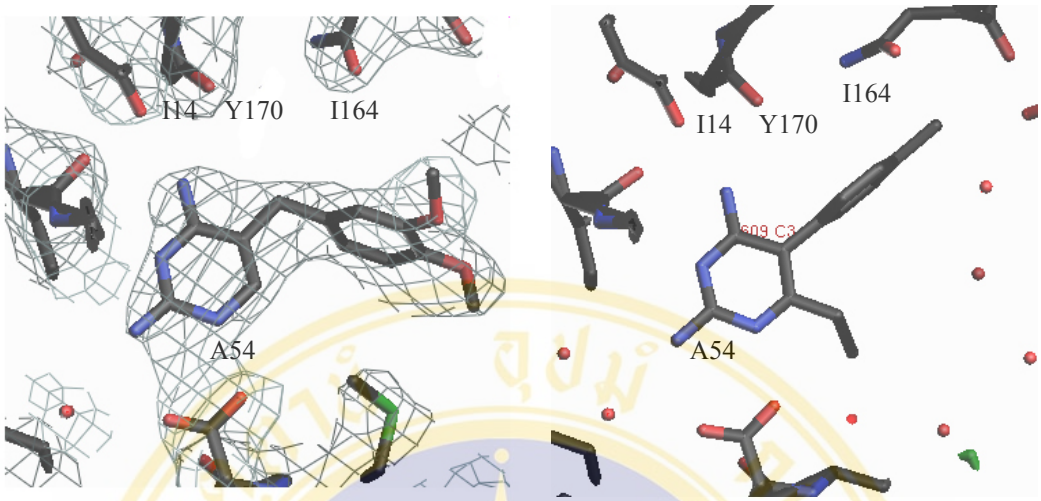

Figure 37 Major interacting residues around the pyrimidine rings of trimethoprim and pyrimethamine within the *Pf*-DHFR active sites. Both the trimethoprim–*Pf*-DHFR complex (left panel) and the pyrimethamine–*Pf*-DHFR complex (right panel) show similar interactions around the pyrimidine ring moieties. One of the m-methoxyl group of trimethoprim is missing from this Figure.

The obvious differences are found from the two residues that are characteristics of the double mutant K1CB1 *Pf*-DHFR, which are arginine at the position 59 and serine at the position 108.

It seems that residue 59, which was mutated from cysteine to arginine, is located too far apart from both inhibitors. However, the effect of these mutations cannot be neglected. In the pyrimethamine–*Pf*-DHFR complex, Arg59 in cooperation with Arg122 forming a large water network comprises at least 6 water molecules (Figure 38). This water network is formed from both arginine residues toward the hydroxyl group of ribose sugar of NADPH. On the other hand, the same area in the trimethoprim complex is filled with the trimethoxyphenyl moiety of trimethoprim and only one water molecule. Hence, this water network implies that the catalytic cleft opening of trimethoprim–*Pf*-DHFR complex was almost free of water molecules comparing to that of the pyrimethamine complex.

Copyright by Mahidol University

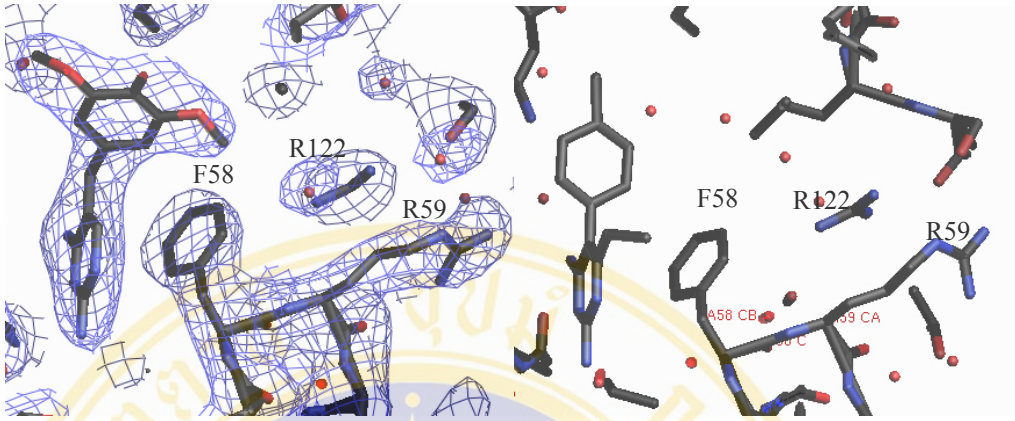

Figure 38 Comparison of water network within the active site of pyrimethamine and trimethoprim complexes. At least 6 water molecules are found in the pyrimethamine complex (right panel), while trimethoprim complex (left panel) possesses only one water molecule.

The molecular interactions within the *Pf*-DHFR were closely observed, and the cause of the S111 loop movement was found to arise from the residue number 59. As shown in Figure 39, the arginine within both the pyrimethamine complex and the trimethoprim complex form charge-polar and polar-polar interactions with carbonyl oxygen and hydroxyl oxygen of Ser120, and also another hydrogen bond with hydroxyl oxygen of Thr63. The effects of these three interactions could largely affect the flexibility of the catalytic clefts. Hence, the shifting of the S111 loop found in trimethoprim was the consequence of the binding of upper and lower jaws (Figure 39).

The result is obvious in the crystal structure of C59R+S108N *Pf*-DHFR in complex with trimethoprim, because the rigid length of trimethoprim is not long enough to persist the clipping. Thus, the loop lies closed to the active site and generates a large, flat cavity to accommodate the trimethoxyphenyl group of trimethoprim. There was no electron density of water found within this flat cleft, hence trimethoprim could occupy a large hydrophobic space with the arms of catalytic loop to prevent the trimethoxyphenyl ring from interacting with water molecules. On

Copyright by Mahidol University

the other hand, pyrimethamine has a longer rigid length and stays deep in the catalytic cleft, thus it can push out the active site to avoid interaction with the chlorine atom on the phenyl ring. Therefore, the S111 loop found in the crystal structure of pyrimethamine complex is not altered much comparing to the wild-type *Pf*-DHFR complex.

Instead of being arginine like in C59R+S108N DHFR mutant, residue 59 in the wild-type *Pf*-DHFR is cysteine, which does not possess any of the three interactions, as illustrated in Figure 39.

Figure 39. Stereo image of arginine at the position 59 that affects the catalytic cleft opening. The trimethoprim complex is shown in gray, pyrimethamine in cyan. The wild-type *Pf*-DHFR is in pink.

This evidence could contribute to the reason why K1CB1 mutant is highly resistant to both pyrimethamine and trimethoprim. The sticky jaws and narrower catalytic cleft could certainly affect the dynamic and kinetic properties of the protein.

Copyright by Mahidol University

Another interesting feature is at the position 108, conformation of Asn108 in pyrimethamine complex is affected by the chlorine atom of pyrimethamine such that the amine group turns atom towards the ribose of NADPH to avoid steric interaction with chlorine. On the contrary, Asn108 in the trimethoprim complex stays quite far from direct interaction (~4 Å) with trimethoprim; and therefore, the amide group could turn to the empty space on the trimethoprim side. The different rotamers of Asn108 is illustrated in Figure 40.

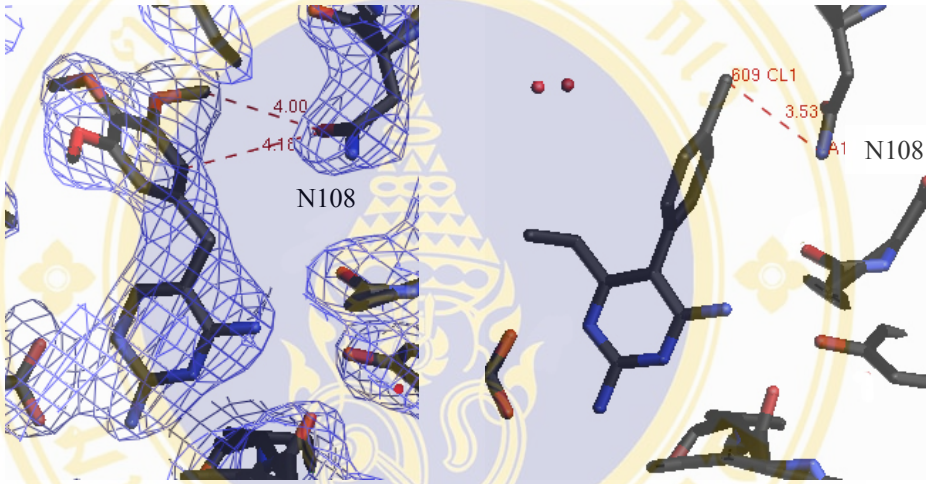

Figure 40 Comparison of the effects of trimethoprim (left panel) and pyrimethamine (right panel) on the conformation of Asn108.

As shown in Figure 41, side chain of Asn108 in the pyrimethamine complex is positioned between the chlorine atom of the pyrimethamine and Gly165. In order to avoid steric clash with the carbonyl oxygen of Gly165 and to maintain favorable polar-polar interaction with the chlorine atom of pyrimethamine, the side chain of Asn108 is positioned away from pyrimethamine and toward Gly165.

Since trimethoprim does not occupy the space equivalent to the one occupied by the chlorine atom of pyrimethamine, the side chain of Asn108 in trimethoprim complex could turn towards the inhibitor while it stays about 4 Å away from the methoxy group of trimethoprim (Figure 41). However, the polar side chain of asparagine does not make good interaction with very hydrophobic part of

Copyright by Mahidol University

trimethoprim it faces. Moreover, the space is too small for the water molecules to fill in, and leave the vacuum space to occur in the core structure of the protein. This makes the interaction much less favorable than the pyrimethamine complex. The situation is very different for serine that presents in the wild-type complex. The shorter side chain allows Ser108 to stay away from Gly165 in the same direction as from the inhibitor.

In combination with the effect of catalytic jaws clipping, the steric interaction caused by serine at position 108 could lower the binding affinities in large part because inhibitors bind less tightly and the enzyme catalyzes reaction with some difficulty.

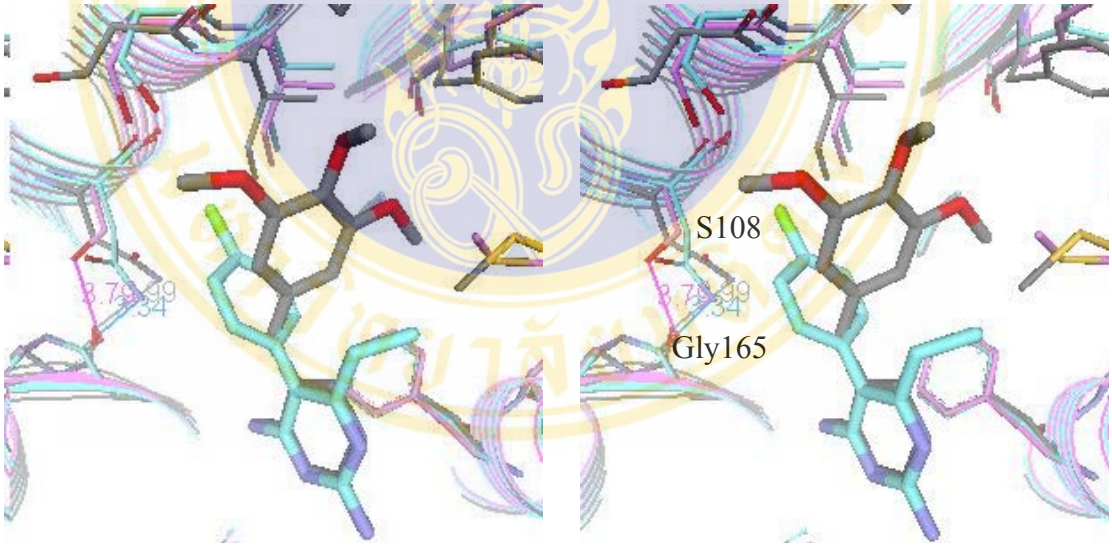

Figure 41 Stereo image showing the highly unfavorable steric interactions found at the position 108. The trimethoprim complex is shown in gray, pyrimethamine in cyan. The wild-type *Pf*-DHFR is in pink.

Copyright by Mahidol University

Another reason of difference in binding affinity should be the polar-polar interaction governed by partial charge of chlorine which is strengthen in the hydrophobic part of protein, while trimethoxyphenyl moiety of trimethoprim could only form non-specific van der Waals interactions.

In the trimethoprim complex, the protein side chains around catalytic cleft attempt to promote the binding stability of trimethoprim by excluding water from the hydrophobic environment and harboring the trimethoxyphenyl group therein. As shown in Figure 42, side chain of Met55 in trimethoprim complex points into the active site to make direct contact (~ 3.6 Å) with trimethoprim (Figure 42, left panel).

In the pyrimethamine complex, the chlorine atom protrudes the space between S111 and I112 and makes a stronger, polar-polar, interaction. The side chain of Met55 points away from the inhibitor towards the opening into the solution to avoid steric clash with the ethyl substituent on the C_6 atom of the pyrimethamine. Amino acid side chains around are slightly adjusted to accommodate the more favorable interaction with the chlorine atom of the chlorophenyl ring (Figure 42, right panel).

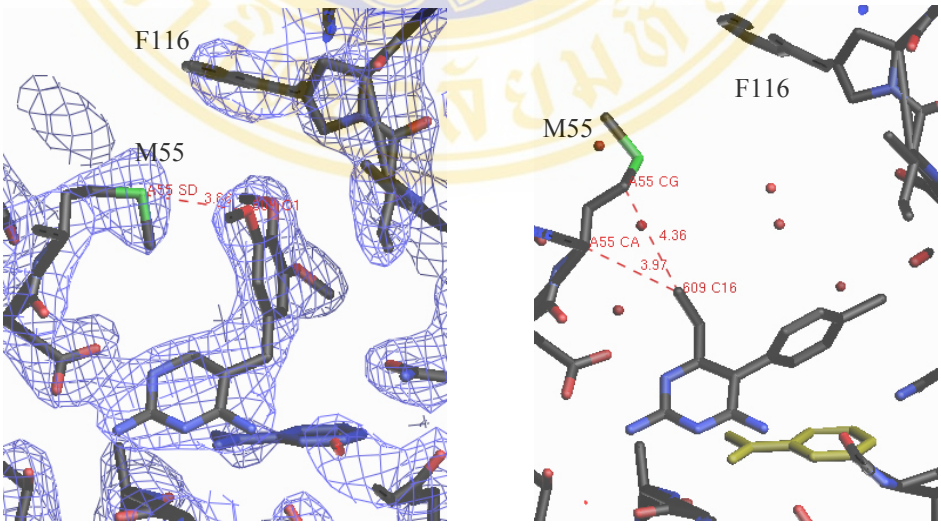

Figure 42 The *Pf*-DHFR catalytic cleft entry. Trimethoprim in the active site of *Pf*-DHFR is harbored by Met55 and also Phe116, while pyrimethamine is more exposed to water as a contribution of Met55 conformation and the position shift of S111 loop (right panel).

Copyright by Mahidol University

5.3.2 Trimethoprim in Complex with C59R+S108N *Pf*-DHFR and NADPH

Various assumptions have been proposed to explain the enhancement of binding affinity of trimethoprim to *E. coli* DHFR besides the larger catalytic cleft of chicken liver DHFR and mouse L1210 DHFR, which results in the decreasing number of contacts between inhibitor, cofactor, and enzyme, as previously discussed in the Section 5.2 (43). Among the most popular explanations is the direct interactions between inhibitors and the cofactor which results in positive cooperativities in bacterial DHFR and negative cooperativities in vertebrate DHFR (88, 89). Such great binding affinity was also speculated to be the consequence of a much greater solvent exposure found around the methoxy groups in *E. coli* DHFR ternary complex, based on theoretical studies about hydrophilic character of methoxy substituents of trimethoprim (85).

Major interactions for the pyrimidine ring of trimethoprim are already discussed in comparison with pyrimethamine. N_1 of pyrimidine ring of trimethoprim made hydrogen bond with Asp54, and 4-amino group make hydrogen bonds with carbonyl oxygen atoms of Ile164 and Ile14. This ring seems almost stacking with the nicotinamide ring of NADPH.

For the trimethoxyphenyl group, Ser111, Ile112, Pro113 lie on top of the ring and act as a ceiling of the cleft, as shown in Figure 43. The two m-methoxy groups rest on the sidechain of Leu46 and Met55. It is interesting that the residue equivalent to Leu46 in *E. coli* DHFR is methionine, and the one equivalent to Met55 is leucine. It implies that the trimethoxyphenyl ring seems to make good pharmacophore in the leucine-methionine neighboring. Phe116 and Met55 move closer to facilitate the hydrophobic environment as already mentioned in comparison with pyrimethamine, see all interactions in Figure 43.

Copyright by Mahidol University

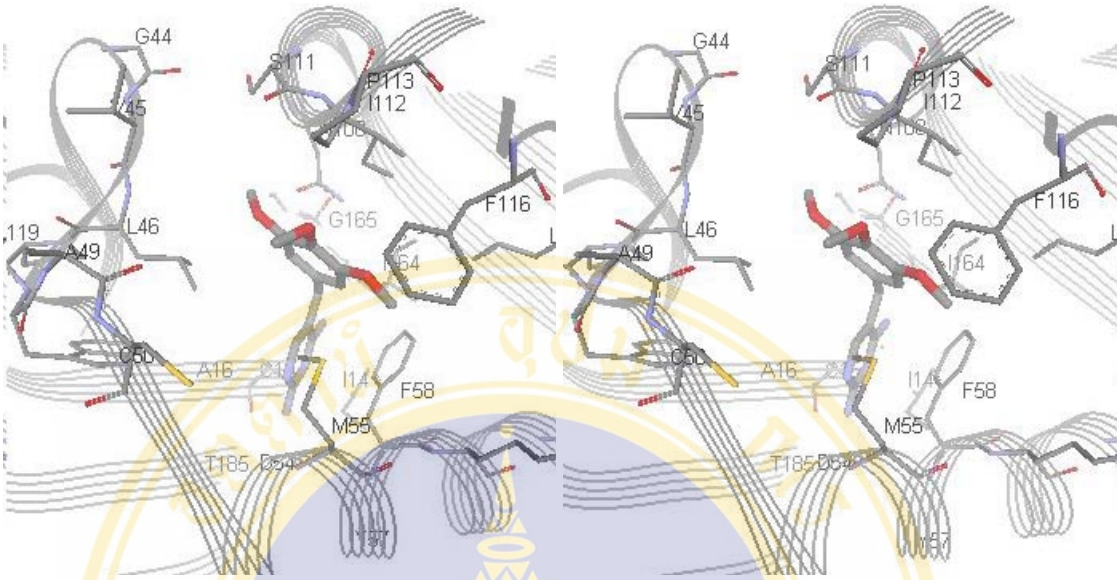

Figure 43 Chemical interaction of within 7 Å from trimethoprim in the active site of C59R+S108N *Pf*-DHFR.

The results from this thesis cannot answer much about binding affinities. Due to the very low binding affinity of trimethoprim to C59R+S108N *Pf*-DHFR (K_i = 242 nM), trimethoprim binds to this mutant even poorer than human DHFR. Thus, there were not very many chemical interactions observed around the inhibitor in this complex. The electron density of nicotinamide ring of NADPH is very weak with atoms of high B-factor, and hence should be said as invisible.

As previously discussed, trimethoprim selectivity should not be the effect of the catalytic cleft size. From the structure of *Pf*-DHFR/trimethoprim/NADPH complex, there is quite low cooperativity between inhibitor and cofactor. The obviously low water exposure may support theoretical studies concerning the hydrophilic character of methoxy groups, as the active site of trimethoprim *Pf*-DHFR complex is almost free of water molecule and a very low binding affinities is observed, comparing to other *Pf*-DHFR complexes.

Copyright by Mahidol University

CHAPTER 6
CONCLUSION

X-ray diffraction data were collected and processed with R-merge of 8.3 % to 2.6 Å resolution. The diffraction data showed the crystal was of orthorhombic space group $P2_12_12_1$ with unit-cell parameters $\alpha = 90^o$, $\beta = 90^o$, $\gamma = 90^o$, a = 56.9 Å, b = 154.9 Å, c = 165.3 Å and 2 molecules/asymmetric unit (V_M=2.5 $Å^3$/Da). The structure was solved by Difference Fourier Technique using the previously known *Pf*-DHFR-TS K1CB1 (C59R+S108N double mutant) complexed with pyrimethamine/NADPH/dUMP as the template.

Structural investigation reveals that trimethoprim forms van der Waals interaction and hydrogen bonds in the *Pf*-DHFR–TS active site; whereas pyrimethamine has a greater binding affinity via a consequence of hydrogen bonds, polar-polar, and van der Waals interactions that provide a better fit in the active site pocket. Both inhibitors occupy the same binding pocket and make similar chemical interactions with surrounding amino acid residues. Thus, mutations of some of these amino acids that cause resistance to pyrimethamine might also trigger resistance to trimethoprim, and vice versa. The role of Ile164, which is equivalent to V115 in various vertebrate DHFRs, in species selectivity of trimethoprim is proposed. The resistance mechanism of C59R+S108N *Pf*-DHFR mutant was discussed.

Copyright by Mahidol University

REFERENCES

1. Fujioka H, Aikawa M. The malaria parasite and its life-cycle. Amsterdam, Netherlands: Harwood Academic Publishers; 1999.
2. Bannister L, G. M. The ins, outs and roundabouts of malaria. Trends Parasitol 2003;19(5):209-213.
3. RBM / WHO. RBM Infosheet. 1-11. In http://www.who.int/mediacentre/factsheets/fs094/en/; 2002.
4. Olliaro PL, Yuthavong, Y. An overview of chemotherapeutic targets for antimalarial drug discovery. Pharmacol. Ther. 1999;81(2):91-110.
5. Goldberg DE, Slater AFG, Cerami A, Henderson GB. Hemoglobin degradation in the malaria parasite *Plasmodium falciparum*: an ordered process in a unique organelle. Proc. Natl. Acad. Sci. U.S.A. 1990;87:2931-2935.
6. Gluzman IY, Francis SE, Oksman A, Smith C, Duffin K, Goldberg DE. Order and specificity of the *Plasmodium falciparum* hemoglobin degradation pathway. J. Clin. Invest. 1994;93:1602-1607.
7. Hunt NH, Stocker R. Oxidative stress and the redox status of malaria-infected erythrocytes. Blood Cells 1990;16:499-526.
8. Goldberg DE. Plasmodial hemoglobin degradation: an ordered pathway in a specialized organelle. Infect. Agents Dis. 1992;1:207-211.
9. Sullivan DJ, Gluzman IY, Russell DG, Goldberg DE. On the molecular mechanism of chloroquine's antimalarial action. Proc Natl Acad Sci USA 1996;93:11865-11870.
10. Olliaro P. Mode of action and mechanisms of resistance for antimalarials drugs. Pharmacol. Ther. 2001;89:207-219.
11. Roland S, Ferone R, Harvey RJ, Styles VL, Morrison RW. The characteristics and significance of sulfonamides as substrates for *Escherichia coli* dihydropteroate synthase. J. Biol. Chem. 1979;254:10337-10345.

Copyright by Mahidol University

12. Blaney JM, Hansch C, Silipo C, Vittoria A. Structure-activity relationships of dihydrofolate reductase inhibitors. Chem. Rev. 1984;84:333-407.
13. Warhurst DC. Resistance to antifolates in *Plasmodium falciparum*, the causative agent of tropical malaria. Science Progress 2002;85(1):89-111.
14. Phillips RS. Malaria. Southampton, UK: The Camelot Press Ltd.; 1983.
15. Bruce-Chwatt LJ. Essential malariology. Southampton, UK: The Camelot Press Ltd.; 1980.
16. Ridley RG. Medical need, scientific opportunity and the drive for antimalarial drugs. Nature 2002;415:686-693.
17. Day KP. The epidemiology of malaria. Amsterdam, Netherlands: Harwood Academic Publishers; 1999.
18. China Cooperative Research Group on Qinghaosu and Its Derivatives as Antimalarials. Chemical studies on qinghaosu (artemisinine). J Trad Chin Med 1982;2:3-8.
19. China Cooperative Research Group on Qinghaosu and Its Derivatives as Antimalarials. The chemistry and synthesis of qinghaosu derivatives. J Trad Chin Med 1982;2:9-16.
20. Meshnick SR. Artemisinin and its derivatives. In: Rosenthal PJ, editor. Antimalarial Chemotherapy: Mechanisms of action, resistance and new directions in drug discovery. New Jersey: Humana Press Inc.; 2001.
21. White NJ. Assessment of the pharmacodynamic properties of antimalarial drugs in vivo. Antimicrob Agents Chemother 1997;41(7):1413-22.
22. Carrington HC, Crowther AF, Davey DG, Levi AA, Rose FL. A metabolite of "Paludrine" with high antimalarial activity. Nature 1951;168(1080).
23. Fry M, Pudney M. Site of action of the antimalarial hydroxynaphthoquinone, 2-[trans-4-(4'-chlorophenyl) cyclohexyl]-3-hydroxy-1,4-naphthoquinone (566C80). Biochem Pharmacol 1992;43(7):1545-53.
24. RBM / WHO. The use of antimalarial drugs. Report of an informal consultation. Geneva: WHO; 2001 November 17, 2000.
25. WHO. Conclusions of a Technical Consultation Convened by WHO. In http://www.who.int/hiv/pub/prev_care/malaria/en/; 2004.

Copyright by Mahidol University

26. Basco LK, Tahar R, Ringwald P. Molecular basis of *in vivo* resistance to sulfadoxine-pyrimethamine in African adult patients infected with *Plasmodium falciparum* malaria parasites. Antimicrob. Agents Chemother. 1998;42(7):1811-1814.
27. Wongsrichanalai C, Pickard AL, Wernsdorfer WH, Meshnick SR. Epidemiology of drug-resistant malaria. Lancet Infectious Diseases 2002;2:209-218.
28. Gill CJ, Sabin LL, Tham J, Hamer DH. Reconsidering empirical cotrimoxazole prophylaxis for infants exposed to HIV infection. Bull World Health Organ 2004;82(4).
29. WHO Division of Diarrhoeal and Acute Respiratory Disease Control. Integrated management of the sick child. Bull World Health Organ 1995;73(735-740).
30. Iyer JK, Milhous WK, Cortese JF, Kublin JG, Plowe CV. *Plasmodium falciparum* cross-resistance between trimethoprim and pyrimethamine. Lancet 2001;358:1066-1067.
31. Khalil I, RoNN AM, Alifrangis M, Gabar HA, Satti GMH, Bygbjerg IC. Dihydrofolate reductase and dihydropteroate synthase genotypes associated with in vitro resistance of *Plasmodium falciparum* to pyrimethamine, trimethoprim, sulfadoxine, and sulfamethoxazole. Am. J. Trop. Med. Hyg. 2003;68(5):586-589.
32. Anglaret X. Trimethoprim-sulfamethoxazole prophylaxis in sub-Saharan Africa. Lancet 2001;358(1027-1028).
33. Whitty CJ, Jaffar S. *Plasmodium falciparum* cross resistance. Lancet 2002;359(9300):80.
34. Peterson DS, Walliker D, Wellems TE. Evidence that a point mutation in dihydrofolate reductase-thymidylate synthase confers resistance to pyrimethamine in falciparum malaria. Proc Natl Acad Sci U S A 1988;85(23):9114-8.
35. Peterson DS, Milhous WK, Wellems TE. Molecular basis of differential resistance to cycloguanil and pyrimethamine in *Plasmodium falciparum* malaria. Proc. Natl. Acad. Sci. USA 1990;87:3018-3022.

Copyright by Mahidol University

36. Sirawaraporn W, Sathitkul T, Sirawaraporn R, Yuthavong Y, Santi DV. Antifolate-resistant mutants of *Plasmodium falciparum* dihydrofolate reductase. Proc. Natl. Acad. Sci. USA 1997;94:1124-1129.
37. Sirawaraporn W, Yongkiettrakul S, Sirawaraporn R, Yuthavong Y, Santi DV. *Plasmodium falciparum*: Asparagine mutant at residue 108 of dihydrofolate reductase is an optimal antifolate-resistant single mutant. Exp. Parasitol. 1997;87(245-252).
38. Rathod PK, Phillips MA. Prized malaria drug target nailed. Nat Struct Biol 2003;10(5):316-8.
39. Yuvaniyama J, Chitnumsub P, Kamchonwongpaisan S, Vanichtanankul J, Sirawaraporn W, Taylor P, Walkinshaw MD, Yuthavong Y. Insights into antifolate resistance from malarial DHFR-TS structures. Nat Struct Biol 2003;10(5):357-65.
40. Benkovic SJ, Hammes-Schiffer S. A perspective on enzyme catalysis. Science 2003;301(5637):1196-202.
41. Foote SJ, Galatis D, Cowman AF. Amino acids in the dihydrofolate reductase-thymidylate synthase gene of *Plasmodium falciparum* involved in cycloguanil resistance differ from those involved in pyrimethamine resistance. Proc. Natl. Acad. Sci. USA 1990;87(87):3014-3017.
42. Matthews DA, Bolin JT, Burridge JM, Filman DJ, Volz KW, Kaufman BT, Beddell CR, Champness JN, Stammers DK, Kraut J. Refined Crystal Structures of *Escherichia coli* and Chicken Liver Dihydrofolate Reductase Containing Bound Trimethoprim. J. Biol. Chem. 1985;260(1):381-391.
43. Matthews DA, Bolin JT, Burridge JM, Filman DJ, Volz KW, Kraut J. Dihydrofolate reductase: The stereochemistry of inhibitor selectivity. J. Biol. Chem. 1985;260(1):392-399.
44. Stammers DK, Champness JN, Beddell CR, Dann EE, Geddes AJ, Ogg D, North ACT. The structure of mouse L1210 dihydrofolate reductase-drug complexes and the construction of a model of human enzyme. FEBS Lett. 1987;218(1):178-184.
45. Oefner C, D'Arcy A, Winkler FK. Crystal structure of human dihydrofolate reductase complexed with folate. Eur J Biochem 1988;174(2):377-385.

Copyright by Mahidol University

46. Li R, Sirawaraporn R, Chitnumsub P, Sirawaraporn W, Wooden J, Athappilly F, Turley S, Hol WG. Three-dimensional structure of *M. tuberculosis* dihydrofolate reductase reveals opportunities for the design of novel tuberculosis drugs. J. Mol. Biol. 2000;295(2):307-323.

47. Champness JN, Achari A, Ballantine SP, Bryant PK, Delves CJ, Stammers DK. The structure of *Pneumocystis Carinii* dihydrofolate reducatse to 1.9 angstroms resolution. Structure 1994;2(10):915-924.

48. Tarnchompoo B, Sirichaiwat C, Phupong W, Intaraudom C, Sirawaraporn W, Kamchonwongpaisan S, Vanichtanankul J, Thebtaranonth Y, Yuthavong Y. Development of 2,4-Diaminopyrimidines as Antimalarials Based on Inhibition of the S108N and C59R+S108N Mutants of Dihydrofolate Reductase from Pyrimethamine-Resistant *Plasmodium falciparum*. J. Med. Chem. 2002;45(6):1244-1252.

49. Sirichaiwat C, Intaraudom C, Kamchonwongpaisan S, Vanichtanankul J, Thebtaranonth Y, Yuthavong Y. Target guided synthesis of 5-benzyl-2,4-diamonopyrimidines: their antimalarial activities and binding affinities to wild type and mutant dihydrofolate reductases from *Plasmodium falciparum*. J Med Chem 2004;47(2):345-54.

50. Ries-Kautt M, Ducruix A. From solutions to crystals with a physico-chemical aspect. 2 ed. New York: Oxford University Press; 1999.

51. Reiss-Husson F, Picot D. Crystallization of membrane proteins. 2 ed. New York: Oxford University Press; 1999.

52. Chitnumsub P, Yuvaniyama J, Vanichtanankul J, Kamchonwongpaisan S, Walkinshaw MD, Yuthavong Y. Characterization, crystallization and preliminary X-ray analysis of bifunctional dihydrofolate reductase-thymidylate synthase from *Plasmodium falciparum*. Erratum. Acta Crystallogr D Biol Crystallogr 2004;60(Pt 6):1185.

53. Meek TD, Garvey EP, Santi DV. Purification and characterization of the bifunctional thymidylate synthetase-dihydrofolate reductase from methotrexate-resistant *Leishmania tropica*. Biochemistry 1985;24(3):678-86.

Copyright by Mahidol University

54. Freidkin M, Crawford EJ, Misra DV. Reduction of folate derivatives with dithionite in mercaptoethanol. Fed Prc Fed An Soc Exp Biol 1963;21:176.
55. Amersham Pharmacia Biotech AB. Protein Purification Handbook. Uppsala, Sweden; 1999.
56. Hillcoat BL, Nixon PF, Blakley RL. Effect of substrate decomposition on the spectrophotometric assay of dihydrofolate reductase. Anal Biochem. 1967;21(2):178-189.
57. Laemmli UK. Cleavage of the structural proteins during the assembly of the head of bacteriophage T4. Nature 1970;227(259):680-685.
58. Amersham Pharmacia Biotech Inc. Protein electrophoresis, technical manual. USA; 1999.
59. Layne E. Methods in Enzymology. 1957;3:447.
60. Pace CN, Vajdos F, Fee L, Grimley G, Gray T. How to measure and predict the molar absorption coefficient of a protein. Protein Sci. 1995;4:2411-2423.
61. National Toxicology Program (NIH/NIEHS). NTP Chemical Repository: Trimethoprim.
In http://ntp-server.niehs.nih.gov; 2001.
62. Hampton Research. Tips from A to Z.
In http://www.hamptonresearch.com/support/atoz.html; 2003.
63. D' Arcy A, Elmore C, Stihle M, Johnston JE. A novel approach to crystallizing proteins under oil. J. Cryst. Growth. 1996;168:175-180.
64. Chayen NE, Shaw Stewart PD, Maeder DL, Blow DM. An automated system for micro-batch protein crystallization and screening. J. Appl. Crystallogr. 1990;23:297-302.
65. Ducruix A, Giege R. Methods of Crystallization. 2 ed. New York: Oxford University Press; 1999.
66. Sawyer L, Turner MA. X-ray analysis. 2 ed. New York: Oxford University Press; 1999.
67. Rodgers DW. Cryocrystallography. Structure 1994;2:1135-1139.
68. Petsko GA. Protein crystallography at subzero temperatures: cryoprotective motherliquors for protein crystals. J. Mol. Biol. 1975;96:381-392.

Copyright by Mahidol University

69. Garman EF, Mitchell EP. Glycerol concentrations required for cryoprotection of 50 typical protein crystallization solutions. J. Appl. Cryst. 1996;29:584-587.

70. Stura EA, Gleichmann T. Soaking techniques. 2 ed. New York: Oxford University Press; 1999.

71. Matthews BW. Solvent content of protein crystals. J. Mol. Biol. 1968;33:491-497.

72. McPherson A. The role of X-ray crystallography in stucture-based rational drug design: CRC Press Inc.; 1995.

73. McPherson A. Introduction to macromolecular crystallography. New Jersey: John Wiley & Sons, Inc.; 2003.

74. Brunger AT, Adams PD, Clore GM, DeLano WL, Gros P, Grosse-Kunstleve RW, Jiang J, Kuszewski J, Nilges N, Pannu NS, Read RJ, Rice LM, Simonson T, Warren GL. Crystallography & NMR System: A new software suite for macromolecular structure determination. Acta Crystallogr D 1998(54):905-921.

75. Rhodes G. Crystallography Made Crystal Clear: A Guide for Users of Macromolecular Models. 2 ed. California: Academic Press; 2000.

76. Jones TA, Zou JY, Cowan SW, Kjeldgaard M. Improved methods for building protein models in electron density maps and the location of errors in these models. Acta Cryst. 1991;A(47):110-119.

77. Holtje H-D, Sippl W, Rognan D, Folkers G. Molecular Modeling: Basic Principles and Applications. 2 ed. Germany: Wiley, VCH Verlag GmbH & Co.; 2003.

78. Kirkpatrick S, Gelatt CD, Vecchi MP. Optimization by simulated annealing. Science 1983;220:671-680.

79. Kleywegt GJ, Jones TA. xdlMAPMAN, and xdlDATAMAN-programs for reformatting, analysis and manipulation of biomacromolecular election density maps and reflection data sets. Acta Crystallogr. D 1996;52:826-828.

80. Collaborative Computational Project Number 4. The CCP4 Suite: Programs for Protein Crystallography. Acta Cryst. D 1994;50:760-763.

81. Vriend G. WHAT IF: a molecular modelling and drug design program. J. Mol. Graph. 1990;8:52-56.

Copyright by Mahidol University

82. Schnell JR, Dyson HJ, Wright PE. Structure, dynamics, and catalytic function of dihydrofolate reductase. Annu Rev Biophys Biomol Struct 2004;33:119-40.

83. Hitchings GH, Burchall JJ. Inihibition of folate biosynthesis and function as a basis for chemotherapy. Adv. Enzymol. Relat. Areas Mol. Biol. 1965;27:417-468.

84. Champness JN, Stammers DK, Beddell CR. Crystallographic investigation of the cooperative interaction between trimethoprim, reduced cofactor and dihydrofolate reductase. FEBS Lett. 1986;199(1):61-67.

85. Groom CR, Thille J, North ACT, Pictet R, Geddes AJ. Trimethoprim binds in a bacterial mode to the wild-type and E30D mutant of mouse dihydrofolate reductase. J. Biol. Chem. 1991;266(30):19890-19893.

86. Margosiak SA, Appleman JR, Santi DV, Blakley RL. Dihydrofolate reductase from the pathogenic fungus *Pneumocystis carinii*: catalytic properties and interaction with antifolates. Arch. Biochem. Biophys. 1993;305(2):499-508.

87. Howell EE, Villafranca JE, Warren MS, J. OS, Kraut J. Functional role of aspartic acid-27 in dihydrofolate reductase revealed by mutagenesis. Science 1986;231:1123-1128.

88. Baccanari DP, Daluge S, King RW. Inhibition of dihydrofolate reductas: effect of reduced nicotinamide adenine dinucleotide phosphate on the selectivity and affinity of diaminobenzylpyrimidines. Biochemistry 1982;21:5068-5075.

89. Sasso SP, Gilli RM, Sari JC, Rimet OS, Briand CM. Thermodynamic study of dihydrofolate reductase inhibitor selectivity. Biochimica et Biophysica Acta 1994;1207:74-79.

Copyright by Mahidol University

BIOGRAPHY

NAME Miss Duangrudee Tanramluk

DATE OF BIRTH October 25, 1979

PLACE OF BIRTH Bangkok, Thailand

INSTITUTIONS ATTENDED Kasetsart University, 1998:
Bachelor of Science (Chemistry)
Mahidol University, 2002:
Master of Sciene (Biochemistry)

HOME ADDRESS 47/34 Moo 4, Khokkham,
Muang, Samutsakhon
Tel. 0-3441-2134
E-mail: b4104056@alumni.ku.ac.th

RESEARCH GRANTS The Development and Promotion of Science and Technology Talents Project (DPST)
The Junior Science Talent Project (JSTP)

Copyright by Mahidol University